



Precision Measurements of Colloidal Dynamics with Holographic Microscopy

Citation

Martin, Caroline. 2024. Precision Measurements of Colloidal Dynamics with Holographic Microscopy. Doctoral dissertation, Harvard University Graduate School of Arts and Sciences.

Permanent link

<https://nrs.harvard.edu/URN-3:HUL.INSTREPOS:37378922>

Terms of Use

This article was downloaded from Harvard University's DASH repository, and is made available under the terms and conditions applicable to Other Posted Material, as set forth at <http://nrs.harvard.edu/urn-3:HUL.InstRepos:dash.current.terms-of-use#LAA>

Share Your Story

The Harvard community has made this article openly available.
Please share how this access benefits you. [Submit a story](#).

[Accessibility](#)

HARVARD UNIVERSITY
Graduate School of Arts and Sciences



DISSERTATION ACCEPTANCE CERTIFICATE

The undersigned, appointed by the

Harvard John A. Paulson School of Engineering and Applied Sciences
have examined a dissertation entitled:

“Precision Measurements of Colloidal Dynamics with Holographic Microscopy”

presented by: Caroline Martin

Signature

Typed name: Professor Vinny Manoharan

Signature

Typed name: Professor Frans Spaepen

Signature

Typed name: Professor Michael Brenner

April 29, 2024

Precision Measurements of Colloidal Dynamics with Holographic Microscopy

A DISSERTATION PRESENTED

BY

CAROLINE MARTIN

TO

THE HARVARD JOHN A. PAULSON SCHOOL OF ENGINEERING AND APPLIED SCIENCES

IN PARTIAL FULFILLMENT OF THE REQUIREMENTS

FOR THE DEGREE OF

DOCTOR OF PHILOSOPHY

IN THE SUBJECT OF

APPLIED PHYSICS

HARVARD UNIVERSITY

CAMBRIDGE, MASSACHUSETTS

APRIL 2024

©2024 – CAROLINE MARTIN
ALL RIGHTS RESERVED.

Precision Measurements of Colloidal Dynamics with Holographic Microscopy

ABSTRACT

To build a holographic microscope, take a standard optical microscope and illuminate the sample with a coherent light source like a laser. Light scattered by the specimen interferes with the transmitted beam, producing an interference pattern called a hologram, a two-dimensional image that encodes three-dimensional information about the sample. While holograms are typically interpreted through reconstruction, recent advances in computational methods have enabled a new approach: extracting information directly from holograms using generative modeling. The combination of holographic microscopy and model-based analysis is well suited to applications where precise, quantitative results are needed with high acquisition speed, including characterizing colloidal dispersions, following the motion of microscopic objects in three dimensions, or measuring colloidal interactions.

I overview methods and applications of generative modeling to holographic microscopy. I then consider the application of those methods to understanding colloidal suspensions, micrometer-scale particles suspended in fluids. With holographic microscopy, we can characterize and track colloidal particles in three dimensions with high precision. However, the accuracy of particle tracking and characterization depends on how well we model hologram formation. I investigate the effects of spherical aberration on the structure of single-particle holograms and on the accuracy of particle characterization. I show that fitting a model that accounts for spherical aberration decreases aberration-dependent error, even when the spherical aberration in the optical train is unknown.

With this new generative model, the inferred parameters are consistent across different levels of aberration, making particle characterization more robust.

Finally, I use holographic microscopy and generative modeling to characterize short-ranged colloid interactions. Understanding the interactions between colloidal particles is essential for predicting and controlling colloidal self-assembly, but methods to characterize these interactions can be limited to observing highly constrained particles. Moreover, these methods can face issues with precision due to multiple scattering between particles and out-of-plane fluctuations. I demonstrate an alternative method to infer particle potentials from holographic data. This method rigorously accounts for scattering effects, works in three dimensions, and does not require the particles to be trapped in an optical potential. With this method, I precisely track pairs of freely-diffusing spheres in three dimensions and at high frame rates. I show that by using Bayesian inference, we can measure separation distances as small as a few nanometers between micrometer scale particles to nanometer-scale precision. From these precise measurements of gap distances, I quantify the short-ranged forces acting on the colloidal particles with model-free and model-based methods. I characterize a range of depletion-driven particle interactions with varying particle size and depletant concentration, and precisely quantify the well curvature about the potential minimum.

Contents

TITLE PAGE	i
COPYRIGHT	ii
ABSTRACT	iii
TABLE OF CONTENTS	v
LISTING OF FIGURES	vii
PRIOR PUBLICATIONS	ix
ACKNOWLEDGEMENTS	x
1 INTRODUCTION	1
1.1 Colloidal suspensions	3
1.2 Holographic microscopy	7
2 IN-LINE HOLOGRAPHIC MICROSCOPY WITH MODEL-BASED ANALYSIS	9
2.1 Experimentation	14
2.2 Results	19
2.3 Applications	30
2.4 Reproducibility and data deposition	37
2.5 Limitations and optimizations	39
2.6 Outlook	43
3 IMPROVING GENERATIVE MODELS FOR HOLOGRAPHIC MICROSCOPY	46
3.1 Effect of spherical aberration on hologram structure	50
3.2 Modeling the effect of spherical aberration	54
3.3 Effect of spherical aberration on particle characterization	56
3.4 Numerical methods	61
3.5 Conclusion	64
4 HIGH-PRECISION MEASUREMENTS OF PARTICLE GAP DISTANCES	66
4.1 Methods	69
4.2 Bayesian analysis of holograms	72
4.3 Prior characterization of spheres	75
4.4 Model parameterization	79
4.5 Model fitting	80

4.6	Results	83
4.7	Conclusion	83
5	INFERRING SHORT-RANGED COLLOIDAL INTERACTIONS	87
5.1	Boltzmann inversion	89
5.2	Fitting Boltzmann model to full distribution	92
5.3	Increasing depletant concentration	101
5.4	Measurements of particle interactions on glass surface	102
5.5	Conclusion	109
6	CONCLUSION	111
6.1	Informing and comparing to simulation	112
6.2	Other methods of inferring particle pair potentials	114
6.3	Outlook	117
REFERENCES		137

Listing of figures

1.1	Self-assembly in nature	2
1.2	Image and diagram of colloidal suspension	3
1.3	Diagram of holographic microscopy	8
2.1	Schematic of hologram formation and analysis by generative modeling	11
2.2	Detailed setup of in-line holographic microscope	15
2.3	Data normalization for hologram analysis	20
2.4	Flow chart of approaches to quantitative analysis of holograms	22
2.5	Applications of generative modeling and holographic microscopy to particle tracking	31
2.6	Applications of generative modeling and holographic microscopy to particle characterization	35
3.1	Diagram and schematic of optical train for typical in-line holographic microscope .	49
3.2	x - z cross-sections of stacks of holograms of an immobilized sphere compared to modeled cross-sections	53
3.3	Sum of squared residuals for fits with lens and aberrated-lens model	58
3.4	Best fit parameters inferred by fitting with lens model and aberrated-lens model .	59
4.1	Using holographic microscopy to infer particle gap distances	70
4.2	Full posterior probability density with lens model	78
4.3	Fitting holograms of particle dimers with gap distance	79
4.4	Sampled posterior probability density characterizing two interacting colloidal spheres	84
4.5	Inferred posterior probability of gap distance and particle size	85
4.6	Gap distance of particle pair across single video	85
5.1	Particle trajectory, histogram, and inverted histogram with fits to models of particle potential	90
5.2	Effect of bin size on Boltzmann inversion	92
5.3	Schematic of the sum of interactions in experimental system	94
5.4	Inferred probability density for a Boltzmann model parameterized in terms of AO attraction and a generic repulsion	97

5.5	Bayesian fit to AO model with repulsive term	98
5.6	Posterior and spring constant from fitting Morse potential to full distribution of gap distances.	100
5.7	Additional peaks in distributions of gap distances at high depletant concentrations	101
5.8	Full histograms of particle gap distance at varying depletant concentrations	103
5.9	Histograms of particle gap distances at varying depletant concentrations	104
5.10	Boltzmann inversion and fits to a Morse potential for varying depletant concentrations	105
5.11	Posterior probability density spring constants across depletant concentration	108
6.1	Measured particle interactions and Morse potential	113
6.2	Confocal images of colloidal crystallization over varying depletant concentrations . .	113
6.3	2D interactions of colloidal spheres	115
6.4	Inferring 2D particle interactions	117

Prior Publications

The following chapters of this thesis are based on previously published work:

- Chapter 2: “In-line holographic microscopy with model-based analysis.” Caroline Martin, Lauren E. Altman, Siddharth Rawat, Anna Wang, David G. Grier, Vinothan N. Manoharan. *Nat. Rev. Methods Primers* 2, 83 (2022)
- Chapter 3: “Improving holographic particle characterization by modeling spherical aberration,” Caroline Martin, Brian Leahy, and Vinothan N. Manoharan. *Opt. Express* 29, 18212-18223 (2021)

Other works to which the author has contributed as a doctoral student include:

- “Large depth-of-field tracking of colloidal spheres in holographic microscopy by modeling the objective lens.” Brian Leahy, Ronald Alexander, Caroline Martin, Solomon Barkley, and Vinothan N. Manoharan. *Opt. Express* 28, 1061-1075 (2020)
- “Precise characterization of nanometer-scale systems using interferometric scattering microscopy and Bayesian analysis.” Xander M. de Wit, Amelia W. Paine, Caroline Martin, Aaron M. Goldfain, Rees F. Garmann, and Vinothan N. Manoharan. *Appl. Opt.* 62, 7205-7215 (2023)

Other publications relating to the work discussed in this thesis are in preparation.

*What! are you never to hear yourself praised!—
Then you must be no friend of mine; for those
who will accept of my love and esteem, must
submit to my open commendation.*

Jane Austen, *Sense and Sensibility*

Acknowledgments

THOUGH THESE THANKS are some of the first words in this dissertation, they are the last words I will write for it. It's a hard task to look back and try to list everyone who has held you up and helped you grow over the formative years of the PhD. I hope these acknowledgements will at least capture some of the gratitude I feel for everyone who helped me reach this point.

I want to first thank everyone I've worked with directly over the years. When I first started my graduate research, I joined a great team of people using holography, especially Ron, Brian, and Solomon. They taught me so much about holopy, data analysis, and fitting, and always made me feel like I was part of the team. Thanks especially to Brian, who I worked closely with, for taking me seriously from day one. Thanks also to Jessica for her endless expertise on colloids, cellulose polymers, and making sample chambers. Whenever I was stuck, I could always count on Jessica for advice, or at the very least commiseration. Thanks to Kellianne for wading into the holographic microscope with me for a summer, and aligning that laser. I also worked with wonderful undergraduates, including Jacquie, Lev, and Natty, who were so bright and curious, and really inspiring to work with. I also had the privilege of working with many current and former members of the Brenner group, including Ella, Qian-Ze, Alp, and Megan. It was a delight to talk about these problems with them. I always managed to leave our meetings with more understanding than when I went in, which is a rarity for scientific meetings.

I also want to thank my committee. First, Michael Brenner, whose meetings were always a jolt to my research. It was in one such meeting with Michael that I think I set a record for fastest explanation of holographic microscopy that I've ever given. I'd like to thank Michael for his enthusiasm and energy, and for such a fun and fruitful collaboration with his group. I'd also like to thank my other committee member, Frans Spaepen, who has a knack for asking the exact right question every time I talk to him about my work. Thank you so much for sharing your wisdom, expertise, and kindness. And finally, I'd like to thank my advisor, Vinny Manoharan. I came to Harvard planning on working with Vinny, and I knew I had made the right choice on the first day of his statistical mechanics class. I remember how he started the course with a discussion about how science has historically pushed certain people to the margins, and how it was our responsibility to understand the context of the process of science, and our privilege to make our own contributions. I left that lecture so excited to work with him, and here, six years later, I know I made the right choice. Thank you for encouraging me to raise my voice, for fighting with me in meetings with paper editors, and for pushing

me to clarify my thoughts and convictions. I have learned from Vinny how to be a better scientist, communicator, and teacher.

The Manoharan group has been one of the best parts of my PhD. It is such a special community in the office and lab, even though they always plan to go out for ice cream when I'm not there. I can't imagine a better group of people to work with, and I'll miss you all terribly. I also want to thank Jerome Fung, a former Manoharan lab member, my undergraduate advisor at Wellesley College, and the reason I ended up on the path I took. Thanks to Jerome for sparking a love of soft matter, and for his endless kindness, encouragement, and mentorship.

I was worried about coming to Harvard for physics, because "Harvard physicists" sound like they may be the worst people in the world. But thank goodness I was wrong. After moving into the reject room in the G1 space, I found a community full of curiosity and passion, but also support and laughter. Thanks especially to Nick, Anne, Alex, Lewis, and honorary physicists Marya and Anna. I also want to thank all my friends from Wellesley, who welcomed me into a rich intellectual community, and shared with me many bowls of ice cream and passionate debates on whether planets could be shaped like donuts. Thanks also to my friends who sustained me virtually through some very hard times, especially Maxine and my best friend from forever Darby. I was also very lucky to be part of an amazing outreach group called WOW STEM. Thanks especially to Katie, Justina, and Ashley. You all have made the past six years so special.

During my time here, I've been lucky enough to have friends that have become my family. Ella, Taylor, DaLi, Kara, Madelyn, Jon, and Luis, it's hard for me to express how much you mean to me. I treasure every family dinner, every terrible episode of Vampire Diaries, every themed party, every commitment to the bit. I'm so happy to have had the time we had together, with all of us living in the Greater Wine and Cheese Cask Area. I'm sad it's ending, but the years we had were special and golden, and I know you all will be in my life forever.

I owe so much to the love and support I receive from my family. My brother and sister are two of my best friends. And I think it's pretty obvious they both want to follow in my footsteps, since my brother Thomas is coming to Harvard next year for law school, and soon my sister Grace is also going to become Dr. Martin, but the real kind of doctor that actually helps people. Thanks especially to both my parents, for their endless love and encouragement and support. My parents both are the reasons I took the path I did. My mom, for modeling what it means to be a scientist and do research, and my dad, for encouraging me from a very young age not to do a PhD in English. I love you all so much.

Finally, I want to thank my boyfriend Jack, and importantly also thank the MBTA Commuter Rail for helping him commute back and forth from Providence to be with me. I was not expecting to find Jack, but as soon as I did, I knew exactly what my future was going to look like. Regardless of anything else, it was going to be with him. I can't wait for that future to start. I love you. Thank you so much for everything.

*We saw to the edge of all there is —
So brutal and alive it seemed to comprehend us back.*

Tracy K. Smith, *My God, It's Full of Stars*

1

Introduction

WILSON BENTLEY, THE FIRST RECORDED person to take photomicrographs of snowflakes, described his subjects as “tiny miracles of beauty” ¹. Bentley’s images of the delicate structure of snow crystals gave rise to a widespread misconception that no two snowflakes can ever be alike. But we now know that this is not true. Snowflakes form after nucleation on a seed, with water molecules crystallizing as the snowflake tumbles in a chaotic path through a cloud with locally varying tem-

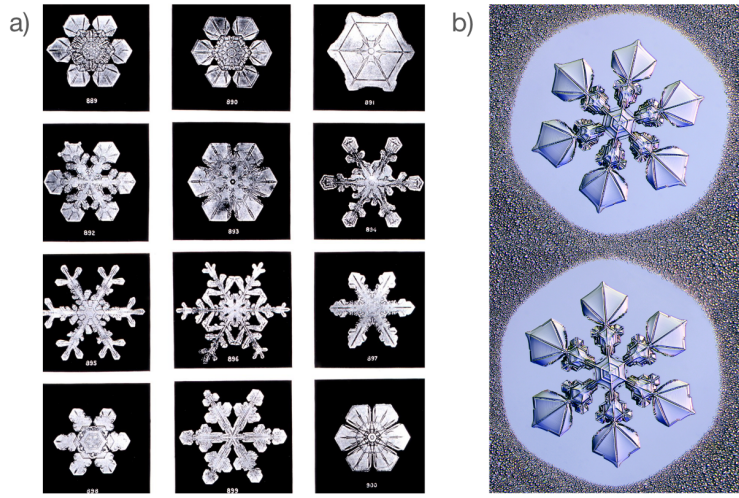


Figure 1.1: (a) Photomicrographs of natural snowflakes published by Wilson Bentley showing the wide array of self-assembled structures that snowflakes can have. Image from Plate XIX¹, in the public domain. (b) Photomicrographs of two “twin” snowflakes grown in a lab under identically varying temperature and humidity conditions. As the snowflakes grow, they deplete water vapor from the surrounding air, leading to a local region of low humidity with few condensed droplets surrounding the snowflakes. Image by Kenneth G. Libbrecht ©, reused with permission.

perature and humidity. It is the randomness of this path, and the sensitive phase behavior of crystal growth in the basal or prism facets under different conditions, that leads to the unique structure of snowflakes. But when two nucleation seeds are exposed to the same variations in temperature and humidity (in a lab, rather than a cloud), the same structure emerges – not by a miracle, but by assembly². While snowflake growth may seem chaotic, the structure emerges by predictable physical processes, including nucleation, crystallization, and growth instabilities.

In this thesis, we do not attempt to unravel the complex physics of snowflake assembly. The growth of a single snowflake involves over 100 quintillion water molecules; tracking the motion of those molecules as the snowflake forms is a daunting, if not impossible, task. We do, however, consider what is needed to understand how complex structures emerge and assemble: quantitative measurements of the interactions between the components. To do so, we consider a much simpler, synthetic system called colloidal suspensions.

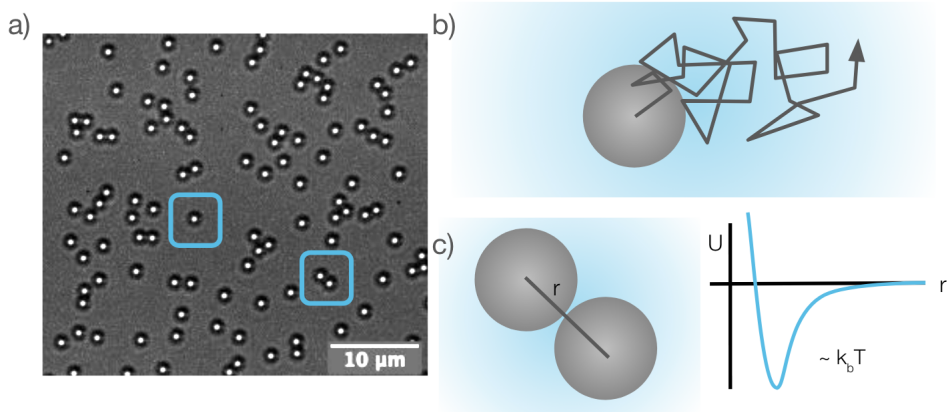


Figure 1.2: (a) Bright-field microscope image of $1.3 \mu\text{m}$ diameter polystyrene spheres on a glass slide. The particles are freely diffusing on the surface, and have an attraction induced by the presence of depletant polymers. (b) Diagram of Brownian motion. Due to random collisions with the molecules of the surrounding fluid, colloidal particles move with a random walk. (c) Diagram of two interacting spheres. Colloidal particles interact through a pair potential that depends on their distance from each other. The interaction – the sum of the attractive and repulsive forces between them – has a well depth of the order of $k_b T$.

1.1 COLLOIDAL SUSPENSIONS

Colloidal particles, or colloids, colloquially, are microscopic particles suspended in a fluid, small enough to be stochastic in their dynamics owing to random Brownian motion, but large enough to be observed with a bright-field optical microscope.

Colloidal suspensions can make up commercial products like paints or inks, or close-packed arrangements of spheres with interesting optical properties such as structural color³ or photonic bandgaps⁴. But we can also consider colloidal spheres model “big atoms”⁵ that can be used to study phenomena like self-assembly or self-organization. We can synthesize colloidal spheres with interactions that we can control, and we can observe colloids in real time as they form compact clusters⁶, arrange themselves into a crystal lattice⁷, or undergo phase transitions⁸. By observing how the particles assemble, move, and interact, we can understand the interplay between energy and entropy that leads to the emergence of structure.

In the process of self-assembly, that interplay between energy and entropy can be understood by the minimization of free energy, $F = U - TS$, which depends on both the energy U and the entropy S at temperature T . We may naively conceive of self-assembly as the victory of the order of interactions over the disorder of entropy, occurring only when the pull of the attraction between subcomponents is strong enough to wrest an ordered structure from chaos. But this is not always the case. In fact, order can emerge from entropic effects alone, such when densely packed microscopic spheres spontaneously crystallize to maximize the configurational space available to them⁹. Entropy can act in tandem with energy to stabilize configurations, allowing the emergence of a particular structure.

How are we to understand the subtle role entropy can play in the emergence of structure? How are we to quantify the energetic terms for a particular system? And what forces and interactions govern particle dynamics at the microscopic scale? These questions can be challenging to answer, especially for atomic or molecular-scale systems where it is impossible to track every interacting particle. Colloidal suspensions, by contrast, are much larger, making it possible to track every subcomponent to understand how they interact and assemble. With measurements of where these particles are in space over time, we can begin to unravel the forces, energy, and entropy of the system.

Measurements of colloidal motion can reveal unexpected phenomena and new physics. Observations of the motion of single particles have led to the validation of theories of diffusion for colloidal spheres¹⁰, the discovery of surprisingly long relaxation times of colloidal particles pinned at an interface^{11,12,13,14}, and the recognition of unexpected diffusion mechanisms of helical particles in a dense suspension^{15,16}. Observations of many-particle dynamics have been used to make rheological measurements of synthetic and biological systems^{17,18,19,20}, to understand phase transitions of hard sphere colloidal particles^{9,21}, or to track defects and dislocations as they move through a colloidal crystal^{22,23}. The motion of small clusters has also been used to unravel the physics of colloidal interactions, including the role of hydrodynamics in colloidal systems²⁴, DNA-mediated interactions²⁵,

or unexpected multi-body effects such as like-charge attraction^{26,27,28,29}.

Colloidal dynamics began with a mystery: when we suspend colloidal particles in a fluid and put them under a microscope, the particles appear to dance. Robert Brown was the first to observe this motion through microscopic observations of small pollen grains suspended in water. After observing the microscopic grains, he noted the “very unexpected fact of seeming vitality retained by these minute particles”³⁰. He eventually found that this diffusive motion was not a vitality exclusive to biological material, but existed for all manner of microscopic particles suspended in fluids. It was not a marker of life, but rather a result of the molecular nature of matter itself.

In addition to stochastic forces from collisions with the fluid, colloidal particles can also exert forces on each other. By measuring the statistics of the motion of two interacting particles, we can infer the underlying interactions between the components. In equilibrium, the distribution of distances r between two particles is given by a Boltzmann distribution that depends on the particle pair potential $U(r)$ such that

$$p(r) \propto \exp [-\beta U(r)], \quad (1.1)$$

where $\beta = 1/k_b T$, k_b is the Boltzmann constant, and T is the temperature. Measurements of the distribution of positions that the interacting particles sample thus gives us insight into the underlying pair potential, which has implications for quantifying the energy and entropy in a particular system and understanding self-assembly and structure formation.

Accurate knowledge of short-ranged interactions between particles is essential for controlling and predicting a range of behavior in soft matter, from crystallization³¹ to defect mobility^{22,23} to cell clustering³². In colloidal systems, interactions between micrometer-scale particles can be experimentally tuned through screened electrostatics³³, entropically-driven depletion interactions⁸, or DNA-mediated attraction from base-pairing of single-stranded DNA polymers rooted on the surfaces of the particles³⁴.

By changing the attractive and repulsive forces the particles experience, we can experimentally control the phase behavior and self-assembly of colloidal spheres. In fact, the assembled structure can be sensitive to the depth and curvature of the interparticle potential well. For example, the depth of the potential well can control whether a bond between particles is transient or stable. When the well depth is close to the order $k_b T$ – the order of thermal fluctuations in the system – particle bonds are short-lived. Well depths much greater than $k_b T$, on the other hand, can make bonds effectively permanent. This tunability in bond behavior can be observed in lock-and-key colloids³⁵, which take advantage of particle geometry such that only bonds formed by on-target binding of smaller “key” particles in the dimple of a larger “lock” particle are stable, while bonds formed by off-target binding outside of the dimple are transient.

But it is not just the depth of the well that controls structure and assembly behavior. The shape of the potential can also sensitively impact structure formation. For colloidal clusters with a short-ranged depletion interaction, the probability of finding nonrigid clusters depends sensitively on the curvature of the pair potential about the minimum, which controls the vibrational entropy of each structure⁶. In fact, Meng and coworkers found discrepancies between measurements and theoretical predictions of cluster populations, which they attribute to the difficulty in precisely quantifying both the depth and curvature of the particle pair potentials. Similarly, vibrational and rotational entropy can also stabilize open lattices of patchy colloidal particles. In both experiment and simulation, the open Kagome lattice of patchy particles has been found to be stabilized by the additional “rattle room” available to the particles as compared to the close-packed lattice^{36,37}.

Accurate knowledge of underlying particle interactions is also essential for computationally predicting colloidal behavior. Simulations have been used to predict design rules³⁸ and to infer the potential needed to achieve a particular self-assembled structure^{39,40}. With advances in automatic differentiation, entire particle simulations can be optimized for the inverse design of material structure, properties⁴¹, or even kinetics⁴². Knowledge of particle interactions can also be helpful for

predicting dynamics, such as with particle tracking algorithms that have improved accuracy by incorporating particle interactions⁴³.

These examples show the importance of understanding how colloidal particles interact. To solve such problems such as tuning assembled structures or predicting equilibrium populations, we need to precisely characterize both the depth and curvature of the potential well.

1.2 HOLOGRAPHIC MICROSCOPY

So far, I have claimed that colloids are ideal systems for understanding microscale forces, entropic effects, and structure formation because they are easily observable. And due to their stochastic motion from thermal fluctuations, two particles in equilibrium will sample their free energy landscape, leading to a distribution of gap distances between the particles that depends on the pair potential. By quantifying the statistics of particle positions, we can measure the underlying particle interactions, enabling us to better understand and predict colloidal assembly, and to understand the fundamental forces that colloidal particles experience.

These interactions – such as depletion, screened electrostatics, or van der Waals forces – can be very short-ranged, acting on the order of nanometers from the surface of the micrometer-scale sphere. Thus, we require that any measurements we make of their relative position be precise to the nanometer scale. Additionally, in order to directly measure the particle interactions, we would like to measure the particles as they freely move in three dimensions, without confinement or an external potential. Thus, if we are to probe colloidal interactions by measuring the relative positions of two interacting spheres, we need rapid, three dimensional particle localization to nanometer-scale precision without confinement.

To achieve these requirements, I use holographic microscopy, a technique where a sample is illuminated with a coherent beam and we record the inference between that beam and the light scat-

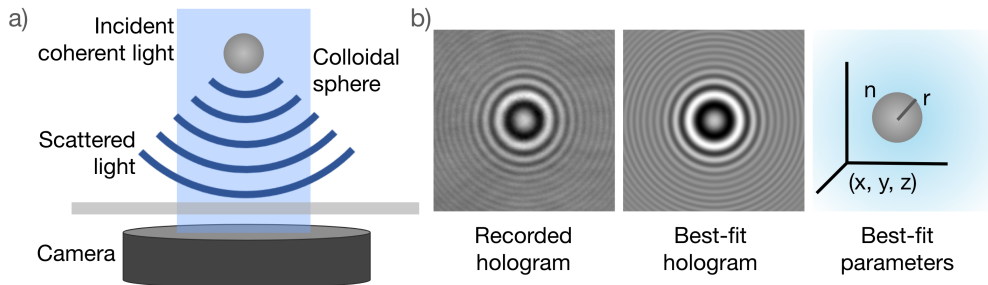


Figure 1.3: (a) Diagram of holographic microscope. Incident coherent light is scattered by the sample. We record the inference pattern of the two fields, a hologram. (b) Recorded hologram of $1.3\text{ }\mu\text{m}$ diameter polystyrene sphere with best-fit hologram found by fitting a model to the data. The best fit parameters quantify where the particle is in three dimensional space, as well as its size and composition.

tered by the object of interest (Fig. 1.3a). This thesis focuses on the development and application of generative modeling approaches to holographic microscopy. The combination of holographic microscopy and model-based analysis is well suited to applications where precise, quantitative results are needed with high acquisition speeds, such as characterizing colloidal dispersions, following the motion of microscopic objects in three dimensions, or measuring colloidal interactions.

I first discuss the advantages and applications of a model-based approach to analyze holograms in order to extract quantitative information about a particle's three dimensional position, size, and composition (Fig. 1.3b) in detail in Chapter 2. I then discuss my work to improve the models we fit to holograms by accounting for optical effects, such as transformations from lenses in the optical train and distortions induced by spherical aberration. I find that by modeling these effects, we can more accurately characterize particles in aberrated and unaberrated systems. Finally, I discuss my application of these methods to precisely infer short-ranged colloidal interactions. I characterize a range of particle interactions and achieve nanometer-level precision with a Bayesian approach to the data analysis. I end by looking forward. I consider expansions of the method I developed here, discuss alternative approaches to inferring pair potentials of many interacting particles, and broadly consider how this work fits into the growing trend of quantitative microscopy.

*I climbed the three staircases, raised the trapdoor of the
attic, and having reached the leads, looked out afar over
sequestered field and hill, and along dim sky-line: that
then I longed for a power of vision which might overpass
that limit; which might reach the busy world, towns,
regions full of life I had heard of but never seen.*

Charlotte Brontë, *Jane Eyre*

2

In-line holographic microscopy with model-based analysis

The contents of this chapter have been previously published⁴⁴. Reprinted with permission from:

“In-line holographic microscopy with model-based analysis.” Caroline Martin, Lauren E. Altman, Siddharth Rawat, Anna Wang, David G. Grier, Vinothan N. Manoharan. *Nature*

The material in this chapter is based upon work at Harvard that is supported by the National Science Foundation under grant DMR-2011754 and by the Department of Defense through the National Defense Science and Engineering Graduate Fellowship Program; work at UNSW Sydney that was supported by the Human Frontier of Science Program Grant (RPG0029/2020), and the Australian Research Council Discovery Early Career Award (DE210100291); and work at NYU that was supported by the National Science Foundation under grants DMR-2104837, DMR-1420073 and DMR-0922680, and by the National Institutes of Health under grant R44TR001590.

IT IS NOT DIFFICULT to make a holographic microscope – that is, a microscope that captures holograms rather than photographs. One needs only to replace the white light source in a standard light microscope with a laser aimed at the specimen. The resulting instrument captures in-line holograms⁴⁵. Though the word hologram might evoke images from popular culture, such as projections of Tupac Shakur or Princess Leia, a true hologram is not an image projected in three-dimensional (3D) space. Instead, it is pattern of bright and dark fringes. The fringes of an in-line hologram form when light scattered from the specimen interferes with light transmitted through it, as shown in Figure 2.1a.

Compared to a conventional photograph, a hologram such as the examples in Figure 2.1b can be difficult to interpret by eye. And unlike the vivid, colorful photographs captured by optical microscopy, the monochrome fringes of a hologram are unlikely to grace a journal cover. These concerns raise the question of why anyone would want to convert a microscope into a holographic microscope.

Our answer is that what is important is not the image itself, but instead what we infer from it. We usually want to do more than just see a microscopic object; we want to precisely quantify its properties — what it is made of, how big it is, where it lies in 3D space, and how fast it moves. This is

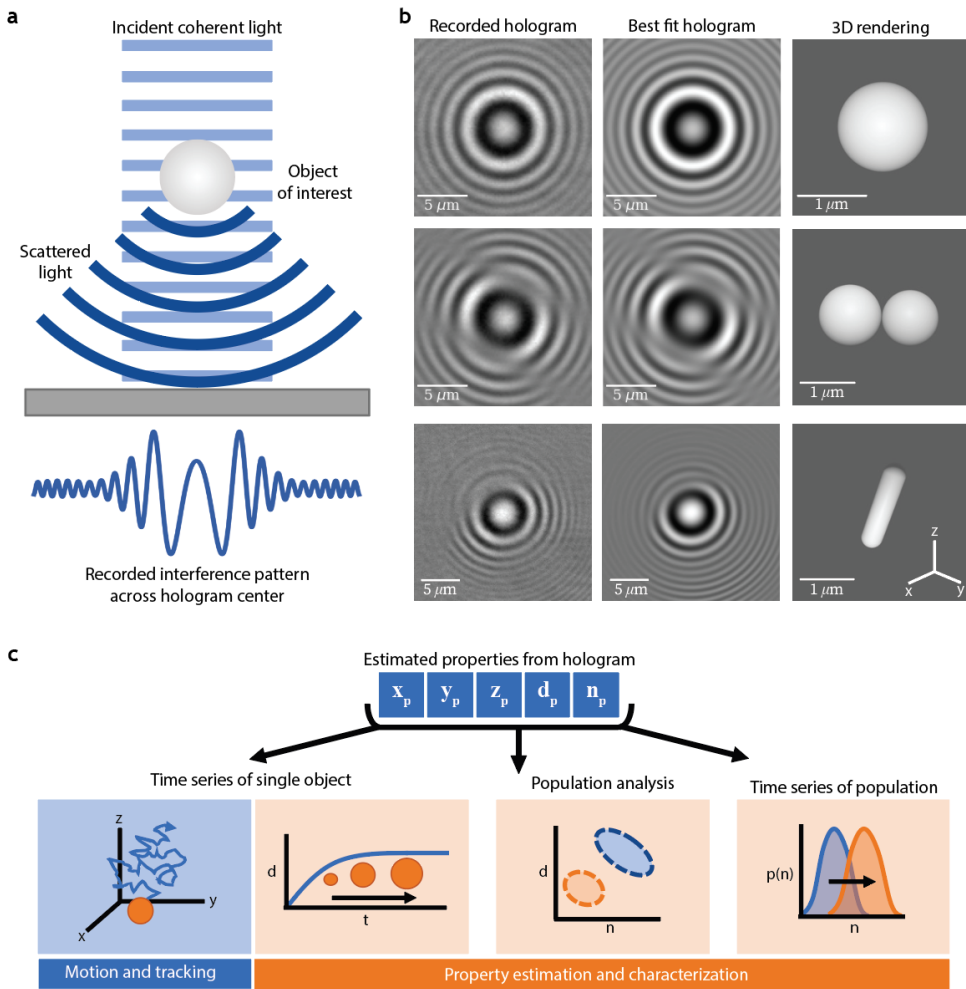


Figure 2.1: Hologram formation and analysis. a) Incident coherent light (light blue) interferes with the light scattered (dark blue) by a specimen. Useful information about the specimen can be extracted from the resulting interference pattern, or hologram, shown as the intensity across its centerline. b) Holograms, best fits, and 3D renderings of a single sphere, sphere doublet, and a capsule-shaped bacterium (bottom row adapted from Wang et al.⁴⁶). Best-fit holograms and 3D renderings are generated from the estimated properties of the specimen, including position, diameter, and refractive index. c) Diagram showing how analyzing many holograms from a specimen yields information that is useful for applications. Analyzing many holograms from the same object as a function of time can reveal its motion in 3D space or how its properties change. Analyzing holograms from a population of objects can differentiate multiple species within a sample. Finally, analyzing a hologram from a population of objects over time can reveal changes in the distribution of properties.

where holographic microscopy excels. Electromagnetic radiation has both an amplitude and phase, but conventional optical microscopes capture little information about the phase. By contrast, a holographic microscope is designed to capture phase information, which is encoded in the fringes. The phase information allows us to quantify many features of a microscopic specimen. For example, the 3D structure and composition of a specimen can be inferred from a single 2D hologram. Denis Gabor, the inventor of holography, showed that shining light through a recorded hologram generates a 3D reconstruction of the light scattered by the original object^{47,48}. Reconstruction has enabled non-invasive 3D imaging of colloidal particles^{49,50,51}, material microstructures⁵², microorganisms^{49,52,53,54,55}, and living eukaryotic cells^{56,57,58}. More complex optical setups can provide additional information about phase changes within a specimen^{59,60,61} and yield tomograms of complex 3D specimens^{62,63}.

This chapter focuses on an alternative analysis methodology: extracting information directly from the hologram without reconstructing it. The analysis relies on physics-based models of how microscopic objects scatter light. Unlike reconstruction, model-based analysis requires prior information about the object's shape and structure. This information influences the choice of model. For objects like colloidal particles, which might be described as spheres^{64,65,66}, ellipsoids⁶⁷, spherocylinders⁶⁸, or clusters of spheres⁶⁹, models can be based on exact solutions to Maxwell's equations that describe the scattering. For other specimens, such as living cells, the scattering can either be numerically simulated^{68,70,71} or the specimen can be modeled as a simpler shape, such as a sphere. In each of these cases, the scattered field $\mathbf{E}_{\text{inc}}(\mathbf{r})$ is a function of the object's 3D position (\mathbf{r}), orientation, refractive index, and size. We can predict the intensity $I(\mathbf{r})$ of the hologram by accounting for the interference with the reference field $\mathbf{E}_{\text{inc}}(\mathbf{r})$:

$$I(\mathbf{r}) = |\mathbf{E}_{\text{inc}}(\mathbf{r}) + \alpha \mathbf{E}_{\text{scat}}(\mathbf{r})|^2, \quad (2.1)$$

where the phenomenological parameter α accounts for imperfections in the illumination⁶⁶.

Modeling enables three different approaches to hologram analysis. In the first, we directly fit the model to an experimentally captured hologram to infer information about the object — a generative modeling approach. In the second, we use modeling to train an algorithm to classify and quantify features from experimentally captured holograms — a machine-learning approach. In the third, we use machine-learning to estimate parameters and then refine these estimates by fitting a generative model — a hybrid approach. As we shall show, a lot of information can be extracted from a hologram, including the object's size, orientation, and composition, as well as its 3D location (Figure 2.1b). The uncertainties in these measurements can be remarkably small. The size and 3D position of a microscopic object can be measured to nanometer-scale precision, while the refractive index and orientation can be measured to part-per-thousand precision⁶⁶.

Where high-precision measurements are the main goal, a model-based analysis has several advantages over reconstruction. First, model-based analyses directly give values and uncertainties for quantities of interest. By contrast, reconstructions and tomograms are images —albeit 3D ones — that do not quantify the properties of the specimen without further analysis. Second, models account for the complex scattering of objects similar in size to the wavelength of light, such as colloidal particles or bacteria. For such objects, diffraction can distort reconstructions⁷². Third, model-based analyses yield precise results even with the simplest optical setup, the in-line configuration shown in Figure 2.1a. Unless otherwise stated, we use the term holographic microscope to refer only to this microscope configuration.

The wealth and precision of information that can be extracted from in-line holograms with a model-based approach enables a host of applications, including 3D tracking of colloidal particles, measuring the forces exerted by cells, analyzing the composition of complex dispersions, and performing sensitive biochemical assays (Figure 2.1c). Many of these applications benefit from the speed of a holographic microscope. Holograms can be collected as quickly as the camera records

images because no mechanical adjustments are needed to keep the object in focus; any movement in the axial direction can be measured from the fringes. Typically, analyzing holograms takes more time than acquiring them. However, many sensitive and sophisticated analyses can be done in near-real time on a personal computer.

The model-based approach requires a careful choice of analytical method and some prior knowledge of the sample. As a result, it has some limitations, which we discuss in the penultimate section of this chapter. Other sections explore how to create and use a holographic microscope; how to analyze the data; what measurements can be made; what reproducibility issues might be encountered and how to overcome them. In the final section we consider the future of model-based analysis, an emerging paradigm for microscopy.

2.1 EXPERIMENTATION

2.1.1 INSTRUMENT LAYOUT

One can convert an optical microscope to an in-line holographic microscope by making the illumination coherent, as shown in Figure 2.2a. The new illumination source can be either a laser or a partially coherent source, such as a single-color light emitting diode (LED). The illumination beam should be collimated and directed into the sample. Light passing through the sample is collected by the microscope's objective lens and projected by its tube lens onto an area sensor, typically a complementary metal oxide semiconductor (CMOS) camera. If the sample is not too dense or opaque — the usual condition under which optical microscopy is done — the incident beam will be weakly scattered, such that most of it is unperturbed. This unperturbed, transmitted light then interferes with the light scattered by the sample to form a hologram.

To integrate a coherent illumination source with the microscope, we place a fiber-collimated laser with narrow spectral bandwidth⁷³ between the illuminator and the phase ring turret/condenser, as

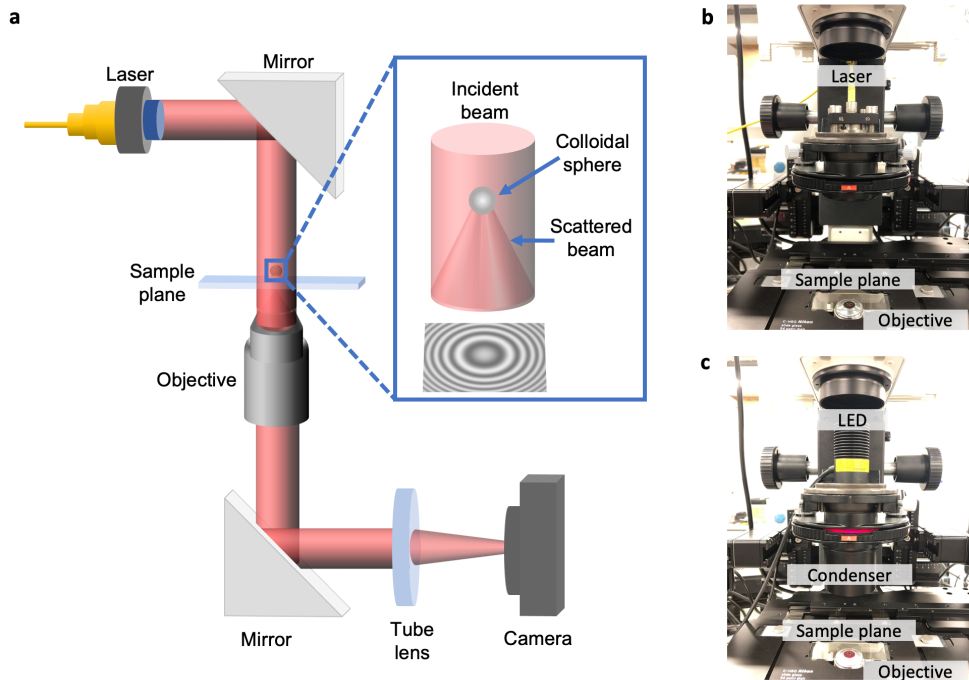


Figure 2.2: Detailed setup of in-line holographic microscope. a) Schematic of beam path and optical layout for an in-line holographic microscope with coherent illumination. A single-mode fiber coupled to the laser spatially filters the beam. The filtered beam (red) is steered to the sample plane, where it scatters from the specimen. The scattered and transmitted beams go through the objective and tube lens to the detector. b) Photograph of an in-line holographic microscope with a fiber-collimated laser source and no condenser lens, built on a standard inverted optical microscope. C) Photograph of an in-line microscope with LED source, where the inbuilt condenser lens collimates the partially coherent source.

shown in Figure 2.2b. We use single-longitudinal-mode diode lasers because they are inexpensive and bright. Furthermore, their coherence length is not too large, so that reflections from various glass surfaces in the microscope do not produce extraneous interference in the hologram. Alternatively, one can use a partially coherent source, such as an LED, as shown in Figure 2.2c. The low temporal and spatial coherence of LEDs can further suppress extraneous fringes and speckle relative to a diode laser⁷⁴. The longitudinal coherence length of commercially available LED sources is on the order of a few micrometers, which is large enough to obtain holograms of objects smaller than this scale, such as colloidal particles. Inserting a pinhole between the LED and the sample increases the spatial coherence but also reduces brightness^{75,76}. One must collimate the LED source by adjusting the distance between the LED and the microscope's inbuilt condenser lens. If the illumination source is already collimated, the condenser can be removed from the beam path.

Model-based analysis of holograms is most effective if the incident mode has the simplest possible structure. Therefore, we spatially filter the illumination source by, for example, coupling the laser source to a single-mode fiber. The illumination beam can then be reasonably described as a plane wave. We set or measure its polarization, which we need to model the scattered field.

The choice of objective lens depends on the size of the object to be imaged. For micrometer-scale objects, we use an objective with a high numerical aperture (NA), such as an oil-immersion or water-immersion lens. Though a water-immersion objective has a lower NA than an oil-immersion objective, it is potentially more useful for aqueous specimens because it reduces the spherical aberration introduced by a glass coverslip⁷⁷. In either case, it is important to select an objective that does not contain a phase plate, an inbuilt optical element used for phase-contrast microscopy, which would distort a hologram.

It is also possible to eliminate the objective lens altogether. One can construct a lensless holographic microscope from a coherent light source, a pinhole, and a sensor placed close to the sample^{75,78}. Lensless microscopes tend to have a small effective NA and a large effective pixel size. They

therefore cannot collect the strongly diverging light scattered by small particles or resolve finely spaced interference fringes. Lensless holography therefore is most effective for tracking and characterizing particles that are several times larger than the wavelength of light.

2.1.2 SAMPLE PREPARATION

Scattering from the sample chamber can add unwanted background interference to a hologram. To minimize background interference, we place our specimens in a sealed sample cell consisting of two glass coverslips separated by a spacer about 100 μm in height. The spacers can be silicone-based vacuum grease, double-sided tape, thin strips of plastic affixed with UV-curable epoxy, or silicone gaskets. We avoid evaporation and undesired flow by sealing the chamber with silicone grease or epoxy.

Some experiments require the sample to flow through the microscope's observation volume. To make a simple flow chamber, we place spacers between two glass surfaces and leave the edges unsealed. We then add a droplet or an absorbent material to one end to draw fluid through the channel by capillary action. To drive flow in more sophisticated flow chambers, such as microfluidic chips⁷⁹, we use syringe-pumps or pressure-pumps. We reduce interference due to reflections by making the channels wider, imaging the objects or particles only when they are a few micrometers away from the walls, or matching the refractive index of the fluid medium to that of the wall material. Flow enables high-throughput experiments, but one can also use an automated stage and a multi-well sample plate to carry out such experiments without flow.

Interfaces between fluids with different refractive indexes can significantly distort holograms. Holograms of particles at or near an interface should therefore be made in regions where the interface is flat. To encourage an air-water or oil-water interface to remain flat, we pin the interface¹¹ using a machined or 3D-printed chamber with a thin, flat lip.

Holograms can also be degraded by non-uniform illumination⁸⁰, undesired scattering from dust

particles or other out-of-focus objects, and optical aberrations⁸¹. If the hologram formation model does not correct or account for these effects, they can introduce errors into the inferred information. A spatial filter can alleviate non-uniform illumination, while a low-coherence source, such as a laser diode or LED, can attenuate holograms from out-of-focus objects. Cleaning the coverslips — by, for example, plasma cleaning, rinsing with purified water, and drying with nitrogen — reduces background scattering from dust in or on the sample chamber. If the sample solution is sufficiently dilute, the hologram of the object of interest will not substantially overlap with holograms of other objects. Typically, the sample should be dilute enough for the particles or objects to be at least a few micrometers apart⁸². With a dilute system, one can also record images with no objects in the field of view, and use these images to correct for background scattering. Finally, a water-immersion lens can minimize the effects of spherical aberration. Alternatively, spherical aberration can be incorporated in the model⁸¹.

2.1.3 DATA COLLECTION

The camera on a holographic microscope does not need to be expensive. For experiments involving a single illumination source, we use a monochrome sensor, because the filters on a color sensor reduce sensitivity and spatial resolution. Shortening the exposure time reduces motion blurring^{83,84} at the expense of the overall image intensity. Increasing the illumination intensity can compensate for this effect. The quality of the recorded image is limited by the signal-to-background ratio, which favors photodetectors with a dynamic range large enough to capture bright fringes without saturation and dark fringes without underexposure. High quantum efficiency is not necessary and can be counterproductive, since the reference wave produces a large background signal that can saturate a high-efficiency detector. Therefore, the cooled, high quantum-efficiency, expensive cameras used in single-molecule and other precision microscopy techniques are unsuited to holographic microscopy.

Fast cameras enable experiments on fast-moving or quickly changing specimens. They require

hardware that can handle their high data rates. For example, a 1-megapixel camera operating at 1000 frames/s transfers 1 GiB/s of 8-bit grayscale images to a computer. This computer needs a fast interface — the latest USB, 10-gigabit ethernet, or a proprietary connection, often operating on a dedicated controller card — a fast internal bus to transfer the data, and a solid-state drive with a high write speed. We recommend a computer with the latest PCIe (Peripheral Component Interconnect express) bus for rapid, parallel data transfer and, ideally, a large amount of random access memory (RAM) to buffer the data stream. Many cameras come with their own proprietary control software, but the academic community has also developed open-source software such as μ Manager⁸⁵, which can be used to control various models of camera and the microscope itself.

Some processes, such as cells flowing through a channel at high speed⁸⁶, may be so fast that features of interest are blurred even at the shortest camera exposure times. For such processes, we pulse a laser diode to illuminate the samples for a short time (microseconds), as in strobe photography. Many cameras include synchronization input and/or output ports. We use these ports to synchronize the camera and laser diode with each other or with a pulse generator^{87,88}.

2.2 RESULTS

Holograms encode comprehensive information about the position and composition of individual particles or biological specimens. In a model-based analysis, we extract this information by fitting a generative model to the hologram^{65,66,68,89,90,91}, by analyzing the hologram with a trained machine-learning system^{92,93,94}, or by some combination of the two. Although all three approaches require minimal processing of the hologram, some preprocessing is beneficial for reliable results. We typically normalize holograms by subtracting the dark count from both the raw hologram and background and then taking their ratio⁹⁵, as shown in Figure 2.3. These linear transformations remove instrument-dependent effects and facilitate comparison to models. We obtain dark counts by

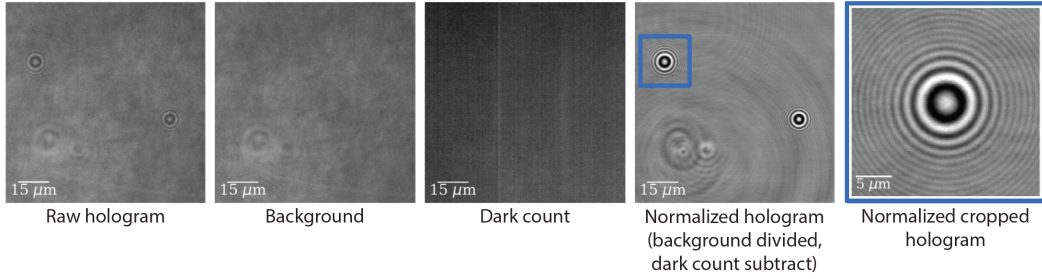


Figure 2.3: Data normalization for hologram analysis. To normalize a hologram, we subtract a frame-averaged dark count (middle) from a raw hologram (far left) and then divide by a dark-count-corrected background image (second from left). We then crop the normalized hologram (second from right) around the feature of interest associated with a particle (far right). The extent of the cropped hologram depends on the size of the specimen and its distance from the focal plane.

recording images with the illumination off, and we obtain background images by recording fields of view with no particles in frame, ideally at the same axial position as the data.

After normalization, we crop the hologram to the region of interest, which is typically a few hundred pixels wide. The size of the cropped hologram should be large enough to capture many hologram fringes, but small enough to avoid overlap with nearby objects. We automate this process by using algorithms based on Hough transforms^{83,96,97} or machine learning^{93,94}.

The computational power required to extract information about the specimen depends on the number of pixels in the hologram. However, the fringes of a hologram are often symmetric, and therefore much of the information is redundant. Consequently, most of these pixels can be discarded. Dimiduk and Manoharan found that by randomly selecting⁹⁸ just 2.5% of pixels and discarding the rest, they could accurately analyze holograms while reducing computational time by an order of magnitude⁹⁹. Selecting a random subset of pixels is now a standard part of our hologram pre-processing routine.

2.2.1 GENERATIVE MODELING

To explain the generative modeling approach, we first consider inferring physical information about a single spherical particle from its hologram, as shown in Figure 2.4. A generative or forward model can realistically simulate the hologram of such a particle as a function of its position, size, and optical properties. One can then fit the model to the data to infer these parameters. The simplest fitting approach is to iteratively modify the parameters until the differences between the model and data are minimized.

A generative model of a single spherical object might use Lorenz-Mie theory⁶⁴ — the exact solution to Maxwell’s equations for scattering from a spherical particle — to calculate the scattered field. It would then simulate a hologram by calculating the interference between this field and a planar reference wave^{65,66}. Such a model includes six parameters: the size and refractive index of the sphere, its 3D position, and α , the phenomenological parameter from Eq. 2.1. The hologram recorded on the detector is treated as a magnified image of the hologram at the objective’s focal plane.

To fit this model to a recorded hologram, one can use a nonlinear least-squares method such as the Levenberg-Marquardt algorithm¹⁰⁰. If the fitting algorithm is given a good initial guess, it can find parameter values that globally minimize the discrepancy between the model and the recorded hologram. Fitting the single-sphere model to data yields precise estimates of the sizes, optical properties, and 3D positions of individual colloidal particles⁶⁶. This approach has been applied to measuring diffusion^{101,102}, quantifying interactions between a sphere and fluid interface^{11,12,13}, tracking particle motion in an optical trap^{103,104,105}, differentiating species of particles within a mixture^{93,106,107,108}, measuring the growth of colloidal particles during chemical synthesis¹⁰⁹, and inferring the refractive index¹¹⁰ and rheological properties¹¹¹ of the medium in which the spherical particles are embedded.

Perhaps more surprisingly, the single-sphere model is a useful approximation for non-spherical

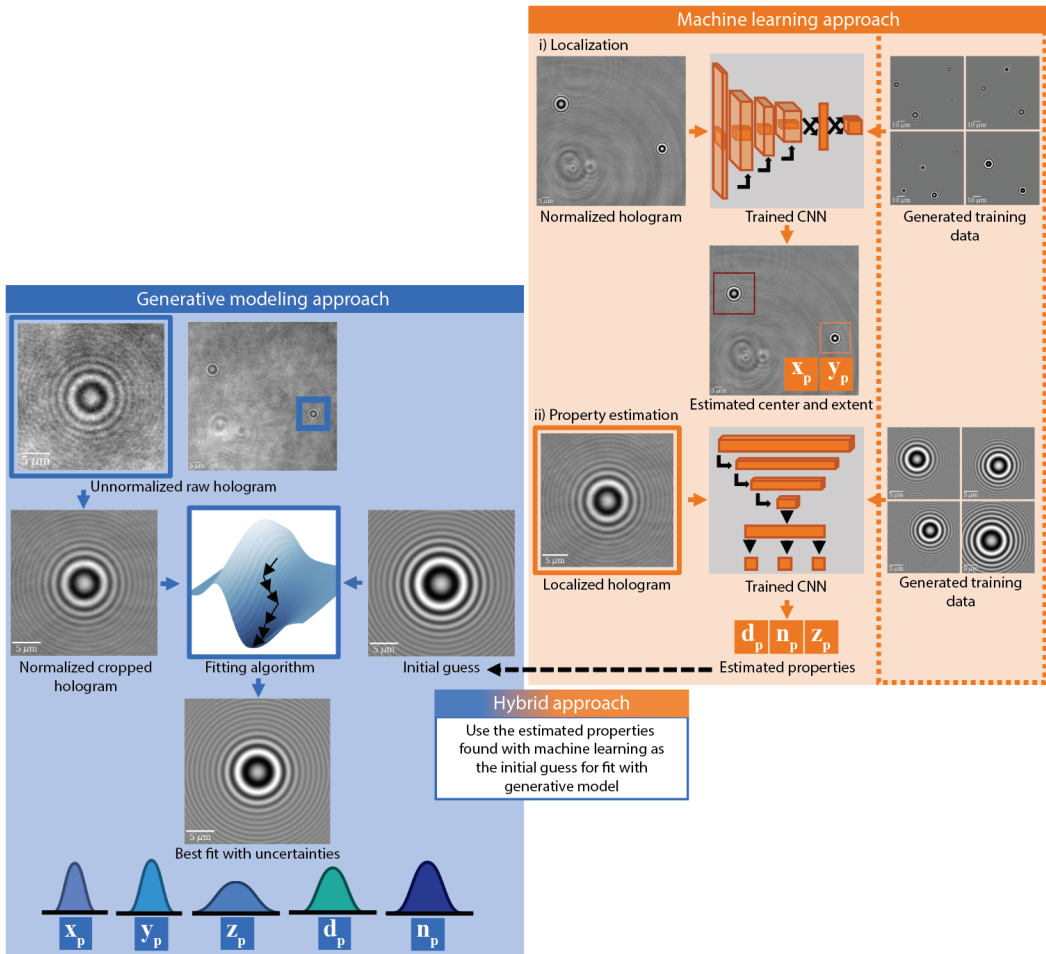


Figure 2.4: Approaches to quantitative analysis of holograms. A flow chart of approaches to hologram analysis, in which a single colloidal sphere serves as an example specimen. In a machine-learning approach, neural networks trained with generated data detect, localize, and estimate the properties of particles. In the localization module, an object-detection convolutional neural network (CNN) detects any holographic features in a normalized field of view and determines the center, x_p and y_p , and extent of each detected feature. A property-estimation module, which is also a CNN, estimates the particle's diameter d_p , refractive index n_p , and axial position z_p from the cropped holograms. In a generative modeling approach, the first steps are normalizing and cropping the field of view around the hologram of interest, which is automatically detected with a Hough transform. A nonlinear least-squares or MCMC algorithm then fits a generative model of hologram formation to this cropped hologram. A nonlinear least-squares fit requires an initial guess, which can be informed by experimental expectations, and returns the best-fit parameters and their uncertainties. In the hybrid approach, a machine-learning module first estimates the parameters, and a fitting module then refines these estimates using the parameters from the machine-learning module as the initial guess to the fit.

objects like dimpled spheres⁹⁵, protein aggregates^{108,112}, colloidal aggregates^{113,112}, and dimers of colloidal spheres¹¹⁴. The advantage of using a single-sphere approximation to model these systems, compared to a more realistic model, is that the single-sphere model can be fit more rapidly to the data. The speed of fitting makes it particularly useful for high-throughput applications, such as industrial quality assessment and process control¹¹², wastewater treatment¹¹⁵ and slurry analysis^{108,116}, in which particle size and composition must be determined continuously in real time.

Where analysis speed is not the primary concern, Bayesian parameter estimation can yield more detailed information on uncertainty and can more easily incorporate prior information than nonlinear least-squares fitting. A nonlinear least-squares fit yields a single set of parameters that best fits the data, while a Bayesian analysis yields the posterior probability density (posterior) of all possible combinations of parameters. Peaks in the posterior correspond to sets of parameters that fit the data well and are not excluded by any prior information. The prior information might include a previous calibration of the particle size distribution or the anticipated refractive index of the material. The width of a peak in the posterior characterizes the uncertainty of the parameter estimates.

The Bayesian approach can also determine marginalized uncertainties (Figure 2.4), which account for correlations between parameter estimates⁹⁹. For example, the best-fit particle size is typically correlated to the axial position, since both affect the fringe spacing. If one cares only about the particle size, one can marginalize — or integrate out — the axial position, effectively incorporating its correlations into the uncertainty of the size estimate. Marginalization yields realistic uncertainties. It is particularly useful for fundamental studies that test theories of dynamics or interactions, and for applications that have specified tolerances — for example, on particle size.

More complex generative models can be used for non-spherical specimens. Exact solutions to Maxwell's equations exist for spheroids, ellipsoids, spherocylinders, coated spheres, and small collections of spheres¹¹⁷. There are also numerical models for these shapes and for many others, including those with no exact solutions⁶⁸. Generative models for these specimens, like models for single

spheres, calculate the scattered field and simulate its interference with a planar reference wave. But models of non-spherical specimens have additional parameters such as shape, orientation, or multiple refractive indices and radii. Consequently, it takes more time to fit such models to the data.

Generative models can also account for the effects of the microscope's optical train. The single-sphere model approximates the scattered field poorly when the particle is close to or below the focal plane. The inaccuracies of the model therefore limit the depth of field available for particle tracking. To circumvent this problem, Leahy and coworkers modeled the effects of an objective lens on the hologram of a spherical particle and then fit this model to data. They found that for a $2.4\text{ }\mu\text{m}$ sphere imaged with a water-immersion lens, the region of accurate tracking increased by a factor of two relative to a lens-free model¹¹⁸. Martin and coworkers showed that extending this model to incorporate the effects of spherical aberration, a common aberration in optical microscopy, increases the accuracy of particle characterization⁸¹. These lens models work with scattering models for either spherical or non-spherical objects. For non-spherical objects, they are slow because they must numerically integrate the scattered field to calculate the effect of the objective¹¹⁹. For spheres, they are quick because the integral can be analytically simplified.

A Bayesian approach is useful for more complex models because it can account for the many ways a model might fit the data. Consider a capsule-shaped bacterium that has a small shape asymmetry between its head and tail. Even if the generative model includes this asymmetry, fitting might not unequivocally determine the bacterium's orientation from the hologram. In the presence of noise, both orientations might fit the data equally well. In this case, the posterior would show two modes, one for each orientation, accurately reflecting the uncertainty in the measurement. This uncertainty can then be propagated to other quantities. If prior information excludes one orientation — for example, if the bacterium is swimming in a known direction — this information would be reflected in the posterior, which would have a single peak.

For the Bayesian approach, we use Markov-chain Monte Carlo (MCMC) methods¹²⁰ to cal-

culate the posterior probability and to obtain marginalized uncertainties. Some MCMC methods require a good initial guess, which can be obtained using algorithms such as covariance matrix adaptation evolution¹²¹. Other methods, such as Hamiltonian Monte Carlo¹²² and parallel tempered Markov-chain Monte Carlo sampling¹²³, do not require a good initial guess. We use these methods to efficiently explore the high-dimensional parameter spaces of complex models.

The choice of generative model depends on the experimental aims. When the aim is to track a spherical object in 3D, we recommend a generative model that includes lens effects. With such a model, one can fit holograms above and below the microscope focal plane. When the aim is to characterize the properties of spherical objects, we recommend using a generative model that accounts for spherical aberration. Such a model enables more accurate quantification. When the aim is high-throughput characterization, we recommend using a single-sphere approximation, which allows real-time analysis. One rarely has to write the generative model from scratch. Open-source packages such as HoloPy¹²⁴ and pylorenzmie include generative models for different types of particles and lens effects. They also include nonlinear least-squares and MCMC methods to fit these models to data. Tutorials are available for HoloPy and pylorenzmie.

2.2.2 MACHINE LEARNING ANALYSIS

Machine learning offers alternatives to conventional algorithms for feature identification^{125,126}, particle tracking¹²⁷, and quantitative hologram analysis^{58,65,66}. As with the generative modeling approach, the aim is to determine an object’s position and properties directly from its hologram. But instead of modeling the physics of image formation, convolutional neural networks (CNNs) or support vector machines (SVMs) recognize, classify, or characterize objects based on training data. In general, machine-learning approaches work well on problems with many degrees of freedom; they recover low-dimensional solutions that classify or characterize the data¹²⁸. For holography in particular, machine learning approaches are well-suited to problems where generative modeling is

computationally expensive, such as characterizing particles in a high-throughput experiment.

We use machine-learning approaches to tackle three types of analysis problems in holography: localization — estimating the hologram’s center and extent in the field of view^{93,94,129}; property estimation — characterizing the object’s refractive index, diameter, and axial position^{92,130}; and classification — differentiating and labeling the structure of the particle¹³¹. Combining the modules used for each of these analysis steps results in a full end-to-end analytical pipeline for holograms⁹⁴.

Each of these three tasks requires training a model. Training consists of feeding holographic image data with known parameters — such as known particle size and position — to the model, which learns to recognize patterns in the data and the parameters. In many machine-learning applications, one must gather and manually annotate training data. The cost of human labor in this process limits how much training data can be produced, and thus reduces the model’s accuracy. The application to holographic microscopy has an advantage because the generative models can rapidly generate large amounts of properly annotated training data.

The amount of training data needed for an analysis task depends on the size of the parameter space and the desired precision of the classification. For the training data to span the range of interest $R(p_j)$, where p_j is one parameter in a set of M coupled parameters, and Δp_j is the desired resolution of that parameter, the number of training elements must scale as

$$N \leq \prod_{j=1}^M R(p_j)/\Delta p_j; \quad (2.2)$$

where the upper limit corresponds to calculating every possible solution. For non-spherical objects, the training data must span all possible orientations, positions, sizes, and refractive indices. Sampling approaches can reduce the number of elements below the upper bound.

To better match experimental conditions, one can intentionally degrade the simulated holograms with either uniform Gaussian noise⁹⁴ or noise directly extracted from the experimental holograms,

including both camera noise and time-varying fluctuations¹³¹. Adding noise prevents the model from overfitting experimental data, thereby improving the accuracy of the results^{94,131}.

Training involves optimizing the parameters of the model to accurately fit the labeled training data. A variety of optimizers are available, including Adam¹³², root-mean-square propagation, and stochastic gradient descent¹³³. Activation units such as ReLU enable the model to learn complicated functions and facilitate rapid training¹³⁴. In our experience, training speed is limited by how quickly training data can be generated, though that process can easily be parallelized and is a one-time cost. With current computing clusters, we can generate data and train a model in a few hours¹³¹.

The first step in hologram analysis is localization, which involves finding the regions of interest in a hologram that correspond to particular objects, as shown in Figure 2.4. CNNs are particularly well suited for object detection and localization^{92,94,135}. We first train the CNN on synthetic holograms with variable numbers of particles. The CNN then takes a grayscale image input and returns a set of cropped images centered on each particle, along with the estimated parameters of the hologram center, x_p and y_p , and extent of each detected feature. We can then use the number of identified features to measure particle concentrations or pass each cropped hologram to another module for further analysis.

Machine-learning algorithms are both more accurate and more robust than conventional object detection algorithms^{83,126}, yielding much lower rates of false positive and false negative detections. The localization algorithm used by Altman and coworkers⁹⁴, for example, missed fewer than 0.1% of simulated holograms across a wide range of particle sizes, refractive indexes, and positions. By contrast, conventional algorithms missed up to 40%. This ability to detect particles over wide regions of the parameter space is necessary for robust, unattended particle tracking and characterization.

After localizing and cropping the hologram, we use other machine learning systems, such as

CNNs^{94,130} or SVMs⁹², to estimate the properties of the objects. First, we scale the block of pixels identified in the localization stage down to a standard size, which enables the algorithm to accommodate holograms with different extents in the camera plane. The network then reduces the dimensionality of the data until it outputs values for the particle properties, including diameter d_p , refractive index n_p , and axial position z_p .

Although the generative modeling approach yields more precise and accurate property estimates, machine learning is faster and more flexible⁹⁴. End-to-end processing of a full-frame hologram takes 30 ms or less⁹⁴. In addition, machine-learning models require little tuning or prior knowledge of the system, and they are more resilient to artifacts that can hinder the performance of generative models⁹⁴.

Machine-learning methods can also classify the structure of a specimen. For example, CNNs can recognize and differentiate clusters of colloidal particles bound by short-range attractions¹³¹. Because the range of the attraction in such clusters is only about 10% of the particle diameter, standard optical microscopy techniques cannot easily distinguish bound and unbound particle pairs. Furthermore, the computational cost of fitting a model to the hologram is high. Klein¹³¹ instead detected differences in cluster configurations using a standard, pretrained CNN image classifier¹³⁶ that was retrained with simulated holograms augmented with experimentally extracted noise. The retrained CNN extracted hierarchical features from the hologram and classified them to determine the configuration of particles. Klein found that after including experimentally extracted noise in the training data, the retrained CNN could differentiate six different ground states of a seven-particle cluster — including two states differing by only one pair of bound particles — with 60-80% accuracy.

A free, open-source software⁹⁴ — Characterizing and Tracking Colloids Holographically (CATCH) — is available for end-to-end analysis of holograms from spheres and other particles that can be usefully modeled as spheres. A tutorial is available. For other applications, models must be built and

trained. However, the architecture of the neural network does not need to be rebuilt for each problem; instead, existing machine-learning frameworks for image analysis can be used¹³¹.

2.2.3 HYBRID APPROACHES

Current machine-learning methods for analyzing holograms are fast and robust, but not as precise or accurate as generative modeling approaches. Conversely, generative modeling approaches are highly precise and accurate, but incur higher computational costs than machine-learning methods. A hybrid approach offers the best of both worlds: fast, automated analysis with high precision.

A hybrid analysis pipeline begins with a machine-learning stage. From a full-frame hologram, a trained network automatically localizes and crops holograms corresponding to individual objects. It then estimates their properties, which might include their refractive indices, diameters, and axial positions. In a second stage, an algorithm fits a generative model to each cropped hologram, using the machine-learning estimates as initial guesses.

Machine learning eliminates the need for human input to the fitting routine. The algorithm determines the number of objects in the field of view, the extents of their holograms, and the initial guesses required to fit the model to the data. This hybrid approach also enables fully parallel analysis of time-series data. In a generative modeling approach, one usually derives initial guesses for each frame in a time-series from the best-fit parameters of the previous frame. Consequently, the frames must be analyzed sequentially. But the machine-learning approach provides initial guesses for all frames, which one can use to fit generative models to all frames in parallel.

In principle, machine-learning approaches could also select the appropriate generative model by classifying the structure and shape of the specimen. Such an approach could automate the entire hologram-analysis pipeline.

2.3 APPLICATIONS

The direct analysis of holograms has enabled new, high-precision measurements of colloids, soft materials, and biological systems. In this section, we highlight a few examples.

2.3.1 COLLOIDAL DYNAMICS AND SELF-ASSEMBLY

The precision enabled by the generative modeling approach was crucial to discovering an unexpected feature of colloidal systems. Since the early 20th century, it was known that micrometer-sized solid particles could stick irreversibly to the interface between two fluids¹³⁸. This phenomenon, driven by surface tension, is the basis for making the solid-stabilized Pickering emulsions now used in foods¹³⁹, oil recovery¹⁴⁰, and many other applications^{141,142}. The interface can also serve as a scaffold that guides the self-assembly of these colloidal particles¹⁴³. Until recently, it was assumed that the particles would approach the interface, breach it, and then immediately reach an equilibrium position, as shown in Figure 2.5a.

Holographic microscopy showed that, contrary to initial assumptions, the particles take a long time to relax to equilibrium after they breach the interface. Kaz, McGorty, and coworkers¹¹ used radiation pressure to push a particle upward to a planar oil-water interface while measuring its height using a holographic microscope. By fitting a single-sphere generative model to the holograms, they were able to measure the height to nanometer-scale precision on millisecond time scales (Figure 2.5a). With this combination of high spatial precision and high temporal resolution, they observed the motion of the particle immediately after the breach and showed that it scales logarithmically with time (Figure 2.5a). The long duration of the measurement allowed them to observe this scaling over multiple decades and enabled comparison with theory. The logarithmic behavior is a signature of pinning and depinning of the three-phase contact line on the particle, which leads to surprisingly long relaxation times — on the order of months for a micrometer-scale particle.

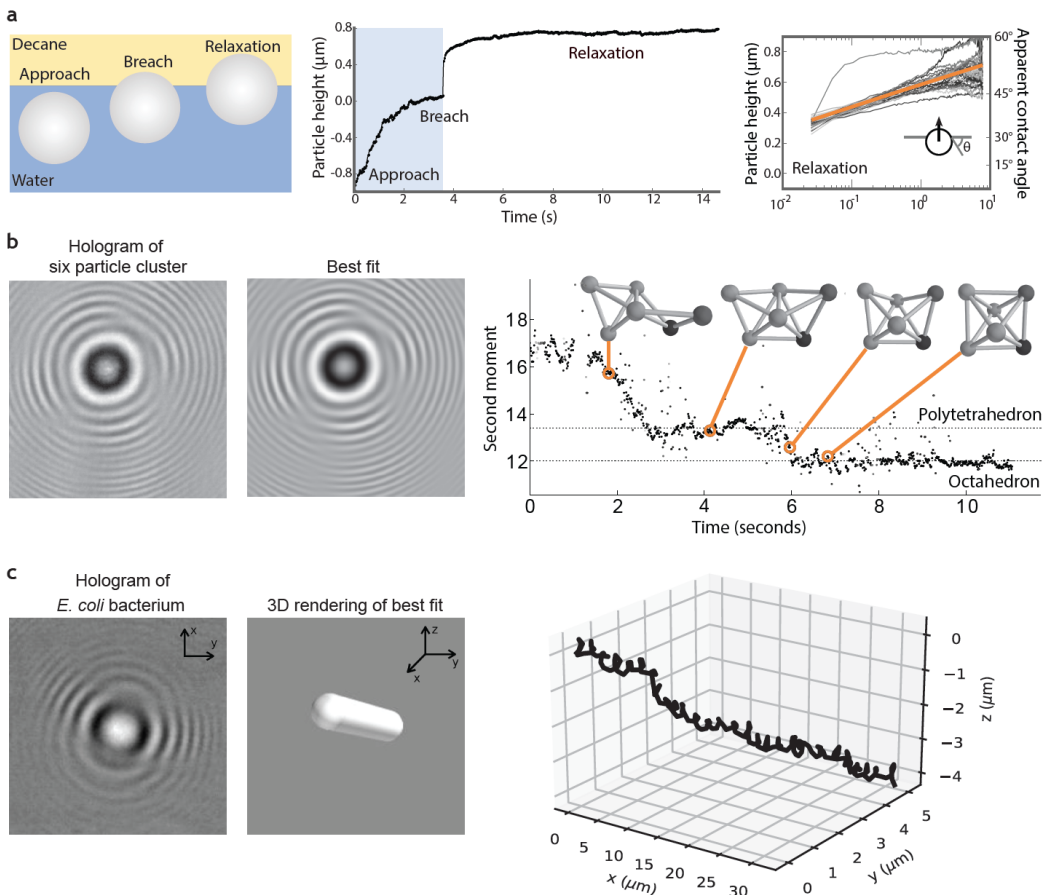


Figure 2.5: a) Diagram of a colloidal particle approaching and breaching an interface between two fluids (left). Plot showing the position of a particle before and after the breach (middle). The high-precision tracking of holographic microscopy shows that the particles relax logarithmically in time to equilibrium (right). Each curve corresponds to a measurement of a single particle (data from Kaz, McGorty et al. ¹¹). b) Fitting a generative model to holograms of a six-particle cluster of interacting spherical particles reveals transitions between states. The raw hologram is shown alongside the best-fit hologram (left). The results of the fits quantify the evolution of the cluster structure, represented by the second moment of the mass distribution. The full structures are shown as ball-and-stick models for four time points highlighted in orange (figure adapted from Perry et al. ¹³⁷). c) A hologram of a single *E. coli* bacterium (left) shows asymmetry in the fringes. Fitting a generative model of a spherocylinder (middle) to this hologram yields estimates of the orientation and position of the bacterium as it swims. The high positional and angular precision reveal a helical wobble, clearly distinct from Brownian motion, in the swimming pattern, shown in the 3D plot (right), adapted from Wang et al. ⁴⁶.

Later holographic microscopy experiments showed that this long-time relaxation is common to many different types of colloidal particles^{12,13,14}. Wang and colleagues⁶⁷ showed that when ellipsoids breach an interface, the particles rotate far more slowly to equilibrium than previously predicted. They revealed this motion by fitting a generative model for scattering from an ellipsoidal particle as a function of orientation and position. These studies illustrate how the generative-modeling approach leverages the strengths of holographic microscopy: its acquisition speed, high dynamic range, and sensitivity to the 3D position and orientation of the particle.

Holographic microscopy is also well suited to answer questions about how colloidal particles interact and diffuse. The structure and dynamics of these systems are difficult to determine with standard optical microscopy because the interactions are so short ranged — a few tens of nanometers — and because the particles diffuse in three dimensions. Using holographic microscopy, Fung and coworkers imaged the 3D motion of pairs of interacting colloidal particles with high temporal resolution. They resolved the translational, rotational, and vibrational motion of the particles — and their interaction potential — by fitting generative models that account for scattering from multiple spherical particles, including near- and far-field couplings between the scattered fields^{69,144}. Perry and coworkers¹³⁷ used a similar approach to infer the 3D dynamics of self-assembled colloidal clusters as they transitioned between free-energy minima (Figure 2.5b). The structure and dynamics of these systems can give insights into the first stages of crystal growth and the mechanisms of self-assembly in colloidal systems. The precision of this measurement was sufficient to resolve transitions between two free-energy minima for a six-particle cluster, which was not possible with wide-field or confocal optical microscopy.

2.3.2 MICRORHEOLOGY AND STRESS MEASUREMENTS

Measurements of colloidal dynamics can not only reveal information about the physics of interacting systems, but can also reveal information about materials in which colloidal particles are embed-

ded. In microrheology, for example, one infers the viscoelastic properties of a material by measuring the Brownian motion of embedded tracer particles¹⁴⁵. In traction-force microscopy, one infers the forces exerted by living cells by measuring the motion of particles embedded in an elastic substrate that deforms as the cells move on it¹⁴⁶. In both cases, one needs to detect small displacements of the particles. Typically, a confocal or a standard widefield optical microscope is used, but a holographic microscope has advantages.

Microrheological measurements benefit from the higher precision of the holographic microscope. Modeling and fitting a time-series of holograms reveals the motion of tracer particles with nanometer-scale precision. The diffusion coefficient^{69,144,147} of the particles and the viscoelastic properties of the medium can then be inferred from this 3D motion data. Cheong and coworkers¹¹¹ used this approach to precisely measure the complex viscoelastic moduli of polysaccharide gels, obtaining accurate measurements in micrometer-scale samples without mechanical loading.

Traction-force measurements benefit from the depth of field of the holographic microscope. Makarchuk and coworkers¹⁴⁸ obtained the full 3D displacement map of tracer particles without scanning the focus of the microscope. They also measured the displacements to nanometer-scale precision. Though their technique did not use a generative model, it did involve directly analyzing the hologram fringes to measure the forces exerted by colorectal cancer cells. The application of holography to traction-force microscopy could enable both higher time resolution and characterization of forces on stiffer substrates, where the embedded particle motion is subtler.

2.3.3 MICROORGANISMS AND ORGANELLES

Holographic microscopy can also measure the properties and motion of biological systems. Fluorescence microscopy is commonly used for such systems because fluorescent labeling offers excellent contrast for the object of interest. But labels can also interfere with biological systems. Furthermore, photobleaching limits the number of detected photons and hence the duration of experiments¹⁴⁹.

Because holographic microscopy is based on scattering, the number of photons that can be detected is unlimited. Instead, the precision and speed are limited by the scattering strength of the sample. Biological systems tend to scatter weakly because their refractive indices are usually close to the index of water (1.33). The refractive indices of living cells, for instance, are around 1.38 or smaller^{150,151}.

However, even weakly scattering microorganisms such as *E. coli* can be seen under the holographic microscope. The small scattering cross-section of an individual *E. coli* bacterium — which is about 2 μm long and has a refractive index of 1.388¹⁵² — makes it difficult to see in a brightfield optical microscope. Wang and coworkers⁴⁶ were able to use holographic microscopy to capture the 3D swimming motion of these bacteria, including its tumbling, as shown in Figure 2.5c. To obtain this information, they first modeled a bacterium as a homogeneous spherocylinder. They then fit a generative model of scattering from a spherocylinder to the data. This technique allowed them to measure both the position and orientation of individual bacteria as a function of time. Using the high acquisition speed of the microscope, they resolved even the wobble of the bacterium during its run-and-tumble motion, as shown in Figure 2.5c.

Holographic microscopes can also image vesicles, another class of weakly scattering systems that are biologically important. Vesicles are enclosed lipid bilayers that serve as models for organelles. They are used to deliver drugs¹⁵³, study the origins of life¹⁵⁴, or create artificial cells^{155,156}. In these applications, the solute loading of the vesicle and its motion must be tracked over time. This is a non-trivial task because bilayer is thin (about 5 nm). Consequently, the vesicle has a small scattering cross-section¹⁵⁷. But when the vesicle is filled with, for example, a sugar solution, its scattering cross-section increases, and interference fringes become visible under the holographic microscope, as shown in Figure 2.6a. One can fit a generative model for a core-shell spherical particle to holograms of such filled vesicles — where the core is the filling solution and the shell is the thin outer layer of lipids. The fit reveals the vesicle's refractive index and size, which can be used to quantify vesicle loading¹⁵⁸.

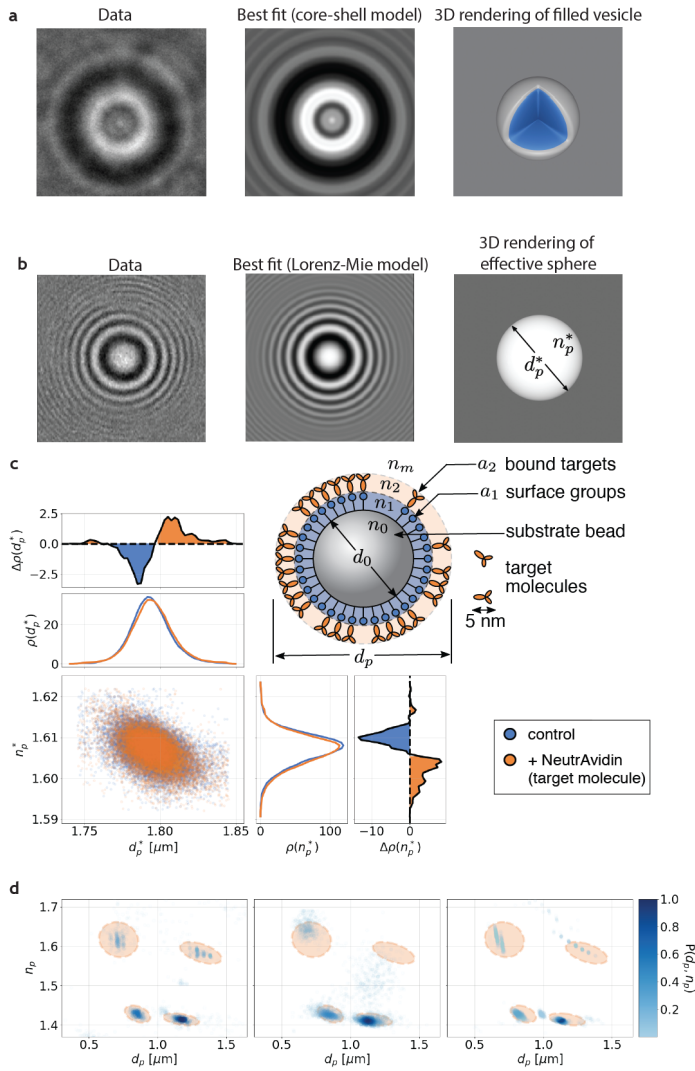


Figure 2.6: Property estimation and characterization. a) Hologram of a vesicle encapsulating 500 mM sucrose, alongside the best-fit hologram from a core-shell model and a 3D rendering of the best-fit vesicle, shown with a cut-away of the enclosed fluid (data and fit from Tran et al. ¹⁵⁸). b) Hologram of a spherical bead that binds target molecules, alongside a best-fit hologram from an effective-sphere model, which treats the substrate bead and molecular layers as a single homogenous sphere. The fit defines the effective diameter and effective refractive index (right) (data and fit from Altman et al. ¹⁵⁹). c) Results from the effective-sphere analysis for avidin binding to biotinylated polystyrene spheres (adapted from Altman et al. ¹⁵⁹). Plots show the distributions of inferred particle diameters $\rho(d_p)$ and refractive indexes $\rho(n_p)$ from control beads (blue), probe beads after binding (orange), and differences. Binding causes a statistically significant shift in $\rho(d_p)$ on the order of a few nanometers. (d) Inferred parameters for a heterogeneous, four-particle mixture from a generative modeling approach (left), a machine-learning approach (middle), and a hybrid approach (right). The results show how well each method differentiates components of the mixture, which contains two sizes each of polystyrene and silica spheres. Ovals mark 99% confidence intervals of the generative modeling results. Color denotes the relative probability density of the parameters, $P(d_p, n_p)$ (adapted from Altman et al. ⁹⁴)

2.3.4 DETECTION OF MOLECULES

Macromolecules, such as enzymes or proteins, are too small to see with a typical optical microscope because they don't scatter enough light. One can detect them by fluorescently labeling them and measuring their fluorescence when they bind to a functionalized bead. As in other fluorescent measurements, labeling adds a step to the detection process, and labels can interfere with binding^{160,161}.

Holographic microscopy offers an alternative approach that does not require fluorescent labeling. As in the fluorescence assay, one first functionalizes micrometer-scale probe beads with surface groups that bind specifically to targets of interest, such as virus particles, antibodies, or other proteins. One then records holograms of individual particles and fits these holograms with an effective-sphere generative model. Fitting reveals binding-induced changes in the inferred parameters¹⁶². The observed shift in effective diameter, for example, can be related to the coverage of bound targets.

This approach allows both rapid fitting and high sensitivity. When the molecules bind, they increase the effective diameter of the beads by a few nanometers, a difference that the holographic microscope can detect¹⁶³. The resulting fits are precise enough to isolate changes in population distributions as the target molecules bind, enabling applications such as fluorescence-free immunoassays, as shown in Figure 2.6b and c^{159,164}.

The validity of the effective-medium approach has been assessed in simulations based on the discrete-dipole approximation^{68,70,71,165}. This approximation treats an inhomogeneous object as a set of point dipoles and allows computation of the scattered field of arbitrarily shaped objects. These simulations also show that one should use a low-index material for the probe bead, relative to the refractive index of the molecular coatings, to observe the greatest shift in effective diameter after binding. Future experiments might therefore employ a silica probe bead, with refractive index $n_p = 1.4$, instead of polystyrene, with $n_p = 1.6$.

2.3.5 CHARACTERIZING INDUSTRIAL DISPERSIONS

For many applications involving industrial dispersions, evaluating the efficacy and safety of the product requires detecting and differentiating multiple species of particulate contaminants and measuring their relative concentrations in dispersion. Hologram microscopy combined with the effective-sphere analysis approach is especially well suited to such applications. This method can analyze multiple particle species in wastewater or industrial slurries with high throughput^{108,112,116}. In these applications, contaminants or large aggregates appear as outliers in the continuous, real-time analysis of particle size and composition.

This method also has applications in the monitoring and development of biopharmaceuticals. The active ingredients of these complex medicines are proteins that can aggregate, compromising the medicine's effectiveness and potentially causing harmful immune response. Winters and coworkers¹⁰⁸ used holographic microscopy and an effective-sphere model to successfully differentiate multiple components of a model biopharmaceutical formulation, including silicone-oil emulsion droplets, fatty-acid clusters, and potentially dangerous protein aggregates. While many of these populations have a wide polydispersity in size, they can be distinguished by their common refractive index, indicating their similar composition. Characterizing the particles' size and composition differentiates the populations of these different species with high throughput and allows their concentrations to be measured accurately. Monitoring the concentration and composition of particles dispersed in biopharmaceutical products is useful for guiding product formulation, performing quality assurance during manufacturing and assessing product stability.

2.4 REPRODUCIBILITY AND DATA DEPOSITION

Reproducible, quantitative analysis with holographic microscopy requires recording and disclosing experimental metadata, storing large data sets and reporting the prior probabilities and techniques

used in the analysis. The metadata are essential for interpreting recorded holograms. Metadata include both laser settings — such as wavelength, polarization and intensity — and imaging settings — such as pixel spacing, frame rate and exposure time. To determine the pixel spacing, we image a graticule, and then divide the distance between markings by the number of pixels spanning that distance. We recommend recording all metadata in the same file as the hologram and maintaining these metadata throughout hologram processing and analysis. Both HDF5 and TIFF files support storing metadata alongside data.

Some video recording formats are unsuitable for quantitative holographic imaging because they use lossy encoding to reduce file size. Lossy formats introduce artifacts into recorded images that can alter extracted results. The data should instead be saved as an uncompressed video or in a format that uses lossless compression, such as HDF5 or TIFF.

To store a time series of recorded holograms, which has a size typically in the order of gigabytes, we recommend using standard, non-proprietary formats such as HDF5. HDF5 has several advantageous features for holography: it is designed for large data sets, it can store data in a compressed format and implementations such as the h5py Python package enable HDF5 files to be loaded piecewise, so that they do not consume all of the computer’s RAM.

Equally important to experimental metadata are parameters associated with hologram analysis. It is essential to disclose all assumptions, including the generative model and the prior probabilities, which are probability distributions in a Bayesian analysis but could also take the form of bounds placed on parameters. Algorithmic parameters should also be disclosed, such as the convergence criteria for non-linear least-squares fitting, the number of chains for MCMC sampling or the number of temperatures for parallel tempered MCMC sampling. In a machine-learning framework, the underlying algorithm architecture and the training data should be reported. One can disclose all of this information by creating public repositories for both data and analysis code.

2.5 LIMITATIONS AND OPTIMIZATIONS

Limits on the information that can be inferred from holograms are both physical and practical. The physical limitations do not depend on the analysis technique used. They are based on how much information is present in the hologram. For example, when the particle approaches within roughly $5\text{ }\mu\text{m}$ of the focal plane of the objective, the fringes in its hologram become too finely spaced for the camera to resolve^{81,118}. Conversely, when the particle moves too far from the focal plane, its fringes become increasingly faint and are obscured by image noise. Even under ideal imaging conditions, some combinations of particle parameters produce nearly indistinguishable holograms, which can lead to unreliable parameter estimation¹⁶⁶. Furthermore, weakly scattering objects introduce degeneracies in the generative model, making it difficult to determine, for example, the size and refractive index of the object independently. In these cases, a Bayesian inference approach with a generative model will report appropriately larger uncertainties. Finally, the presence of many objects in the specimen can make it more difficult to extract information from the hologram, because fringes from other objects disrupt the fringes of interest. Machine-learning methods can be used to isolate clean holograms of the object of interest¹⁶⁷.

2.5.1 GENERATIVE MODELLING

The main practical limitation of the generative modelling approach is that one must know what one is looking at before modelling it, a limitation not faced by reconstruction-based analyses. More specifically, the generative model must accurately describe the shape, structure and composition of the specimen. It must also accurately describe how its hologram is formed. Ignoring physical effects, such as strong aberrations, leads to systematic characterization errors⁸¹. Additional parameters in the model, such as the field rescaling parameter α , can improve the fit but may be difficult to interpret. Furthermore, even in the most complex models, the inferred parameters can depend on the

distance between the object and the focal plane. Martin *et al.*⁸¹ found that when the particle was closer than about 10 μm to the focal plane, the inferred refractive index of the particle had a variation of 6%, whereas the inferred diameter had a variation as high as 20%. Such results may indicate that the model does not account for some physical effects. To overcome these limitations, future work should focus on more descriptive and accurate generative models.

Another practical limitation is the computational cost of fitting. Fitting the more complex generative models, such as those describing the scattering from a cluster of many spherical particles, can take hours of CPU (central processing unit) time for a single hologram. By contrast, the hologram of a single sphere can be computed in under a millisecond on a desktop computer. The computational cost of detailed analysis may be prohibitive for certain experiments, such as those involving long time series or high throughput.

New developments in computing and inference could mitigate these issues. For example, algorithms such as automatic differentiation^{168,169}, variational inference¹⁶⁹, and Hamiltonian Monte Carlo¹²² can accelerate fitting models with large numbers of parameters. Additionally, graphics processing unit (GPU) and tensor processing unit (TPU) computing frameworks can parallelize the fitting of highly complex models to time series¹⁷⁰.

An alternative is to develop simpler models rather than more complex ones. The effective-sphere model is an example of a model that makes simplifying yet accurate physical approximations. This approach can reduce the burden of specifying the detailed shape and structure of the object, and can sharply reduce the computational cost. The challenge is to determine the appropriate approximation for the problem. To this end, one can test the approximations by running full scattering calculations using tools such as the discrete-dipole method⁷¹.

2.5.2 MACHINE LEARNING

Although machine-learning algorithms can perform more robustly over a wider parameter space than conventional algorithms, they can be inaccurate when their inputs differ too drastically from their training data. Imprecision in the localization algorithm, which estimates the position and extents of holograms, can also propagate uncertainty into parameters such as size and axial position⁹⁴.

The machine-learning approach is also limited by computational speed, although in a different way from the generative modelling approach. In particular, analyzing data is fast, but training can be slow because many holograms must be generated to span the parameter space. Altman and Grier⁹⁴ achieved reliable results with a training set of 10^4 images, but in the theoretical limit 10^9 images would be required to achieve the parts per thousand precision of a generative modelling approach. Because the training data can be generated and labelled automatically, achieving high-precision classification is not an intractable problem for spherical specimens. Advances in network architecture and training protocols for high-precision tracking and characterization of spherical particles may soon be practical even with modestly sized training sets. But for non-spherical specimens, which include additional degrees of freedom such as shape and orientation, it may be impractical to generate and process enough training data for accurate characterization.

Using synthetic data to train machine-learning models has some disadvantages. Experimental artifacts, such as pattern noise in the camera, can significantly compromise accuracy. To mitigate this problem, one can either improve the experimental design or modify the models used to generate the training data. For example, one can measure the camera noise and incorporate it into the generated holograms¹³¹, or generate the training data using models that more accurately describe the artifacts of the experimental system.

2.5.3 HYBRID APPROACHES

A hybrid approach can, in principle, overcome the limitations of both the generative modelling and machine-learning approach. It removes the need for human input or prior knowledge, while benefiting from the speed of machine learning and precision of fitting. Nevertheless, the hybrid approach comes with caveats. First, it remains computationally expensive because the generated training data must span the parameter space. Second, fitting the model requires calculating many holograms, although we expect fitting times to be reduced if the machine-learning stage provides a good initial guess. Third, any fundamental inaccuracies and limitations in the generative model affect the analysis in both stages. In the machine-learning stage, these inaccuracies affect the training data and, therefore, the parameter estimates. The inaccuracies in these estimates can propagate to the results of the fitting stage, as the accuracy of the fit can depend on the starting point in parameter space.

2.5.4 MORE GENERAL LIMITATIONS

It is difficult to know whether the model-based approach and in-line experimental geometry will be effective for a specimen that differs from the previous examples, or whether a different analysis or experimental technique could reveal more information. We cannot give specific information on the ranges of specimen concentration, size, shape or structure for which the approach will yield useful results. New studies are needed to probe the physical and practical limitations of analysing more complex specimens. For those interested in using the approach but unsure whether it will work on a particular specimen, our advice is to try it. The in-line geometry is straightforward to set up, and open-source software for generative modelling¹²⁴ and machine learning⁹⁴ makes it easy to apply the analysis methods.

2.6 OUTLOOK

Since its development in the 1940s, holographic microscopy has been repeatedly revitalized by technological developments. The invention of the laser simplified implementation¹⁷¹; the development of digital cameras enabled digital reconstruction¹⁷²; and the advent of computers powerful enough to compute scattering solutions of microscopic objects enabled direct analysis of holograms^{173,174}. Recent developments in statistical inference and machine learning enabled the model-based approaches and precise measurements discussed in this primer.

The future of model-based analysis depends on continued advances in inference and computation. Removing limitations, such as the variation of parameter estimates with defocus, demands more physically accurate generative models. These models must also be more computationally efficient. Currently, it takes days of CPU time to fit a complex generative model to a hologram of a two-sphere cluster if the model includes the effects of a lens¹¹⁹. Although processing power will likely increase, there is still a need for numerical and algorithmic optimization. Real-time analysis of holograms requires inference algorithms that are more efficient. These algorithms must also be resilient to the complications of real experimental systems, such as variations in brightness and loss of fringe information near the focal plane.

Machine-learning techniques are poised to meet many of these challenges. CNNs have quantified the properties of microscopic objects from real holograms taken under various experimental conditions, at speeds nearly 100 times faster than conventional inference-based techniques. However, these property estimates are not as precise as those obtained with a fitting approach, and they lack the uncertainty estimates provided by MCMC sampling. Furthermore, estimating properties such as the shape, structure and orientation of more complex specimens requires algorithms trained with a large amount of data. Machine-learning approaches rely on generative models to produce these training data. The future of the field will likely depend on the development of both approaches in

parallel.

We would go further; we think the future of holographic microscopy depends not only on the parallel development of generative modelling and machine learning but on their integration. We envision a microscope that would send its holograms directly to a system that could guess what kind of objects made them, analyse the holograms and report any parameters and uncertainties that the researcher specifies. The specimen might be a living eukaryotic cell, and the objects might be its organelles. Behind the scenes, a hybrid approach would be at work. A machine-learning module would determine the number, shapes and structures of objects that made the hologram; estimate the properties of these objects; and select a generative model for each. A fitting module would then report precise estimates and marginalized uncertainties on parameters of interest, using the results from the machine-learning module as initial estimates.

The development of these new algorithms could be synergistic with experimental design. In the broad field of quantitative phase microscopy^{59,175,176,177}, researchers leverage various experimental approaches — off-axis beam geometries, phase-shifting elements, coherence control and multi-wavelength apparatus, among others — to acquire more information and more sensitive measurements of complex specimens. Meanwhile, interferometric scattering techniques have pushed the detection limit of holographic microscopy to the single-molecule scale^{178,179}. Generative models are starting to appear for these techniques¹⁸⁰. The development of generative modelling and machine-learning approaches could drive further advances in experimental techniques, and vice versa.

This vision is not limited to holographic microscopy; it is a vision for where microscopy in general may be headed. As we noted in the introduction, a hologram is not easy for the human eye to interpret. It is difficult to visually recognize even a specimen's shape from its hologram, let alone its size or orientation. But the interference fringes that make the hologram impenetrable to human vision contain a wealth of information about the specimen. That information is most easily extracted and quantified by an algorithm. The same principle can be applied to any microscopy technique.

By removing the need for humans to directly interpret the image, we can design microscopes that maximize the amount of information contained in the image. Although the resulting images may not appeal to the eye, their true appeal lies in what they reveal about the specimen.

Much Madness is divinest Sense –

To a discerning Eye –

Emily Dickinson, *Much Madness is divinest Sense*

3

Improving generative models for holographic microscopy

The contents of this chapter have been previously published⁸¹, © 2024 Optica Publishing Group.

Reprinted under the terms of the Optica Open Access Publishing Agreement from:

“Improving holographic particle characterization by modeling spherical aberration.” Car-

oline Martin, Brian Leahy, and Vinothan N. Manoharan. *Optics Express* 29, 18212-18223 (2021)

The material in this chapter is based upon work supported by the National Science Foundation (DMR-1420570), the Harvard Materials Research Science and Engineering Center (DMR 20-11754) and the Department of Defense through the National Defense Science and Engineering Graduate Fellowship. The authors thank Ron Alexander and Solomon Barkley for useful discussions on fitting methods.

THE COMBINATION OF DIGITAL HOLOGRAPHIC MICROSCOPY, forward modeling, and statistical inference allows colloidal particles to be characterized and tracked with high precision over a large depth of field¹¹⁹. In contrast to the traditional method of interpreting holograms by reconstruction^{47,181}, where the fields scattered by the object are recovered by physically or numerically shining light through the recorded hologram, in forward-modeling approaches a scattering theory is directly fit to a minimally processed hologram^{65,66}. This approach yields estimates of the particle's three-dimensional position, index of refraction, and size. The forward-modeling approach has the advantage that the position and properties of the object can be inferred directly from the hologram, whereas reconstructions must be further processed to recover this information. When the objects are spheres approximately as large as the wavelength, their reconstructions often do not resemble spheres⁷², making it difficult to precisely extract their positions from the reconstruction. Furthermore, the forward-modeling approach yields estimates of the particle's index of refraction, which cannot be directly inferred from a reconstruction. The precision of the quantities inferred from forward-modeling and fitting, combined with the high acquisition speed of the holographic microscope, make the approach useful for many applications, including microrheology¹¹¹, visualizing the dynamics of colloidal clusters¹⁴⁴, and studying bacterial swimming⁴⁶.

However, the most commonly used forward models ignore optical aberrations, which exist in all

imaging systems. Not modeling such aberrations can lead to systematic errors in the inferred parameters. Although many techniques have been demonstrated to correct for the effects of aberrations and artifacts on reconstructions^{182,183,184,185,186,187,188,189}, there has been little work on accounting for these effects in forward models. Recent models do include the phase effects introduced by an ideal objective lens^{118,119}, but they do not include aberrations in either the objective or experimental setup. Moreover, the effects of aberrations on the accuracy of parameters inferred through model-based approaches have not yet been examined.

It is important to understand the effects of aberrations because most microscopy experiments are subject to them. Here, we focus on spherical aberration. Although most high-quality objectives are corrected for spherical aberration near focus, holographic microscopy is often used to image particles far from the focal plane, where the aberration may be less well corrected. Furthermore, the interface between a liquid sample and a glass coverslip can lead to spherical aberration when the refractive index of the objective immersion fluid is not matched to that of the sample medium⁷⁷. Water-immersion objectives are therefore used to minimize aberrations when aqueous samples are imaged. But even with a water-immersion objective, spherical aberration can be introduced by the coverslip interface. This aberration can be corrected by setting the objective's correction collar, which adjusts the position of a movable central lens group within the objective (Figure 3.1a), to the thickness of the coverslip, which is typically 0.10 mm to 0.20 mm. If the correction collar is set incorrectly, however, spherical aberration is induced. Thus, unless the microscopist carefully measures the thickness of each coverslip—a laborious task when many samples must be imaged—the holograms will likely be subject to spherical aberration. To maximize the precision of tracking and characterization, we must therefore consider the effects of aberrations that can be induced by the experimental setup, as well as those inherent to the objective.

In this chapter, we experimentally examine the effects of spherical aberration on holograms captured in an in-line holographic microscope and develop a model to describe these aberrations. We

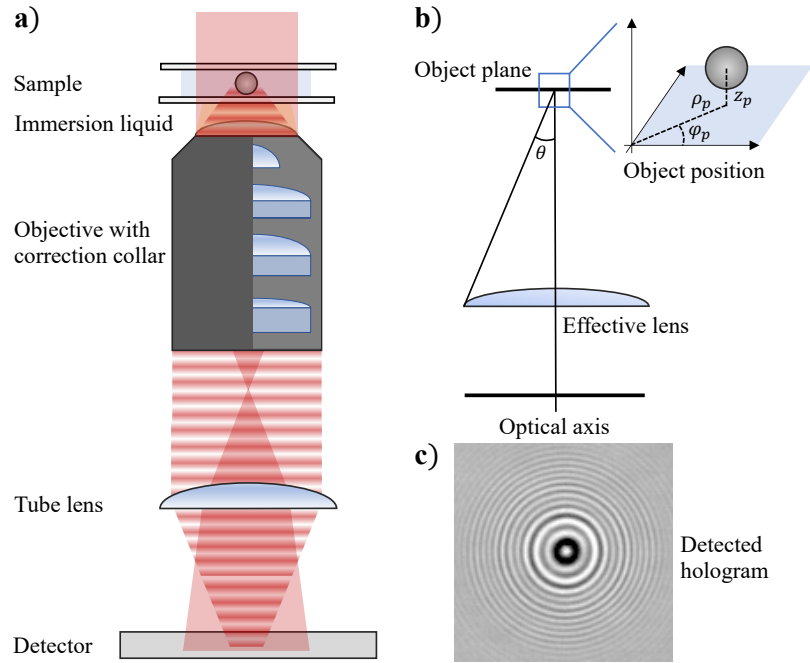


Figure 3.1: (a) Diagram of the optical train in a typical in-line digital holographic microscope with an immersion objective with correction collar. Collimated coherent light (red) illuminates a sample chamber consisting of an object in a medium between a glass slide and coverslip. (b) We treat the optical train as a single effective lens pupil with polar angle θ , as defined from the optical axis. The object's position in the object plane is defined by (ρ_p, ϕ_p, z_p) in cylindrical coordinates. (c) A measured hologram from a $1.05\text{ }\mu\text{m}$ polystyrene sphere sitting $7.5\text{ }\mu\text{m}$ above the focal plane, illuminated with 660 nm light. We record the hologram with a water-immersion lens with a numerical aperture of 1.20 and set the correction collar to minimize aberration.

fit this model directly to aberrated holograms and extract information about the particle as well as the aberrations. This method does not require reconstruction or image processing. We find that modeling the effect of aberrations improves agreement between the model predictions and the experimental data, leading to lower residuals between the best-fit holograms and data across levels of induced aberration. We also find that the inferred parameters do not change as the level of aberration in the optical train increases. Modeling the aberrations therefore allows one to more accurately characterize colloidal spheres even if one does not know whether the experimental setup is spherically aberrated, or by how much. The robustness of the fits with this new forward model to aberrations, either induced in or inherent to the optical system, could simplify experiments and reduce systematic errors.

3.1 EFFECT OF SPHERICAL ABERRATION ON HOLOGRAM STRUCTURE

To explore the effects of typical levels of spherical aberration on hologram structure, We image an immobilized polystyrene microsphere with a reported radius of $1.05\text{ }\mu\text{m}$ (density 1.055 g/mL , index 1.591 at 590 nm , Invitrogen S37500) under varying levels of spherical aberration. To immobilize the microsphere, we fill an inverted sample chamber with a 0.001 \% w/v colloidal suspension in a 0.2 mM NaCl aqueous solution. The particles then sediment and stick to the slide, likely because the salt screens any electrostatic repulsion between the sphere and glass. We then reorient the sample chamber. The particles remain immobilized on the top slide, approximately $150\text{ }\mu\text{m}$ above the interface between the bottom slide and immersion lens.

The particles are illuminated with a diode laser (660 nm wavelength, 120 mW power, Opnext HL6545MG) driven at 130 mA (Thorlabs LDC205C). We use a Nikon Eclipse Ti TE2000 microscope with a water-immersion objective and correction collar (Plan Apo VC $60\times/1.20\text{ WI}$, Nikon, $300\text{ }\mu\text{m}$ working distance) and a 1024×1024 -pixel CMOS monochrome sensor array (PhotonFo-

cus A1024) to capture the hologram. Before analyzing each hologram, we subtract the average of dark-count images taken without illumination and divide the resulting hologram by averaged background images taken with no particles in the field of view. This image processing differs from the double-exposure method of reconstruction-based holography, which removes phase shifts and thus aberrations in the resulting phase-contrast image. We do not attempt to reconstruct the background to obtain a phase map¹⁸⁴. Instead, our processing method removes stray illumination in the optical train and accounts for non-uniform illumination and artifacts.

We adjust the level of induced spherical aberration by varying the correction collar setting on the objective. The correction collar on our objective corrects for coverslip thicknesses of 0.13 mm to 0.19 mm. Setting the collar to the thickness of the coverslip, measured at 0.17 mm, minimizes spherical aberration; setting it to the furthest available setting, 0.13 mm, maximizes spherical aberration. At the maximally aberrated setting, we expect aberration in the phase from 0.04 mm of glass, which is the difference between the measured and corrected thicknesses. This difference should induce a phase shift $\Delta\phi$ between the paraxial and off-axis rays. For a homogeneous material with refractive index n_2 and thickness b embedded in a medium with refractive index n_1 , $\Delta\phi$ is given by

$$\Delta\phi = bk(n_2 - n_1) \left[2 \frac{n_1}{n_2} \sin^2\left(\frac{\theta}{2}\right) + 2(n_2 + n_1) \frac{n_1^2}{n_2^3} \sin^4\left(\frac{\theta}{2}\right) + \dots \right], \quad (3.1)$$

where k is the wavenumber and θ is the angle of incidence of the off-axis ray¹⁹⁰. For a glass layer ($n_2 = 1.515$) with thickness $b = 0.04$ mm surrounded by water ($n_1 = 1.33$), and at the maximum angle of incidence set by the numerical aperture of the lens ($NA = 1.2$), we calculate a maximum phase shift corresponding to approximately 52 wavelengths. In the above expression, the $\sin^2(\theta/2)$ term corresponds to defocus, which accounts for 35 wavelengths of phase shift, and the $\sin^4(\theta/2)$ term corresponds to the primary spherical aberration, which accounts for the remaining 17 wavelengths. The higher order terms correspond to higher order spherical aberration. To minimize the

aberration induced by the coverslip, we correctly set the correction collar to the precisely measured thickness of the coverslip (0.17 mm). In this case, we expect any remaining aberration to be intrinsic to the optical system, rather than induced by the experimental setup. We note that because high-numerical-aperture objectives are designed to image objects in the focal plane, they may not be well corrected for aberrations far from the focus.

To examine how increasing the aberration affects the hologram structure, we record “stacks” of holograms of the immobilized sphere by sweeping the focus through the particle at three different correction-collar settings. We then examine the x - z cross-sections of these hologram stacks, where each section shows the intensity of the hologram through the central fringe (Figure 3.2). The particle height determines the spacing of the fringes in the resulting hologram, with the fringe spacing increasing with increasing distance from the focal plane. The x - z cross-sections therefore have a cone-like structure, with a bright center above the focus and a dark center below. With no spherical aberration, we expect a single focal point at which the center of the hologram transitions from bright to dark, which we observe in the cross-section at 0.17 mm correction.

As we change the correction collar setting, the increase in aberration introduces several noticeable changes in the recorded hologram structure. First, oscillations between bright and dark points appear along the central axis (orange arrows in Figure 3.2), and the number of oscillations increases as we increase the aberration. Second, we observe an overlap of fringes near the focus. Instead of converging at the focal plane, the bottom cone structure converges at a point above the focal plane with increasing aberration, resulting in distortions due to the overlap of the fringes of the top and bottom cone near the focal plane (green arrows in Figure 3.2). Finally, the position of the focal plane shifts as the aberration increases, as highlighted in Figure 3.2 by the increasing distance of the focal planes from the blue dotted line.

These changes in structure are the result of the angle-dependent phase shift due to increasing spherical aberration. Spherical aberration changes the phase of the off-axis rays. The interference

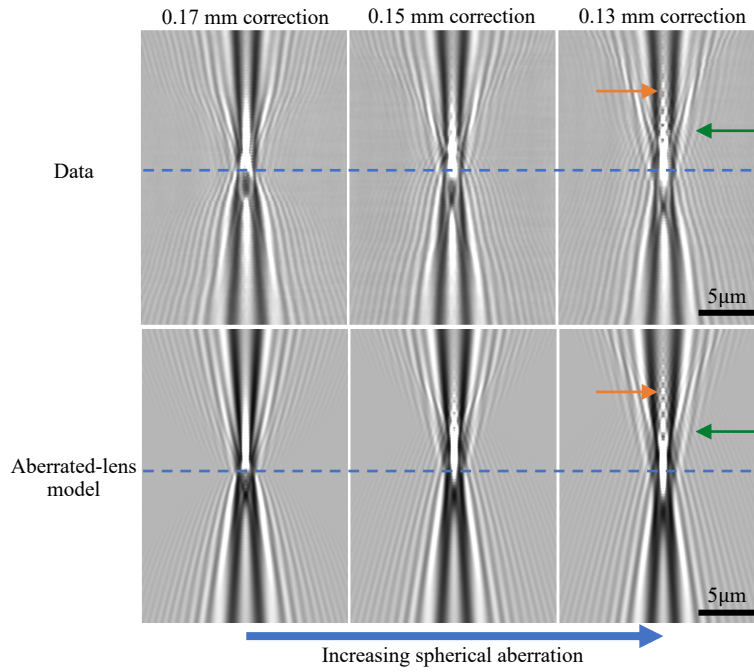


Figure 3.2: x - z cross-sections of stacks of holograms of an immobilized $1.05\text{ }\mu\text{m}$ radius polystyrene microsphere, taken from $15\text{ }\mu\text{m}$ below to $15\text{ }\mu\text{m}$ above the focus in $0.25\text{ }\mu\text{m}$ intervals at three correction collar settings. Adjusting the correction collar induces spherical aberration, which results in on-axis oscillations in brightness (orange arrow), overlapping fringes close to the focal plane (green arrow), and defocus. The blue line marks the focal plane of the least aberrated system; all stacks are taken with the lens in the same physical position. The top row of cross-sections shows experimental data. The bottom row shows calculations from a model that includes spherical aberration. By changing α_0 in the aberration series (primarily fourth order in the phase deviation), we are able to produce cross-sections that capture the distortions in the experimentally observed holograms.

between these peripheral rays and the paraxial rays produces the bright and dark points that we see in the data; the up-down asymmetry is characteristic of spherical aberration ¹⁹¹. The overlap of fringes as the cone structures do not come to a single point is also indicative of spherical aberration, as there is no longer a single well-defined focal plane in the presence of these aberrations. Finally, the observed defocus effect is also characteristic of aberration induced by index mismatch, as described above.

3.2 MODELING THE EFFECT OF SPHERICAL ABERRATION

These results show that spherical aberration caused by small offsets in the correction collar can induce significant changes in the recorded holograms across a wide depth of field. To infer accurate particle parameters under typical levels of spherical aberration, we need a forward model that accounts for these effects.

To model the effects of aberration on a recorded hologram, we build upon the treatment for modeling an unaberrated lens from Leahy, Alexander, and coworkers¹¹⁸. In an unaberrated system, all rays emitted from a point source on the focal plane come to a focus at a single point on the detector. By Fermat's principle, these rays traverse the same optical path length through the imaging system. In an aberrated system, the rays do not come to a focus at a single point, and therefore the phase of each ray differs. These phase aberrations can be quantified by the deviation Φ of each ray's phase from its ideal value, as measured on the lens pupil. In the presence of general aberrations, Φ depends both on the position on the lens pupil and on the source's in-plane position¹⁹¹. For spherical aberration, however, Φ is a function of the polar angle θ only, defined in Figure 3.1b. For incident light polarized along the x -direction $\hat{\mathbf{x}}$ of the detector plane, propagating the fields through the optical train yields the incident (\mathbf{E}_{in}) and scattered fields (\mathbf{E}_{sc}) on the detector:

$$\mathbf{E}_{\text{in}} \propto -E_0 e^{i\Phi(\theta)} \hat{\mathbf{x}} \quad (3.2)$$

$$\begin{aligned} \mathbf{E}_{\text{sc}}(\rho_p, \phi_p, z_p) \propto & \frac{E_0}{2} \left\{ [\mathcal{I}_0(k\rho_p, kz_p) + \mathcal{I}_2(k\rho_p, kz_p) \cos(2\phi_p)] \hat{\mathbf{x}} \right. \\ & \left. + \mathcal{I}_2(k\rho_p, kz_p) \sin(2\phi_p) \hat{\mathbf{y}} \right\}, \end{aligned} \quad (3.3)$$

where (ρ_p, ϕ_p, z_p) is the position of the particle in cylindrical coordinates, as shown in Figure 3.1b, and $\hat{\mathbf{y}}$ is the unit vector along the y direction. We have omitted phase and amplitude factors common to both the incident and scattered fields. In the presence of aberrations, the integrals \mathcal{I}_0 and \mathcal{I}_2

are defined as

$$\mathcal{I}_0(u, v) = \int_0^\beta [S_\perp(\theta) + S_{\parallel}(\theta)] J_0(u \sin \theta) e^{iv(1-\cos \theta)} e^{i\Phi(\theta)} \sqrt{\cos \theta} \sin \theta d\theta \quad (3.4)$$

$$\mathcal{I}_2(u, v) = \int_0^\beta [S_\perp(\theta) - S_{\parallel}(\theta)] J_2(u \sin \theta) e^{iv(1-\cos \theta)} e^{i\Phi(\theta)} \sqrt{\cos \theta} \sin \theta d\theta, \quad (3.5)$$

where J_n is the Bessel function of the first kind of order n , S_\perp and S_{\parallel} are the components of the far-field scattering matrix given by Mie theory, and β is the acceptance angle of the lens.

In the unaberrated-lens model ¹¹⁸, Φ is constant and \mathcal{I}_0 and \mathcal{I}_2 are changed only by a phase factor $e^{i\Phi}$ imparted by the lens. In the presence of spherical aberrations, Φ is a general function of θ^2 , and therefore Φ is generally Taylor-expanded as an even polynomial in θ . The constant term in this polynomial corresponds to piston, which is irrelevant for in-line holographic microscopy because it affects the incident and scattered fields identically and therefore does not alter their interference. The quadratic term corresponds to defocus, which is degenerate with z_p . Thus, we represent $\Phi(\theta)$ as a function $(1 - \cos \theta)^2 [\alpha_0 + \alpha_1 P_1(1 - \cos \theta) + \alpha_2 P_2(1 - \cos \theta)]$, where P_ℓ are Legendre polynomials and the coefficients α_ℓ are parameters that describe the level of aberration. Since $1 - \cos \theta = \theta^2/2 - \theta^4/24 + \dots$, this parameterization excludes piston and defocus aberrations. The coefficients α_0 , α_1 , and α_2 allow us to account for fourth- through eighth-order aberrations in the phase (or third- to seventh-order in the ray displacements). While the coefficient α_0 primarily describes fourth-order spherical aberration, the coefficients α_1 and α_2 describe a mix of fourth-, sixth-, and eighth-order aberrations. We choose to parameterize Φ in terms of Legendre polynomials to make it easier to fit the aberration coefficients to data; a parameterization in terms of ordinary polynomials leads to covariances between the inferred expansion coefficients.

With this model for spherical aberrations, we are able to generate holograms that capture the aberrated structure observed in the data. We generate x - z cross-sections at evenly spaced intervals as z_p moves through the focal plane (Figure 3.2, bottom), using parameters based on the manufac-

turer’s specifications of the microsphere imaged in the top row. When the aberration coefficients are set to zero, we recover the expected unaberrated structure: a double cone that comes to a single focus where the hologram center transitions from bright to dark. When we increase the aberrations by increasing α_0 (corresponding to primarily fourth-order phase aberrations), we reproduce the effects we observe in the aberrated data, including the on-axis oscillations in brightness and the overlapping fringe pattern near the focal plane. Because our parameterization of the aberration function separates defocus from spherical aberrations, we also adjust z_p in the generated holograms to account for the defocus in the data.

The model does not capture all of the structure seen in the cross-sections, particularly in the regions near the focal plane. For example, the model does not accurately reproduce the intensity and structure of the dark region below the focus. These discrepancies suggest the need to model other effects, including perhaps other types of aberrations. Nonetheless, our results show that accounting for spherical aberration captures many of the aberration-dependent distortions in hologram structure that can arise under typical experimental conditions.

3.3 EFFECT OF SPHERICAL ABERRATION ON PARTICLE CHARACTERIZATION

To determine how spherical aberrations affect the accuracy of particle characterization, we fit holograms of a single immobilized 1.05 μm -radius polystyrene sphere at varying coverslip corrections, recorded from 30 μm above to 30 μm below the focus in 0.25 μm intervals. We fit both the aberrated-lens model described above and the unaberrated-lens model¹¹⁸ (hereafter called the “lens model”) to the measured holograms to infer the particle radius, refractive index, and position, as well as the objective acceptance angle β and the field rescaling parameter α . For the aberrated-lens model, we also fit three coefficients of the aberration series, α_0 , α_1 , and α_2 (see Section 3.4 for details on how we choose the order of the series required to describe aberrations in the data). We use a Bayesian frame-

work, and to avoid local minima in the posterior probability density, we use a combination of non-linear least-squares fitting, covariance matrix adaptation evolution strategy, and parallel-tempered affine-invariant Markov-chain Monte Carlo sampling.

We find that the aberrated-lens model produces consistently better fits to the data than the lens model, as measured by the sum of squared residuals χ^2 (Figure 3.3). When the particle is within 5 μm of the focal plane, fitting becomes inconsistent for both models, and the residuals between the data and best-fit holograms are large. When the particle is 30 μm from the focal plane, both models produce fits with comparable residuals. As the microsphere approaches the focus, however, the residuals found by the lens model increase significantly. Furthermore, the lens model fits the data increasingly poorly as the aberration increases. By contrast, the residuals found by fitting the aberrated-lens model do not increase as sharply with decreasing distance between the microsphere and focal plane and do not change as much with the level of aberration. The aberrated-lens model also produces consistently lower residuals than the lens model, with the largest improvement in goodness-of-fit observed for the most aberrated system. When the particle is farther than 5 μm from the focal plane, we find that modeling the effect of aberrations produces more consistent residuals and improves goodness-of-fit at all aberration levels.

Ignoring the effects of spherical aberration in the model results not only in higher residuals but also in systematic shifts in the inferred particle refractive index and radius with the aberration level. When the particle is more than 5 μm from the focal plane, the inferred values for both the refractive index and radius differ consistently between the most aberrated (0.13 mm collar setting) and least aberrated (0.17 mm) systems, even when the particle is at the same z_p (Figure 3.4, top). We quantify this parameter shift by determining the absolute difference between the inferred parameters for each z_p more than 5 μm from the focal plane, then averaging across particle position to find the mean absolute difference with standard error. The inferred refractive indices differ by (0.030 ± 0.002) , or $(1.8 \pm 0.1)\%$, and the inferred radii differ by (0.020 ± 0.002) μm , or

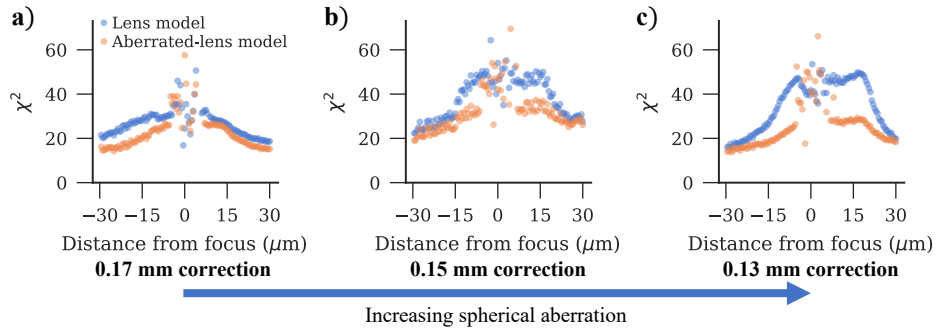


Figure 3.3: (a-c) The sum of squared residuals between holograms of an immobilized microsphere and best-fit holograms found with both the lens model and aberrated-lens model as a function of distance from focal plane and level of spherical aberration. While both models produce high residuals near the focal plane, outside this region, the aberrated-lens model produces consistently lower residuals than the lens model does. This improvement in goodness-of-fit occurs across z_p and aberration level, with the largest improvement seen in the most aberrated system.

(2.0 ± 0.2) %, when the particle is more than 5 μm from the focal plane. This difference is far larger than the uncertainty in parameters, estimated as the standard error for each best-fit value and shown as error bars in Figure 3.4.

When we account for aberration in our model, the inferred parameters no longer depend on the level of aberration (Figure 3.4, bottom). When the sphere is more than 5 μm from the focal plane, the refractive indices inferred using the aberrated-lens model differ by (0.002 ± 0.001), or (0.16 ± 0.03) %, between the most and least aberrated systems, an order-of-magnitude improvement over the refractive indices inferred using the lens model. The inferred radii differ by (0.007 ± 0.002) μm , or (0.8 ± 0.2) %, a two-fold improvement.

Furthermore, the refractive index and radius that we infer by fitting the aberrated-lens model are close to the values reported by the manufacturer of the particles, irrespective of the aberration level. When the microsphere is more than 5 μm from the focal plane, we infer a refractive index of $n = (1.597 \pm 0.014)$ and a radius of $r = (0.951 \pm 0.017)$ μm for the least aberrated system, and $n = (1.599 \pm 0.015)$ and $r = (0.950 \pm 0.027)$ μm for the most aberrated system, where the values reported represent the mean and standard deviation of inferred parameters across z_p values. The

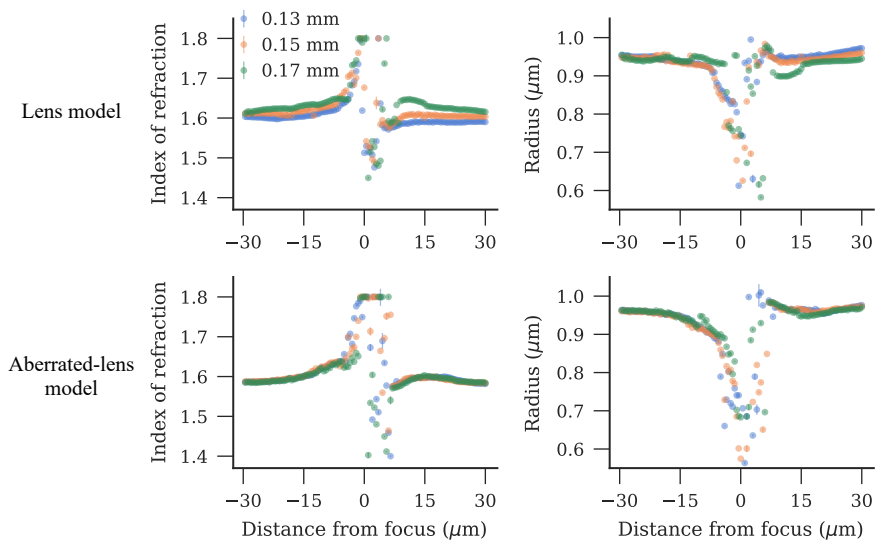


Figure 3.4: Refractive index and radius inferred by fitting the lens model and aberrated-lens models to the data, shown as a function of particle distance from the focal plane. Colors indicate the level of spherical aberration, as measured by the correction-collar setting (lowest level of aberration is at 0.17 mm). Both models perform poorly near the focal plane, yielding unphysical and inconsistent values for the refractive index and radius when the particle is closer than about 5 μm to the focus. Outside this region, the refractive index and radius inferred by fitting the lens model depend on the level of aberration in the system. For the aberrated-lens model, this systematic difference disappears, and we obtain consistent results across aberration levels.

manufacturer reports the value of the radius as $r = (1.050 \pm 0.026) \mu\text{m}$ and the refractive index as $n = 1.591$ at 590 nm; we expect the refractive index of polystyrene to be $n = 1.586$ at 660 nm¹⁹². We find good agreement between the inferred and expected refractive index irrespective of aberration level in the system. Although there is a difference between the manufacturer's mean value and our inferred value of the radius, the inferred values are consistent across aberration levels. The remaining systematic difference might arise from differences in measurement conditions (dry *versus* aqueous), polydispersity in the particle stock, or additional unmodeled optical effects. Nonetheless, the self-consistency of the parameters and the agreement between the inferred and expected refractive index show that modeling spherical aberration removes one source of systematic error in particle characterization.

These characterization results do not change significantly with z_p when the particle is more than 10 μm from the focus. The variation in the inferred radius, as quantified by the standard deviation across z_p values, is 0.9 %, and that in the inferred refractive index is 0.5 %, as compared to 19.7 % (radius) and 6.0 % (refractive index) when the particle is less than 10 μm from the focus. Neither the lens model nor the aberrated-lens model give consistent or even physically realistic estimates when the particle is within 5 μm of the focus, and in the 5 μm to 10 μm range, the inferred values have a noticeable z_p dependence. For example, as the particle approaches the focus from above, the refractive index is systematically underestimated and the radius is systematically overestimated; the reverse occurs as the particle approaches the focus from below. Therefore, the forward-modeling approach that we demonstrate should be used with caution when, for example, one must characterize particles that could drift near the focal plane. Future work should focus on modeling other optical effects that are relevant near the focus. We hypothesize that the poor characterization close to the focus arises because there are few fringes and little contrast, limiting the amount of information that could be extracted by fitting. The dependence of the inferred parameters on z_p that we observe might provide some clues about what other effects must be modeled to improve the precision near the focal

plane.

There is no additional computational cost to calculating a hologram with the aberrated-lens model compared to the lens model. On a 1.6 GHz Intel Core i5 processor, the aberrated-lens model takes (85 ± 3) ms to generate a 200×200 pixel hologram, while the lens model takes (86 ± 5) ms; these numbers include overhead incurred by the `holopy` package¹²⁴. However, it does take longer to fit the aberrated-lens model to data because it has more parameters than the lens model.

3.4 NUMERICAL METHODS

We evaluate Eqs. 3.4–3.5 using the same methods described by Leahy, Alexander, and coworkers¹¹⁸ for an unaberrated lens. Because spherical aberrations preserve the azimuthal symmetry in Eqs. 3.4–3.5, their numerical evaluation carries no additional computational complexity relative to the unaberrated case and retains a computational advantage over the lensless model due to additional numerical optimizations in the lens model¹¹⁸. We use the Python package `holopy`^{124,193} to calculate holograms using the lens model¹¹⁸.

To fit these models, we use a multi-step approach designed to avoid local minima. We first use a parallel-tempered, affine-invariant, Markov-chain Monte Carlo ensemble sampler, as implemented by the Python package `emcee`¹⁹⁴. We choose uniform priors with bounds set by any physical constraints of the experimental system ($x, y > 0, r > 0, n > 0, 0 < \beta < 1.2, \alpha > 0$). We run this parallel-tempering algorithm at 7 temperatures with 50 walkers for 2000 steps each, which takes approximately 12 h per hologram on one core. We therefore use parallel tempering to fit only every 20th hologram in each stack.

We then fit the remaining intermediate holograms using the maximum *a posteriori* parameters found with parallel tempering as the initial guess. We fit these holograms iteratively with the evolution strategy CMA-ES (covariance matrix adaptation evolution strategy)¹²¹, as implemented by

the Python package `cma`¹⁹⁵, and with a Levenberg-Marquardt algorithm for nonlinear least-squares fitting, as implemented by the python package `lmfit`¹⁹⁶. We find that when we fit with CMA-ES alone, we avoid local minima but often fail to fully converge on the minimum within a reasonable computation time. Conversely, we find that when we use only Levenberg-Marquardt least-squares fitting, we converge to a good fit only with a very good initial guess. Thus, we first explore the posterior landscape with CMA-ES, and then ensure that we converge on the best fit through least-squares minimization of the residuals. The combination of the two algorithms with the initial guess from MCMC produces fits comparable to those we find with parallel-tempering, but with much shorter run times. When we maximize the posterior with CMA-ES, we choose broad Gaussian priors, with means set by the maximum *a posteriori* parameters found by parallel tempering and variances set to physically reasonable values, such as the width of a pixel for the particle's x and y coordinates ($\sigma_{x,y} = 0.176 \mu\text{m}$, $\sigma_z = 4 \mu\text{m}$, $\sigma_n = 0.2$, $\sigma_r = 0.1 \mu\text{m}$, $\sigma_\alpha = 0.5$, $\sigma_\beta = 0.4$, $\sigma_{\alpha_\ell} = 300$). The widest priors are chosen for α_0 , α_1 , and α_2 , which have widths of the same order as the typical values we infer for the coefficients. We choose these wide priors because in typical experiments the microscope user has little *a priori* knowledge of the aberration. For other parameters, we place bounds on the Gaussian priors if there are any physical constraints ($x, y > 0$, $r > 0$, $n > 0$, $0 < \beta < 1.2$, $\alpha > 0$). We then use least-squares fitting to minimize the residuals between the data and the best-fit holograms found by CMA-ES. The error bars shown in Figure 3.4 are calculated by `lmfit` from the estimated covariance matrix. Because the holograms are analyzed individually, the uncertainties are independent. They do not account for systematic errors. We find that when the holograms are closely spaced in z_p , the parameters change slowly enough that we avoid local minima in fitting the holograms between the select parallel-tempered frames.

To determine the order of the expansion of the aberration function necessary to describe the data, we calculate the sum of squared residuals χ^2 and the maximum *a posteriori* parameters for increasing aberration order using the parallel-tempered sampler described above. We select holograms

taken at $z_p = 7.5 \mu\text{m}$ above the focal plane, for 0.13 mm to 0.17 mm correction. Holograms at this position are well within the distance from the focus where fitting returns reasonable residuals for all models, but they also show a large change in structure as we change the level of aberrations, indicating a strong dependence on the aberration function. We find that the χ^2 value decays with increasing aberration expansion order, with χ^2 at a maximum with zeroth-order aberration (lens model) and decreasing with each additional aberration order included before plateauing. We observe this decay in χ^2 for all levels of aberration, with the sharpest decay occurring in the most aberrated system. For our data, the χ^2 values plateau when we expand up to the eighth-order phase polynomial, which includes aberration coefficients α_0 , α_1 , and α_2 . We find very small differences between the eighth-order and tenth-order expansion, with an average decrease in χ^2 of 0.6% across levels of aberration. This improvement in goodness-of-fit is much smaller than the 43% mean decrease in χ^2 found between the zeroth- and eighth-order expansion.

We see additional evidence favoring the eighth-order expansion in the comparison of the inferred maximum *a posteriori* parameters to the manufacturer's specifications for the particles. We find that when we include only α_0 in the expansion, the χ^2 value decreases greatly compared to the lens-model, but the maximum *a posteriori* parameters become unphysical, with the maximum *a posteriori* refractive index jumping to nearly 1.68 , much larger than the anticipated value of 1.59 . As we increase the number of aberration coefficients, the maximum *a posteriori* values of the parameters plateau to physical values with the eighth-order expansion with coefficients α_0 , α_1 , and α_2 . We find small differences between characterization with the eighth- and tenth-order expansion, with average differences of 0.5% in refractive index and 0.6% in radius. To avoid unnecessary complexity in the model, we choose to expand the aberration function to the eighth-order phase polynomial and include three aberration parameters in the model.

Although we find that truncating the aberration series at the eighth-order phase polynomial is appropriate for the aberration level in our experimental system, other experimental systems may

require higher-order expansions to fully capture the aberration function.

3.5 CONCLUSION

Unless carefully corrected, spherical aberration is present in typical holographic microscopes and can significantly affect hologram structure. Spherical aberration can arise in an otherwise corrected system when the correction collar on a water-immersion lens is incorrectly set, or when there are interfaces between media of different refractive indices—for example, when an aqueous sample chamber is imaged using an oil-immersion or air-immersion objective. We have shown that neglecting to account for this aberration leads to inconsistent particle characterization when fitting a forward model to the data.

Adding the effects of spherical aberration to a forward model of hologram formation improves the fit of the model to the data and removes aberration-dependent shifts in the recovered parameters. Fitting with this aberrated-lens model makes particle characterization with holography robust to aberration for both isolated spheres or well-separated collections of spheres⁸². With greater computational resources, it could be expanded to the characterization of other particles, such as clusters and spheroids^{117,119}. The robustness to level of aberration is a useful feature for experiments, because it means that no prior knowledge or characterization of the aberrations is needed. Instead, the aberration coefficients can be fit at the same time as other parameters such as the refractive index and radius. Thus, our method can correct not only the known aberrations in the microscope, such as those induced by the coverslip, but also aberrations that are unknown to the experimentalist because they are intrinsic to the instrument or objective.

An interesting direction for future work is to determine whether modeling the effects of aberration enables reliable particle characterization even with a highly aberrated lens. For example, low-cost holography with a ball lens may be possible. For highly aberrated systems, our methodology

could be extended to other types of aberration, including curvature of field or coma.

Data from the experiments shown in this paper are available in Ref. 197. Source code for the forward model and inference calculations is available in Ref. 193.

*Imagination is better
than a sharp instrument. To pay attention, this is our endless
and proper work.*

Mary Oliver, *Yes! No!*

4

High-precision measurements of particle gap distances

The material in this chapter was done in collaboration with Solomon Barkley, Lev Bershadsky, Jessica Sun, and Vinothan Manoharan, and was supported by the Harvard Materials Research Science and Engineering Center (DMR 20-11754) and the Department of Defense through the National Defense Science and Engineering Graduate Fellowship.

BY OBSERVING THE STATISTICS of the motion of two interacting particles, we can infer the underlying interactions between them. In equilibrium, the distribution of distances r between two particles is given by a Boltzmann distribution that depends on the particle pair potential $U(r)$ such that

$$p(r) \propto \exp [-\beta U(r)], \quad (4.1)$$

where $\beta = 1/k_b T$, k_b is the Boltzmann constant, and T is the temperature. Therefore, to probe the underlying pair potential, which has implications for quantifying the energy and entropy in a particular system to understand self-assembly and structure formation, we can measure the distribution of particle positions.

If we are to characterize short-ranged colloidal interactions such as depletion ¹⁹⁸, screened electrostatics ³³, DNA-mediated interactions ²⁵, or van der Waals ¹⁹⁹ forces, we must measure relative particle positions over time. Because these interactions can vary over a distance of nanometers from the surface of a micrometer-scale sphere, we require that those measurements are precise to the nanometer scale. And in order to directly measure the particle interactions, we would like to measure the positions without confining the particles by an external potential.

Particle localization to nanometer-scale precision without confinement can be difficult. The typical approach, video microscopy, allows colloidal particles to be tracked with a simple bright-field microscope with subpixel localization for particles moving in two dimensions ¹²⁵. Although bright-field microscopy is not designed for out-of-focus imaging, axial information can be extracted by quantifying out-of-focus blur, allowing a single particle to be tracked to subnanometer precision ²⁰⁰. However, 3D tracking with bright-field microscopy for more than one particle remains less precise, owing to multiple scattering and near-field coupling between the spheres ²⁰¹. One way to avoid multiple scattering is to index-match the particles and fluid. If the particles are fluorescently labeled, they can then be imaged with confocal microscopy. Extracting quantitative information from

these images requires further analysis; recent methods have achieved particle localization to 3 nm²⁰².

A limitation of confocal microscopy, however, is that it relies on axial scanning to acquire 3D information, limiting the method to large or slowly moving particles. An alternative approach, total internal reflectance microscopy, does not require axial scanning. It makes use of scattering from a weak evanescent wave near a surface to measure nanometer-scale changes in particle heights²⁰³, but can only image particles very close to a surface – around 250 nm or less.

Here, we demonstrate an alternative approach to solving measuring small interparticle distances using holographic microscopy. Because holograms record both phase and intensity, we can recover three-dimensional (3D) information from a single two-dimensional (2D) image, allowing us to track particles in 3D without confinement or scanning. Using this approach, we measure the trajectories of two freely diffusing colloidal spheres. By fitting a model of particle light scattering to this data, we directly infer the surface-to-surface gap distance to nanoscale precision. Because the model accounts for multiple scattering and near-field coupling between the two spheres, we can accurately measure small separation distances.

Previous attempts to measure small gap distances between colloidal spheres with holographic microscopy include the work of Fung and coworkers⁸⁸, which used a model-based approach to quantify the translational, vibrational, and rotational dynamics of colloidal clusters freely moving in 3D. They were able to track interparticle distances by analyzing the data with an exact numerical solution to scattering by two spheres, which they found was necessary due to the near-field coupling of the particle scattering at small separation distances. By fitting for the particle positions in 3D space, they tracked the vibrational dynamics of a colloidal dimer and inferred the particle pair potential.

Though an important proof of concept, this work had several limitations. For one, the inferred particle radii had an uncertainty on the order of 10 nm to 100 nm, the same magnitude as the range of the interaction itself. Because each particle radius and position were inferred separately, there were also strong covariances between the model parameters, which lead to large uncertainties in the

gap distance, and the fitting procedure was not able to explicitly avoid unphysical regimes where the particles overlapped. Another challenge was avoiding local minima in the fitting landscape. Because Fung and coworkers used a gradient-descent-based algorithm, they required an initial guess close to the global minimum for reliable results.

In this chapter, we develop a method that overcomes these limitations and allows measurement of gap distances as small as a few nanometers to nanometer-scale precision. We first parameterize the model such that the gap distance between the spheres is an explicit parameter. We also take a Bayesian approach to fit the model to the data, which allows us to account for any prior information about our system. We set informative priors on the parameters, including constraining gap distances to be positive – explicitly forbidding sphere overlap in a way that was not previously possible – and characterizing, *a priori*, the radii and refractive indices of the particular particles used in each experiment. We also use more sophisticated fitting algorithms, including parallel tempered Markov chain Monte Carlo (PT-MCMC) methods¹²³ and evolutionary strategies like covariance matrix adaptation (CMA-ES)¹²¹, to sample the full posterior probability landscape. With this sampling, we obtain not only the best-fit parameters that describe the data, but also the spread and correlation of those parameters. By marginalizing over, or integrating out, other parameters, we incorporate all uncertainties into the uncertainty of the single parameter of interest: the interparticle gap distance.

4.1 METHODS

We suspend dilute amounts of 1.3 μm sulfate polystyrene spheres from Molecular Probes (Lot S37499, density 1.005 g mL⁻¹) in equal volume deionized water (output from Millipore Elix 3 and Millipore Milli-Q Synthesis) and heavy water (deuterium oxide, Cambridge Isotope Laboratories, $\geq 99.9\%$) to density-match the polystyrene spheres with the solution, thereby mitigating the effects of sedimentation. We then add sodium carboxymethyl cellulose (NaCMC, DS 0.9, $\geq 99.5\%$, Acros

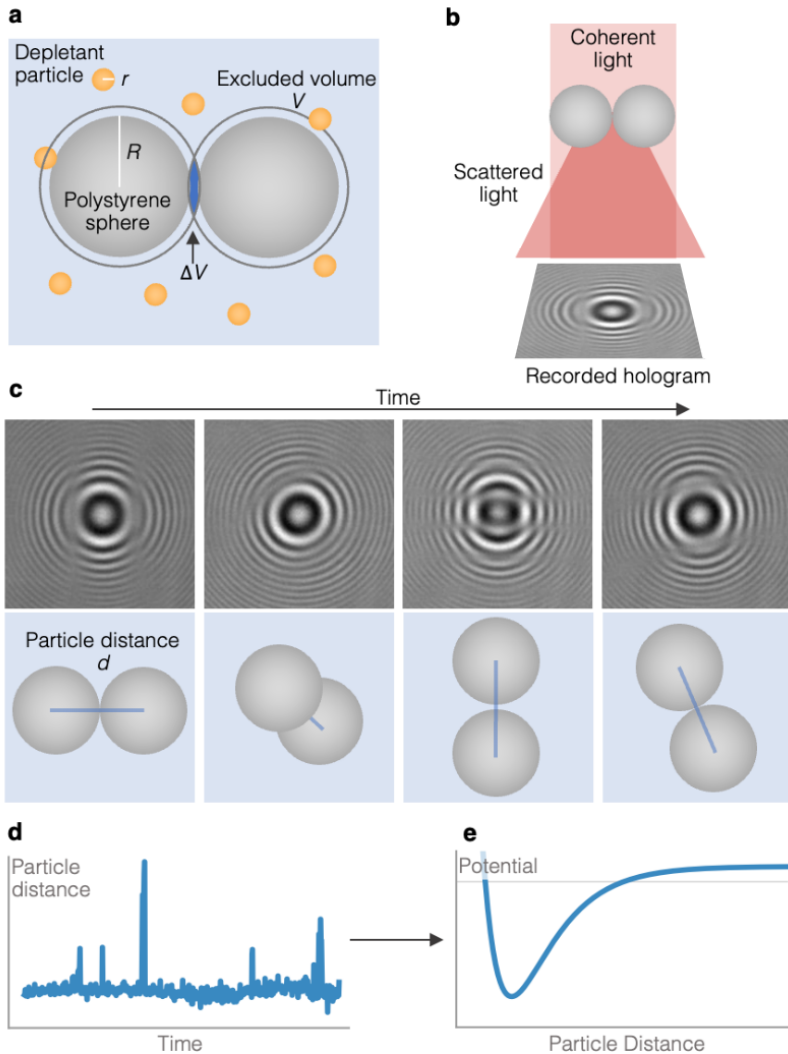


Figure 4.1: Schematic of method to infer particle gap distances with holographic microscopy. (a) Diagram of the depletion interaction. We induce an attractive interaction between polystyrene spheres by adding small depletant polymers to the solution, which drives entropic attraction between spheres with a range set by the size of the depletant particle. (b) Diagram of hologram formation by two spheres. We shine coherent light onto the pair of spheres and record the resulting hologram, the interference between the incident and scattered light. (c) Example of recorded holograms (top) and visualization of particle positions (bottom) given by the best-fit parameters. The recorded hologram encodes 3D information about the particles' positions, sizes, and compositions, which we extract with model-based analysis. (d) Example plot of particle gap distance, as determined by model-based hologram analysis. (e) Example plot of particle pair potential, inferred by analyzing the distribution of gap distances in (d). Data and plots are for illustrative purposes only.

Organics). The polymer has a molecular weight of 700,000, a radius of gyration of about 60 nm, and an overlap concentration of 0.11 mg mL^{-1} ^{204,7}. The polymers induce a depletion attraction between the spheres. We suspend samples at a range of polymer concentration from 0.075 mg mL^{-1} to 0.10 mg mL^{-1} . The NaCMC polymers are nearly index matched with the background, enabling us to image the particles in an optically clear environment.

We create sample chambers of plasma cleaned no. 1 glass coverslips (VWR). We deposit a thick line of vacuum grease (Dow Corning) in a circle on the bottom coverslip, fill the center of the circle with solution, then press the second glass coverslip on top. We seal the chambers with UV-cured epoxy (Norland Optical Adhesives 85). We pipette approximately $2 \mu\text{L}$ of solution into the sample chambers, which are approximately $50 \mu\text{m}$ deep. The samples have a density of approximately 10^{-6} particles per cubic micrometer.

We record images of these suspensions on an inverted in-line holographic microscope, illuminated with a diode laser (660 nm wavelength, 120 mW power, Opnext HL6545MG) driven at 130 mA (Thorlabs LDC205C). We use a Nikon Eclipse Ti TE2000 microscope with a water-immersion objective and correction collar (Plan Apo VC $60\times / 1.20$ WI, Nikon) and a 1024×1024 -pixel CMOS monochrome sensor array (PhotonFocus A1024) to capture the hologram. Before analyzing each hologram, we subtract the average of 25 dark-count images taken without illumination and divide the resulting hologram by the average of 25 background images taken with no particles in the field of view⁴⁴. We manipulate the colloidal spheres with optical tweezers that are created by a fiber-coupled 830 nm laser diode (Sanyo DL-8142-201), with a Thorlabs TCM1000T temperature controller and LD1255 current controller. The beam of the tweezer backfills the objective and is focused at the focal plane.

For each experiment, we use optical tweezers to bring two spheres to the center of the sample chamber, far from any wall or surface, and image the particles with holographic microscopy while they are well separated, at least 10 particle radii apart. We use these images of the spheres to charac-

terize the size and refractive index of each sphere, as we discuss below. We then bring both spheres into the optical trap, which brings the spheres close together and orients the doublet to be roughly parallel to the focal plane. We then turn off the optical tweezers and observe the particles as they freely diffuse in the center of the sample chamber. We record 30 s videos of 4000 frames at 133 frames per second.

We also characterize particle gap distances for particle pairs diffusing on a glass surface, which we discuss in Section 5.4. For these experiments, we suspend dilute amounts of 0.71 μm polystyrene beads (Fluoromax, ThermoFisher) in equal volume deionized water and heavy water with 2 mM NaCl to screen interactions between the particles and glass surfaces. We then add sodium carboxymethyl cellulose (DS 0.9, $\geq 99.5\%$, Acros Organics) with molecular weight of 250,000, and a radius of gyration of about 40 nm, and an overlap concentration of 1.01 mg mL^{-1} ²⁰⁵. We suspend samples at a range of concentrations from 0.17 mg mL^{-1} to 0.40 mg mL^{-1} . For this system, we use the same style of sample chambers and same particle density as the 3D system, but move the particles to the top coverslip of the sample chamber using the radiation pressure of the optical tweezers. The depletion interaction binds the particles to the glass surface, where they are free to diffuse but remain confined to a quasi-2D volume. We record shorter videos of approximately 10 s at 133 frames per second because the bond lifetime is short and the particles quickly diffuse away from each other.

4.2 BAYESIAN ANALYSIS OF HOLOGRAMS

We take a model-based approach to the analysis of the recorded holograms, as described in detail in Chapter 2. In brief, we fit a model for hologram formation to the recorded hologram. The forward model is a solution to Maxwell's equations that depends on the properties of the particles, including their positions, sizes, and refractive indices. By Monte Carlo exploration of the parameter space of

the model, we recover the full posterior probability density, which allows us to estimate the best-fit parameters and any uncertainties or covariances among them.

4.2.1 BAYESIAN INFERENCE

The light scattering solution provides a forward model of hologram formation given a particular set of parameters. But we are really interested in estimating how well a given parameter set describes the data that we observe. To obtain these estimations, we take a Bayesian approach.

Bayesian inference allows us to weigh our data given the model, or our *likelihood*, by our previous expectations, or our *prior*, to arrive at some estimation of our *posterior*. It rests on Bayes's theorem, which states

$$P(\theta | D, M, I) = \frac{P(D | \theta, M, I)P(\theta | M)}{P(D | I)}, \quad (4.2)$$

where θ is the vector of parameters of the model M , D is the observed data, and I is any additional information.²⁰⁶

Bayes's theorem states that the probability density of a hypothesis being true given the available data is equal to the probability density of the data being true given the hypothesis, multiplied by the probability density of the hypothesis being true, and divided by a normalizing value of the probability density of the data being true. The probability density $P(\theta | D, M, I)$ is known as the posterior, the probability density $P(D | \theta, M, I)$ is known as the likelihood, and the probability density $P(\theta | M)$ is known as the prior. Finally, the value of $P(D | I)$ is known as the evidence, which is the probability density of observing the data under any circumstances. This term normalizes the posterior.

A Bayesian approach to data analysis has several appealing features. For one, it frames probability as something we can update, a degree of belief that can change as more data becomes available. Perhaps more appealing is the explicit inclusion of prior information in weighting our degree of belief.

This prior knowledge can exist in several forms – the constraint that a height above a surface must be positive, a guess for the refractive index of a material, or manufacturer specifications for particle size and polydispersity, to name a few. When not explicitly included as prior probabilities, this information typically informs metaparameters such as initial guesses or bounds on parameters. We argue that it is in fact more rigorous to formalize the role of prior information in inference problems, rather than subtly include it behind the scenes in fitting metaparameters.

Another appealing feature of Bayesian inference is the ability to *marginalize*, or integrate out the effects of all parameters not of interest. For example, if we were fitting both the refractive index n and radius r of some sphere, but we were only interested in the radius, the desired probability density function could be written as $P(r) = \int P(r, n) dn$. The marginalized posterior $P(r)$ would then include any uncertainty on n if the parameters have any correlation between them, allowing us to more accurately quantify the uncertainty with which we are actually concerned. More generally, the marginalized posterior is given by

$$P(A | D) = \int P(A, \theta | D) d\theta, \quad (4.3)$$

where A is a general parameter, θ is all other parameters in the model, and $P(A, \theta | D)$ is the multivariate posterior probability density. This formulation allows us to collapse a multidimensional posterior probability density to a univariate posterior for a single parameter of interest.

4.2.2 SAMPLING METHODS

In general, the posterior is a high-dimensional surface, with dimensions that scale with the number of parameters in the model. This high dimensionality presents a difficult problem: how can we find the global maximum of a multidimensional landscape, and how can we evaluate the posterior about that maximum in a reasonable amount of time?

One class of methods to sample posteriors is called Markov chain Monte Carlo (MCMC) algorithms^{207,208,209}. In general, Monte Carlo approaches rely on sampling many points of a posterior, and using that sampled set to construct a representation of the underlying posterior. For MCMC algorithms, this sampling involves a biased random walk: the algorithm samples a point, evaluates the posterior at that point, and probabilistically decides to accept or reject the point as weighted by its probability. The accepted steps are recorded and form a Markov chain. Ultimately, because of this weighting, the “walkers” spend more time in the region of parameter space where the posterior is largest, and after many steps, the algorithm’s walk makes a representative sample of the distribution about its maximum*.

Bayesian inference has experienced explosive growth as sampling methods have become more sophisticated and more computationally tractable. Hamiltonian Monte Carlo (HMC) approaches have allowed for efficient sampling in highly multidimensional posteriors¹²², and parallel tempered MCMC (PT-MCMC) methods have enabled efficient sampling even in highly multimodal posteriors¹²³. We use several of these algorithms, as well as other fitting methods such as CMA-ES, throughout the work in this chapter, which we discuss in detail below.

4.3 PRIOR CHARACTERIZATION OF SPHERES

The inferred gap distance between two spheres is highly sensitive to the radii of the particles. Thus, it is helpful to characterize each pair of spheres used in the experiment before we measure the gap distance. To characterize the particles, we take advantage of the robustness of fitting holograms with the single-sphere model (as discussed in detail in Chapter 2). Because we use optical tweezers to

*A historic note: scientists often call this class of methods “Metropolis-Hastings” algorithms after the two (male) first authors of the formative works on the subject. But it is perhaps more fair that we refer to them as *Rosenbluth-Hastings* algorithms, as the algorithm was in fact implemented for the first time by Dr. Arianna Wright Rosenbluth. For more information about Dr. Rosenbluth’s incredible life and career in science, see <https://www.wowstem.org/post/arianna-wright-rosenbluth>.

bring the colloidal particles together, we can characterize the same spheres that we later image. We incorporate that characterization as a prior on the inferred radii and refractive indices of the spheres in the two-sphere light scattering model.

To characterize the spheres, we record 20 images of the well-separated spheres, meaning that they are separated by a distance of many particle diameters, such that the fringes of the holograms do not interfere. As results from Leahy and coworkers¹¹⁸ and the results described in Chapter 3⁸¹ have shown, the height z of the particles has a large impact on the consistency of the inferred parameters. We record the well-separated holograms at a height that is many particle diameters from the focal plane ($z \approx 20 \mu\text{m}$ for $1.3 \mu\text{m}$ spheres, and $z \approx 15 \mu\text{m}$ for $0.7 \mu\text{m}$ spheres), and maintain that same height as we bring the spheres together and record as they freely diffuse.

The generative model we use can also strongly affect the inferred parameters for the radius and refractive index, as discussed in Chapter 3. To obtain the most precise characterization possible, we fit the well-separated spheres to a single-sphere model that includes optical effects from the lens¹¹⁸. We do not use the model that accounts for optical aberrations, as the results in Chapter 3 show that it is not necessary to account for spherical aberration when the correction collar on the coverslip is properly set to the thickness of the coverslip.

As Leahy and coworkers noted¹¹⁸, the resulting posterior is highly multimodal when the lens angle is included as a parameter. This multimodal posterior presents issues with sampling and finding a global maximum. For typical MCMC algorithms, such as the affine-invariant MCMC sampler implemented by the Python package emcee¹⁹⁴ used to sample the multimodal posterior shown in Fig. 4.2, the walkers do not find the true global maximum and become stuck, leading to inaccurate results. To overcome this problem, we use a parallel-tempered, affine-invariant MCMC sampler implemented by emcee, using 7 temperatures with 50 walkers for 2000 steps each. This sampling takes approximately 10 h for each hologram, but it converges onto a global maximum. The best-fit hologram matches the recorded data (Fig. 4.2a) and the walkers sample the multimodal wells of the lens

angle (Fig. 4.2b).

The samples from the PT-MCMC sampler can be used to estimate the maximum *a posteriori* (MAP) values for each parameter, as well as their uncertainties and covariances. Pair plots of the posterior for a single frame are shown in Figure 4.2b. The marginalized probability densities for each parameter are shown on the diagonal and are approximately Gaussian for all except for the lens angle, owing to its strongly multimodal probability density. The marginalized values for the parameters match our expectations, with the inferred maximum *a posteriori* values for the particle radius ($r = 0.664 \mu\text{m}$) and refractive index ($n = 1.6$) matching manufacturer specifications for the roughly $1.3 \mu\text{m}$ diameter polystyrene spheres.

We use the posteriors from all frames to estimate the average diameter, average refractive index, and uncertainties to be used in subsequent analyses. The mean diameter (or refractive index) across frames is given by²¹⁰

$$\overline{d_w} = \sum_i \frac{w_i d_i}{\sum_i w_i}, \quad (4.4)$$

where w_i is given by

$$w_i = 1/\sigma_i^2. \quad (4.5)$$

For our data, d_i is the MAP value of each frame's posterior and σ_i is the width of the marginalized distribution.

This formulation allows us to describe the mean of the measurements of the radius and refractive index as Gaussians with mean $\overline{d_w}$ and width σ_w . We use these means and widths as prior probabilities on each parameter r_1, r_2, n_1, n_2 for the two-sphere model. We place priors on these parameters rather than setting them as time-invariant constants in the subsequent fitting because we find that allowing slight variations in each as the particles move in 3D space allows for better fits to the holograms.

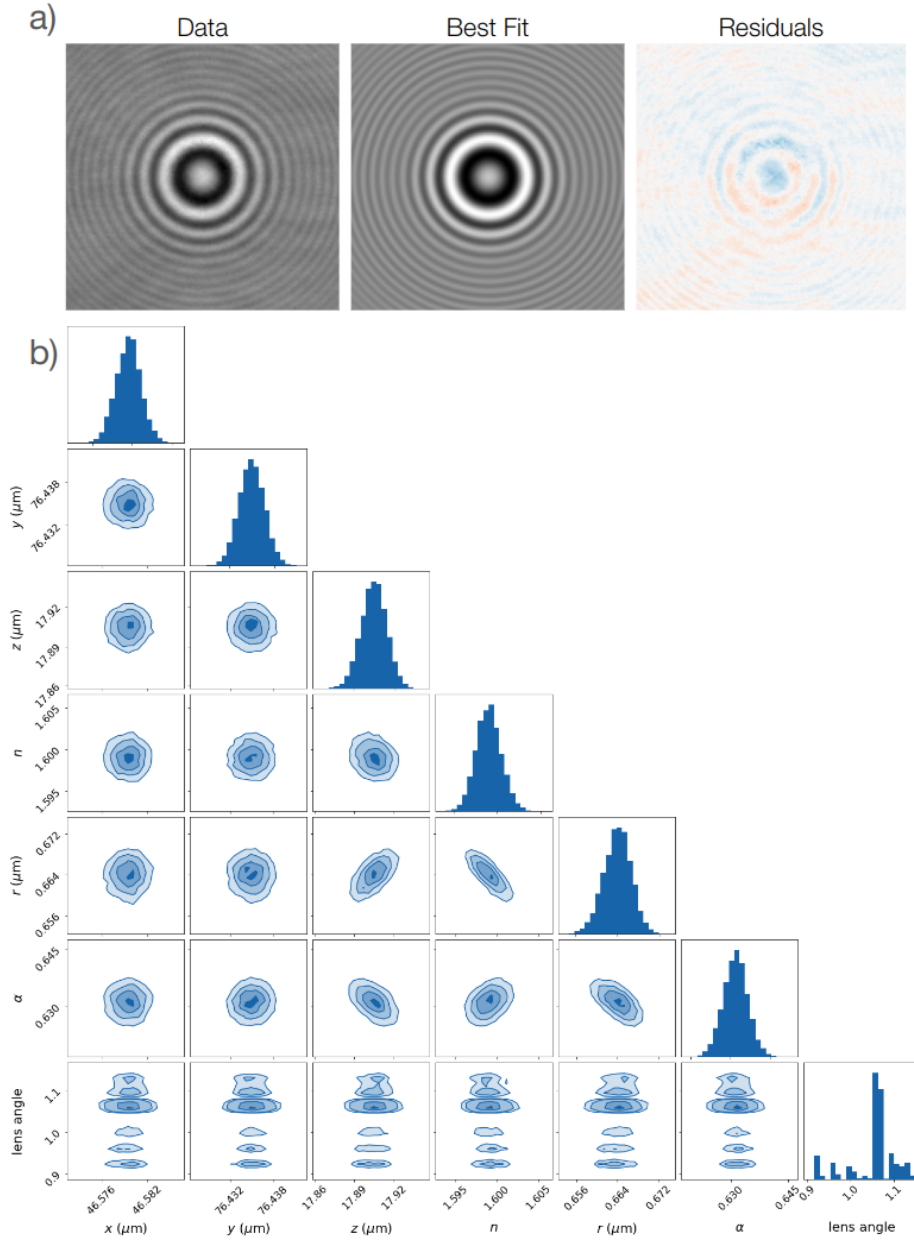


Figure 4.2: (a) With parallel tempering, the maximum *a posteriori* fit (middle) matches the recorded hologram (left) of a $1.3 \mu\text{m}$ sulfate polystyrene sphere and has low residuals (right). (b) Sampled posterior probability densities for all parameters in the lens model for a single particle and frame. The marginalized probability densities for each parameter are shown on the diagonal. They are approximately Gaussian for all except for the lens angle. The off-diagonal plots show the two-dimensional posterior surfaces for each combination of parameters, with skew in these surfaces arising from correlations between the parameters. The inferred maximum *a posteriori* values match manufacturer specifications for the particle radius ($r = 0.664 \mu\text{m}$) and refractive index ($n = 1.6$).

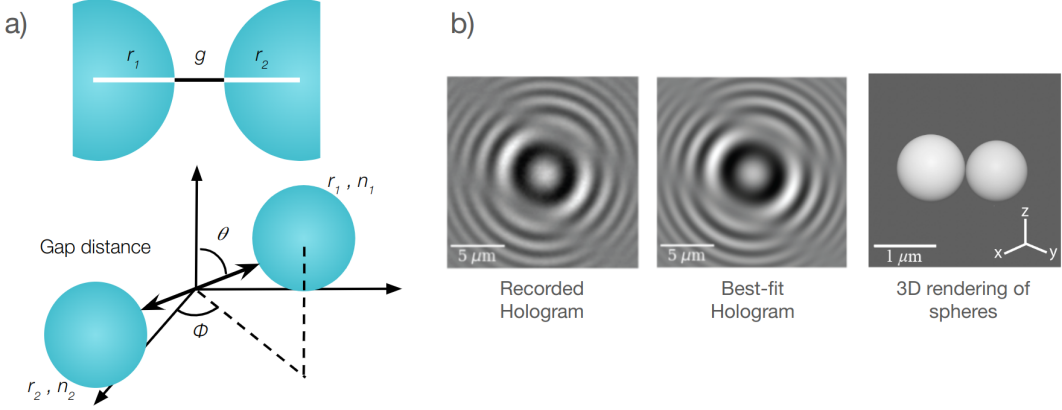


Figure 4.3: Fitting holograms of particle dimers. (a) Coordinate system used for fitting location of the two spheres, allowing gap distance to be an explicit model parameter. (b) Data, best fit hologram, and 3D rendering for a single frame of the two spheres. The best-fit hologram found with the model describes the data well.

4.4 MODEL PARAMETERIZATION

In addition to placing priors on the size and refractive index of each sphere, we also reparameterize the scattering model for the particle pairs so that the gap distance between the spheres is an explicit fitting parameter. Instead of fitting for each particle's position (x_i, y_i, z_i) , we fit to the center of the dimer (x_g, y_g, z_g) and then the spherical coordinates (g, θ, ϕ) that describe the rotation of the line through the center of the dimer, where g is the gap distance between the spheres (Fig. 4.3a). The relation between the center of the dimer and the centers of each sphere i is

$$\begin{bmatrix} x_i \\ y_i \\ z_i \end{bmatrix} = \begin{bmatrix} x_g \\ y_g \\ z_g \end{bmatrix} \pm (r_i + g/2) \begin{bmatrix} \cos \phi \sin \theta \\ \sin \phi \sin \theta \\ \cos \theta \end{bmatrix}. \quad (4.6)$$

The other parameters in the model include the refractive indices of each sphere n_1, n_2 , the radii of each sphere r_1, r_2 , and the scaling parameter α which adjusts the relative intensity of the incident and scattered fields.

To calculate the scattering of the two spheres, we use a lensless model of scattering by two spheres as implemented by `holopy`^{193,124}. The package computes the numerically exact solution of the scattered fields by a superposition solution that accounts for the multiple scattering between the two spheres¹¹⁷. Although it is possible to include the effects of the lens in this model¹¹⁹, Alexander and coworkers found that this approach was computationally prohibitive owing to the need to numerically (rather than analytically) integrate. Because we cannot account for the effects of the lens, we take care to record holograms in a regime well-suited to the lensless model by taking data well above the focal plane with an optical train that is aberration-corrected.

We find good agreement between the best fits of this model to the data and the recorded holograms (Fig. 4.3b). This parameterization allows us to directly characterize the gap distance and, importantly, marginalize over all other parameters in the model, incorporating their uncertainties directly into the uncertainty on gap distance.

4.5 MODEL FITTING

Now that we have a model for hologram formation, all that remains is to fit that model to the recorded data. Ideally, we would run a full MCMC fit on each frame. But for a single 30 s video, this sampling would require nearly a full year of computation time. However, this level of fitting is unnecessary. Because the videos are recorded at a high frame rate relative to the particle rearrangements, the information between subsequent frames is highly correlated. Thus, as a compromise between precision and efficiency, we carefully fit every 100th frame of each video using an iterative combination of CMA-ES, least squares, and MCMC fitting that we describe below. Once we have a good fit for these frames, we run sequential least-squares fitting with a Levenburg-Marquadt algorithm, using the result from each frame as the initial guess for the next frame. Because the frames are closely spaced in time, this sequential fitting can initialize the fitting algorithm very close to the global maxi-

mum of the posterior.

The first step of the fitting scheme for every 100th frame is to estimate the 3D orientation of the spheres by assuming that they are touching and allowing the model to optimize z_g , θ , and φ , as well as the rescaling parameter α , while keeping all other parameters fixed at our best guesses for r_i , n_i , x_g , and y_g (the last two of which we estimate by a Hough transform of the holograms^{83,96,97}). We fit with the evolutionary strategy CMA-ES with 100 walkers, as implemented by the Python package cma¹⁹⁵. We place informative priors on the parameters, such as bounding z_g to be larger than 0 and smaller than the approximate size of the sample chamber of 50 μm , with a mean at the recorded height of the dimer found by translating the microscope stage. We set uniform priors on θ and φ bounded by the physical limits of the angles, with slight extension past these limits to keep the walkers from encountering a hard cutoff near the extremes. The full priors chosen are

$$\begin{aligned} z_g &\sim \text{Truncated Normal}(\mu = z_{\text{rec}}, \sigma = 1, \text{lower} = 0, \text{upper} = 50) \\ \theta &\sim \text{Uniform}(\text{lower} = 0 - 0.1, \text{upper} = \pi + 0.1) \\ \varphi &\sim \text{Uniform}(\text{lower} = 0 - 0.1, \text{upper} = 2\pi + 0.1) \\ \alpha &\sim \text{Uniform}(\text{lower} = 0.5, \text{upper} = 1.2). \end{aligned} \tag{4.7}$$

The second step of the fitting algorithm verifies that CMA-ES has maintained the correct labels for each sphere by calculating the model for flipped labels and coordinates, and accepting the model that has the higher log(posterior) function. Flipping happens rarely, but we must account for it to find the correct orientation for the dimer.

The third step of the fitting process is to find a reasonable guess for the interparticle gap distance. To do this, we allow the gap distance g , the dimer height z_g , and the scaling parameter α to vary, while setting θ and φ to the values found by the previous fitting step, and fixing all other parameters to the previous values of r_i , n_i , x_g , and y_g . We allow z_g to vary to allow for any potential covariances

between the height and the gap distance.

Now that we have a reasonable estimate for each parameter through prior characterization, we use these fits as initial guesses for a Levenberg-Marquardt algorithm for nonlinear least-squares fitting, as implemented by the Python package `lmfit`¹⁹⁶. The final step before fitting with the full MCMC sampler is checking the edge cases on the angle parameters to see if they have gone above or below the bounds set by geometry, and cycling them by 2π if they have crossed the threshold.

Finally, we allow all parameters of the model to vary and sample the model with an affine-invariant Markov chain Monte Carlo sampler as implemented by `emcee`¹⁹⁴. We use 50 walkers that each make 2000 samples, and we randomly subsample the holograms to approximately 30% of the pixels to reduce computational time⁹⁹. The priors used are

$$\begin{aligned}
 r_i &\sim \text{Truncated Normal}(\mu_{r_i}, \sigma_{r_i}, \text{lower} = 0, \text{upper} = 1) \\
 n_i &\sim \text{Truncated Normal}(\mu_{n_i}, \sigma_{n_i}, \text{lower} = 0, \text{upper} = 2) \\
 x_g, y_g &\sim \text{Truncated Normal}(\mu_{x,y}, 0.177, \text{lower} = \mu_{x,y} - 5, \text{upper} = \mu_{x,y} + 5) \\
 z_g &\sim \text{Truncated Normal}(\mu_z, 1, \text{lower} = 0, \text{upper} = 50) \\
 g &\sim \text{Truncated Normal}(\mu_{\text{gap}}, 0.005, \text{lower} = 0, \text{upper} = 10) \\
 \theta &\sim \text{Truncated Normal}(\mu_\theta, 0.1, \text{lower} = 0 - 0.1, \text{upper} = \pi + 0.1) \\
 \varphi &\sim \text{Truncated Normal}(\mu_\varphi, 0.1, \text{lower} = 0 - 0.1, \text{upper} = 2\pi + 0.1) \\
 \alpha &\sim \text{Truncated Normal}(\mu_\alpha, 0.5, \text{lower} = 0, 5, \text{upper} = 1.2),
 \end{aligned} \tag{4.8}$$

where the means of $x_g, y_g, z_g, \theta, \varphi, \alpha$, and g are the final optimized result from the previous fits, and the mean of the priors of each r and n are found using Equations 4.4 and 4.5 such that $\mu = \overline{d_w}$ and $\sigma = \sigma_w$.

The MCMC sampler runs in approximately 3 hours. The final step in the fitting process for a given time series is to use the MAP values returned by the sampler as an initial guess for sequential

frames that have not yet been fit. We use a Levenberg-Marquardt algorithm for nonlinear least-squares fitting, which is much faster than sampling, taking on the order of 1 min for each frame. Because the frame interval is much shorter than the diffusion time of the spheres, the results for the previous frame robustly return a good fit for each sequential frame.

4.6 RESULTS

The MCMC sampler gives us more than simply the best-fit parameters; it allows us to marginalize the full posterior and calculate any covariances among parameters (Fig. 4.4). The results are within reasonable agreement of our prior characterization and manufacturer expectation for the particle radius and refractive index, and are reasonable for all other parameters.

Importantly, we find a high precision for the gap distance between the particles. The uncertainty on the gap distance is a few nanometers, as seen in Fig. 4.5, and the uncertainty on the particle size is less than 1 nm. This precision is two orders of magnitude better than previous measurements of gap distance with holographic microscopy⁸⁸.

With the robust fitting method described above, we precisely measure the gap distance between two particles as a function of time (Fig. 4.6) for the 3D experimental system of 1.3 μm spheres with 0.075 mg mL⁻¹ of NaCMC (radius of gyration approximately 60 nm). The distribution of gap distances can be used to infer the minimum energy point for the potential. We discuss this process, and how these results vary with depletant size, particle size, depletant concentration, and ionic strength in the subsequent chapter.

4.7 CONCLUSION

A model-based inference approach combined with holographic microscopy is well-suited for imaging small numbers of spheres freely diffusing in three dimensions. The model-based approach

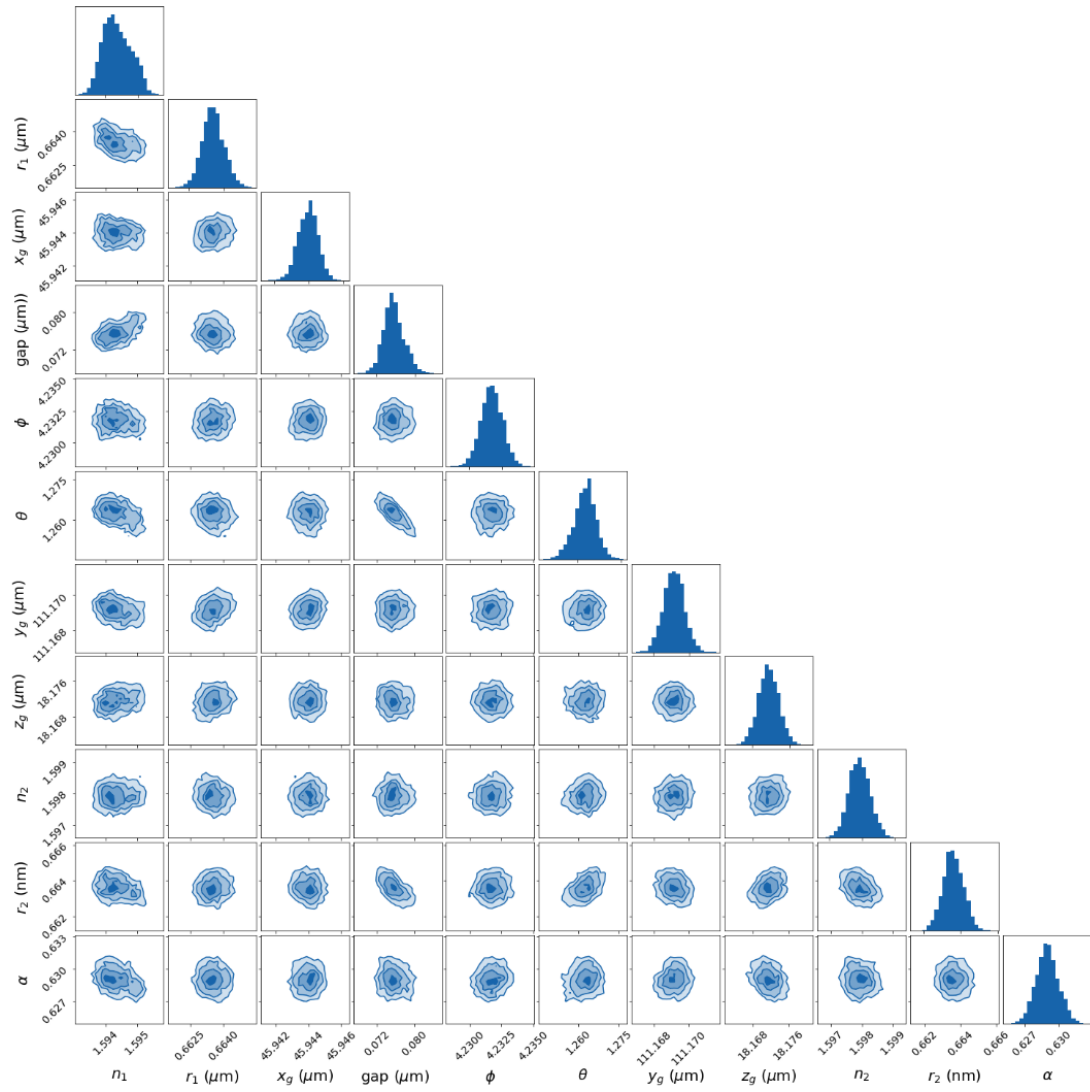


Figure 4.4: Sampled posterior probability density for a single hologram of two interacting spheres. The plots along the diagonal show the marginalized probability for each parameter, while the off-diagonal plots show the two-dimensional marginalized posterior for each pair of parameters.

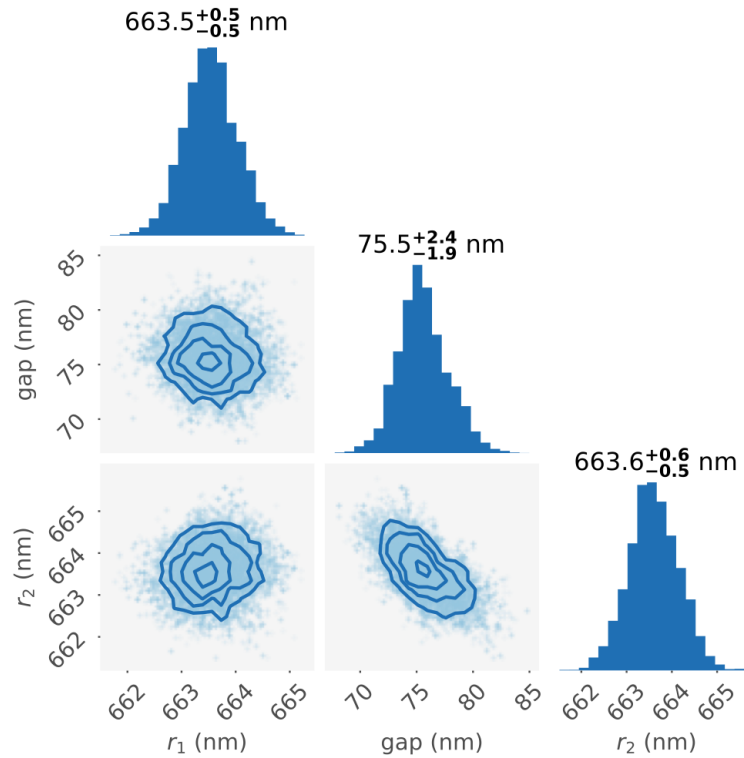


Figure 4.5: Zoomed-in version of Figure 4.4 for the gap distance and particle size. The marginalized probability for each parameter gives a measurement for the best fit as well as uncertainties on the parameters, which we find to be on the order of nanometers.

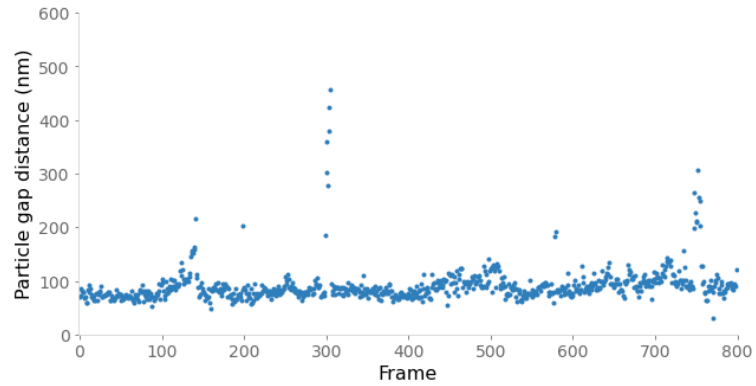


Figure 4.6: Inferred gap distances for frames across a single 30-second video of a pair of freely diffusing $1.3\text{ }\mu\text{m}$ spheres with a depletant concentration of 0.075 mg mL^{-1} . Error bars are shown but are smaller than the point size.

rigorously accounts for any scattering between the spheres, while the microscope encodes three-dimensional information about the sample in a single two-dimensional image, removing the need for axial scanning or particle confinement. Moreover, model-based analysis of holograms works particularly well for small numbers of particles, when the number of parameters are relatively low and computational costs are not too high.

While the first attempt to solve this problem of inferring interparticle distances with holography happened over a decade ago⁸⁸, real success would have to wait for improvements, not in data acquisition, but in data analysis. With Bayesian inference, we now have tools to better constrain this problem through prior characterization of the spheres and a model directly parameterized in terms of the gap distance, and tools to better sample the posterior landscape.

We have shown that the precision achieved through the combination of model-based inference and experimental protocols is of the order of nanometers, orders of magnitude better than the precision of 10 nm to 100 nm previously reported⁸⁸. Furthermore, this precision is also of the order or better than results from tracking particles in bright-field or confocal microscopy, with the advantage that holographic microscopy does not require any confinement or scanning.

With a precise characterization of particle gap distance over time, we now turn to the problem of interpretation in the following chapter. The gap distance encodes information about the underlying particle interactions. We have solved the problem of extracting information from our recorded holograms; what now remains is to understand what we have found.

If we had a keen vision and feeling of all ordinary human life, it would be like hearing the grass grow and the squirrel's heart beat, and we should die of that roar which lies on the other side of silence.

George Eliot, *Middlemarch*

5

Inferring short-ranged colloidal interactions

The research in this chapter was done in collaboration with Solomon Barkley, Lev Bershadsky, Jessica Sun, and Vinothan Manoharan, and was supported by the Harvard Materials Research Science and Engineering Center (DMR 20-11754) and the Department of Defense through the National Defense Science and Engineering Graduate Fellowship.

MANY PHENOMENA IN SOFT MATTER physics depend sensitively on the particular structure of

the interparticle pair potential, but it can be challenging, if not in some cases impossible, to accurately predict this potential *a priori*. Models for the behavior of colloidal spheres in aqueous solutions, such as DLVO (Derjaguin and Landau, Verwey and Overbeek) theory for van der Waals and electrostatic forces, depend sensitively on the solvent conditions and particle charge, which can be difficult to characterize²¹¹. Moreover, some measurements of bulk colloidal behavior deviate from predictions, such as those for charged colloidal suspensions²¹² or suspensions with high depletant concentrations¹⁹⁸. In general, models for interactions often make simplifying assumptions for interactions that may not always hold, such as neglecting geometrical confinement or surface effects from a functionalized coverslip²¹³.

Because *a priori* prediction of colloidal interactions is challenging, it is desirable to instead directly measure particle interactions in order to make accurate predictions for colloidal assembly and behavior. Some current experimental methods for measuring interaction potentials rely on observing confined particles that may be stuck to the wall of a flow cell as in hydrodynamic force balance²¹⁴ or the tip of a force sensor as in atomic force microscopy²¹⁵. Other methods require the particle motion to be constrained to a limited number of dimensions, such as the characterization done by Crocker and coworkers to measure short-ranged interactions of a pair of particles confined to move in one dimension within a optical line trap¹⁹⁸. These methods also require complex experimental setups and might involve conditions that differ from *in situ* environments of the systems of interest.

Regardless of the level of confinement in the experiment, typical methods for inferring particle potentials from measurements may have systematic errors. Consider the method outlined by Crocker and coworkers¹⁹⁸, which has been used to characterize several types of interactions, including interactions between red blood cells²¹⁶, DNA-mediated colloidal interactions²⁵, and three-body interactions²¹⁷. In all these experiments, the particles are confined by optical traps. That optical potential must be known and subtracted off to resolve the underlying potential. Moreover, when parti-

cles are assumed to move within one dimension, any out-of-plane oscillations within the optical trap are neglected. The optical trap used for confinement might also change the pair potential through heating or light scattering effects such as optical binding forces, which can be significant²¹⁸.

Some groups have attempted to address these differences from experimental conditions by instead measuring the potential of mean force of many interacting particles and extrapolating to the dilute limit²¹⁹. But these methodologies are subject to the limited precision of particle tracking algorithms. As discussed in the previous chapter, tracking freely moving particles in 3D space is a challenging problem because colloidal spheres at close distances can scatter light multiple times and optical artifacts arise in microscope images. There have been attempts to overcome this limited precision through reconstruction of bright-field images²¹⁸, back focal plane interferometry²¹³, total internal reflection microscopy¹⁹⁹, or confocal microscopy,²²⁰ but these methods require either confinement or axial scanning, which limits the time resolution.

As demonstrated in the previous chapter, we can use holographic microscopy to account for or avoid many of these issues. With a model-based analysis of holograms, we can extract gap distances between freely diffusing pairs of colloidal spheres to nanometer-scale precision. Now, we turn to the problem of extracting information from the distribution of those distances. In this chapter, we describe methods for inferring particle interactions with model-free and model-based methods, as well as precise quantification of the curvature of the potential about the minimum.

5.1 BOLTZMANN INVERSION

The distribution of center-to-center distances r between two particles in equilibrium is given by a Boltzmann distribution depending on the pair potential $U(r)$:

$$p_b(r) \propto \exp [-\beta U(r)], \quad (5.1)$$

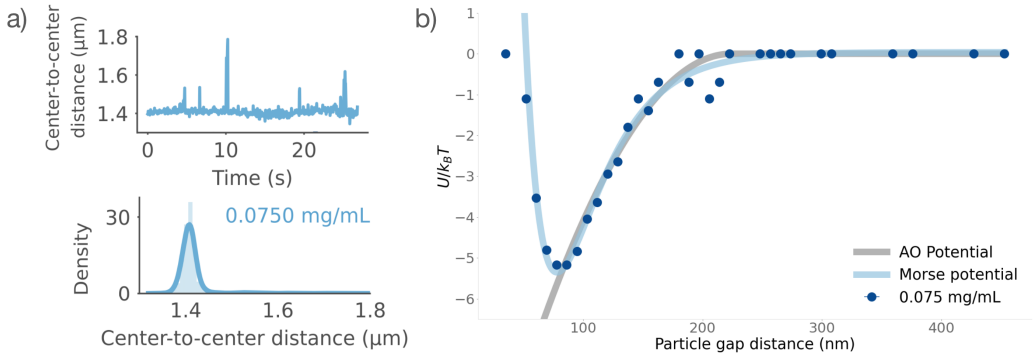


Figure 5.1: (a) Plots of particle center-to-center distance over time and histogram of center-to-center distances. The spheres are 1.3 μm in diameter and are in a solution of NaCMC polymers at 0.075 mg mL^{-1} . (b) Plot of particle pair potential found by Boltzmann inversion. The data (dots) are well described by a Morse potential (blue line) with a minimum at approximately 70 nm gap distance. Because we are measuring only energy differences, the curve can be arbitrarily shifted; we set the energy level to zero at large gap distances. We fit the attractive regime to an Asakura-Oosawa (AO) model (gray curve) of hard-sphere depletant interactions, with best-fit parameters $r_l = 0.695 \mu\text{m}$, $r_s = 67 \text{ nm}$, and $\varphi = 0.29$.

where $\beta = 1/k_b T$, k_b is the Boltzmann constant, and T is the temperature. We can invert this relation to obtain

$$\frac{U(r)}{k_b T} \propto -\ln [p_b(r)]. \quad (5.2)$$

We can measure $p_b(r)$ by first constructing a histogram of the distribution of particle distances r (Fig. 5.1a). By taking the negative natural log of the frequencies and plotting against the distance r , we arrive at a model-free inference of the particle pair potential. This method of inverting the Boltzmann distribution can only resolve energy *differences*. As such, the entire curve can be shifted arbitrarily up and down, with the zero-point energy typically set by where the energy approaches a flat line at sufficiently large r .

We first use this method to analyze a measurement of a distribution of gap distances between two spheres 1.3 μm in diameter, freely diffusing in 3D in a solution of a polymer with a radius of gyration of approximately 60 nm at a concentration of 0.075 mg mL^{-1} . We find that this concentration of depletant results in a bond lifetime that is well suited to this method: the particles are strongly

bound, such that they stay together for longer than the 30 s videos, but they also sample many distances, which is important for resolving longer-range energy levels.

We find that the pair potential found by Boltzmann inversion for this system is well described by a Morse function (Fig. 5.1b), with an energy minimum at a gap distance of about 70 nm. The minimum presumably emerges from the balance between electrostatic repulsion between the charge-stabilized spheres and the attractive force from the depletant particles. We estimate the attractive term in the potential by fitting the data to a hard-sphere model of the Asakura-Oosawa potential (see Section 5.2.1), which gives best-fit parameters of $r_l = 0.695 \mu\text{m}$, $r_s = 67 \text{ nm}$, and $\phi = 0.29$. We have previously characterized the radii of the large particles to be approximately 0.664 μm , but we expect the radius inferred from the simple AO model to be larger than the hard-sphere radius because it includes electrostatic repulsion effects. The inferred radius of the depletant polymer is slightly larger than the radius of gyration of 60 nm, but again includes charge effects. The discrepancy between the inferred and expected volume density of polymers, expected to be about $\phi = 0.1$, likely also arises from electrostatic effects, as discussed in the following section.

The Boltzmann inversion method does not require any assumptions about the underlying form of the potential curve, and has been used to elucidate unexpected behavior at high concentrations of depletant particles¹⁹⁸. The inferred particle pair potential also contains a wealth of information about the shape and range of the interaction.

There are, however, drawbacks to this method. First, the depth of the potential well, an important feature for determining the behavior of a colloidal suspension, is ill-constrained, as the zero-point of the energy depends on knowing the distance at which the potential is negligible. The larger issue is the strong dependence of the inferred potential on the choice of number of histogram bins. When the bin size is smaller than the precision on the gap measurements ($\pm 2 \text{ nm}$), we find differences in the shape of the potential curve (Fig. 5.2). More importantly for our purposes, binning the distances reduces the precision we have achieved with holographic microscopy, and makes it difficult

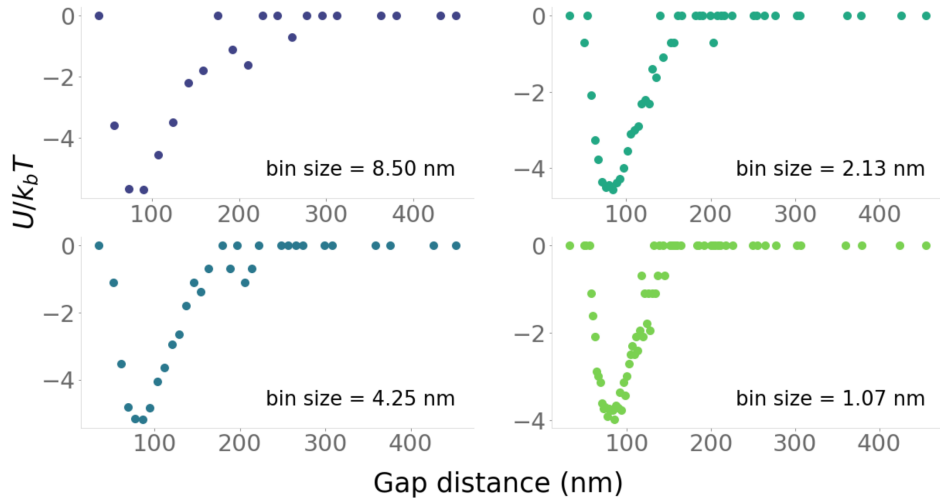


Figure 5.2: Pair potential inferred by Boltzmann inversion of histograms with varying bin size. Dots represent the locations of the bins of the histogram, plotted against the negative log of the frequencies. When the width of the histogram bin used to estimate the probability density function is smaller than the precision of the measurements of gap distance (± 2 nm), artifacts arise in the shape of the potential curve. Conversely, when the bins are around the same width as the width of the potential well, we obtain a worse estimate of the curvature about the minimum.

to account for the uncertainties on those gap distances.

5.2 FITTING BOLTZMANN MODEL TO FULL DISTRIBUTION

We now consider a model-based approach to this data analysis that is not subject to the limitations of the inversion method. We model the underlying particle potential $U(r)$, then find the parameters of that model that best describe the observed distribution of distances $p(r)$ in equilibrium. This method has the advantages of not binning or reducing the data, and it also rigorously accounts for the uncertainties on each frame.

To implement this method, we rewrite Equation 5.1 with a normalization factor Z to arrive at a distribution

$$p(r)dr = \frac{1}{Z} \exp [-\beta U(r)], \quad (5.3)$$

where

$$Z = \int_a^b \exp [-\beta U(r)] dr, \quad (5.4)$$

and a and b are the boundaries of the support of $p(r)$.

If the data $\{r\}$ are independent and identically distributed (IID), we can write the likelihood function of all the data points as

$$p(\{r\} | \theta) = \prod_{i=1}^N \frac{1}{Z} \exp [-\beta U(r_i | \theta)], \quad (5.5)$$

where θ is the vector of parameters for the potential and N is the number of data points. The log likelihood is then given by

$$\ln p(\{r\} | \theta) = -N \ln Z + \sum_{i=1}^N [-\beta U(r_i)]. \quad (5.6)$$

With this parameterization, as well as priors on the parameters, we can find the θ that maximize the log posterior for a distribution of observed data points $\{r\}$. However, we must first consider how to parameterize the model for $U(r)$ by considering the sum of forces acting in our system.

5.2.1 MODELS OF SHORT-RANGED INTERACTIONS

The depletant polymers in the solution induce an entropically driven attraction between the larger colloidal spheres. This attraction arises from the depletant polymers being physically excluded from the interior of the larger particle. The region around each large sphere that the polymers cannot penetrate is called the excluded volume. When the two spheres touch, their excluded volumes overlap, and there is more configurational space available to the depletants. Thus, it is entropically favorable for the larger spheres to come into contact. Alternatively, we can conceptualize the attractive force in terms of osmotic pressure. When the spheres approach each other, there is a distance at

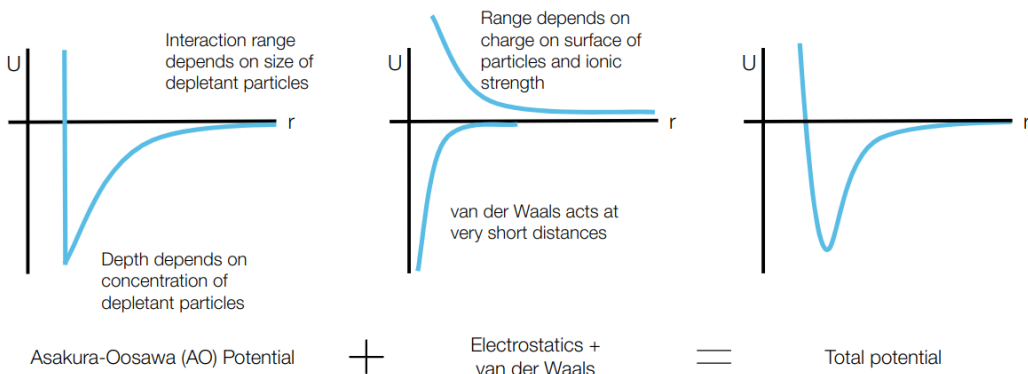


Figure 5.3: Schematic of attractive and repulsive interactions between colloidal particles in the experiments, shown as sketches of particle potentials. The attractive potential induced by depletant polymers can be modeled through the Asakura-Oosawa (AO) theory. This attractive potential depends on the concentration and size of the depletants. The electrostatics and van der Waals interactions can be modeled by DLVO theory. We expect the total interaction to be the sum of all these forces, with a potential well with some curvature and range.

which the depletant polymers cannot physically fit between the spheres. The resulting pressure differential draws the spheres together.

The excluded volume depends on the center-to-center distance r and the relative radii of the two species of spheres. In the hard-sphere approximation, we can consider the limits of the interaction as follows. When the particles are touching, there is an infinite hard-sphere repulsion at a length scale set by the diameter of the large spheres. On the other extreme, the potential goes to zero when there is no overlap of the excluded volume, at a length scale set by the diameter of the depletant particle. In between, the potential depends on the overlap in the excluded volumes, which can be determined geometrically as a function of the particle separation. This quantitative calculation leads to the Asakura-Oosawa (AO) model²²¹.

The AO model is typically parameterized in terms of the number density of the depletant particles, but more generally, the depletion potential should scale with the osmotic pressure of the poly-

mer:

$$\frac{U_{AO}(r)}{k_b T} = \begin{cases} -\frac{\pi}{6} \frac{\Pi}{k_b T} (2\alpha_s + 2\alpha_l - r)^2 \times (2\alpha_s + 2\alpha_l + \frac{r}{2}) & \text{for } r < (2\alpha_l + 2\alpha_s) \\ 0 & \text{otherwise,} \end{cases} \quad (5.7)$$

where Π is the osmotic pressure of the depletant polymers, α_s is the radius of the depletants, α_l is the radius of the larger particles, and r is the distance between the two spheres²²². The number density and scaled osmotic pressure $\Pi/k_b T$ are equal only in the limit of low concentration. For polyelectrolytes, like NaCMC, the second virial coefficient can be significant at small ionic concentrations²²³.

We expect additional interactions between the spheres arising from van der Waals forces and electrostatics. These interactions can be modeled with DLVO (Derjaguin and Landau, Verwey and Overbeek) theory, which models both electrostatic repulsion between the two like-charged colloidal spheres and the strong short-ranged attraction from van der Waals forces. However, the strong van der Waals attraction only occurs at very small particle distances, which the particles do not typically explore unless the electrostatic screening is strong, such as at high salt concentrations. For our experiments, the salt concentration is low and we therefore neglect van der Waals forces. We model the electrostatic interactions as a screened Coulomb repulsion between the two spheres, where the electrostatic effects are given by a double-layer model. In this model, the free ions in solution form a diffuse layer about the charged surface, with a thickness set by the Debye screening length²¹¹. The potential can be written as

$$\frac{U_{DLVO}(r)}{k_b T} = Z^2 \lambda_B \left(\frac{e^{\kappa \alpha_l}}{1 + \kappa \alpha_l} \right)^2 \frac{e^{-\kappa r}}{r}, \quad (5.8)$$

where Z is the surface charge valence of each large sphere, λ_B is the Bjerrum length, κ^{-1} is the Debye length, and α_l is the radius of the large particles.

The sum of these interactions gives the total pair potential:

$$\frac{U(r)}{k_b T} = \frac{U_{AO}(r)}{k_b T} + \frac{U_{DLVO}(r)}{k_b T}. \quad (5.9)$$

5.2.2 GENERIC REPULSIVE TERM

However, the full AO-DLVO model is ill-suited for this experimental system, because the Debye-Hückel screening model is not necessarily accurate for a dense suspension of polyelectrolytes, such as the depletant polymers used here. It is difficult to define a screening length based on the ionic concentration because the polymers do not act as simple free ions. The AO potential is also a flawed representation of the depletant interaction in our system, as neither the polymer nor the spheres act as true “hard” spheres; both are charged. It is also unclear in what regimes the polymers act as spheres at all. It is possible that at large concentrations, the polymers begin to overlap or absorb onto the particle surface. Moreover, it is not necessarily true that the AO and DLVO interactions should be purely additive, since they were developed under different regimes and assumptions.

We instead approximate the interactions at low polymer concentration as a hard sphere-depletant interaction parameterized in terms of the osmotic pressure (Equation 5.7) with a generic repulsive term that approximates the screened Coulomb repulsion between the spheres. We parameterize the repulsive term as

$$\frac{U_{rep}(r)}{k_b T} = e^{-C[x-2(a_l+D)]}. \quad (5.10)$$

This formulation adds two constants to the model: C , which scales the strength of the repulsive term, and D , which shifts the repulsive term along the line connecting the sphere centers. Equivalently, the parameter D scales the prefactor of the exponential. We add the two terms to approximate the interaction as

$$\frac{U(r)}{k_b T} = \frac{U_{AO}(r)}{k_b T} + \frac{U_{rep}(r)}{k_b T}. \quad (5.11)$$

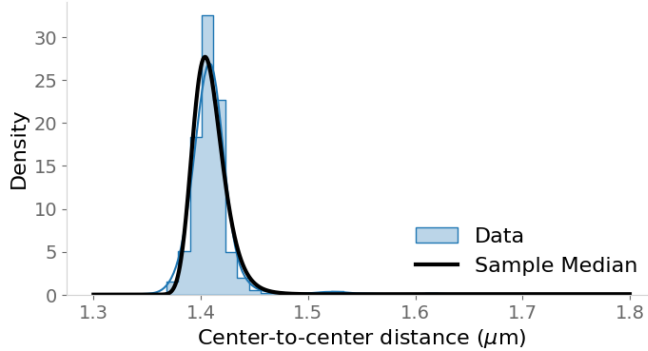


Figure 5.4: Inferred probability density for a Boltzmann distribution parameterized in terms of AO attraction and a generic repulsion fit to a full distribution of particle distances (trajectory shown in Figure 5.1a). The shape of the best-fit distribution (black), given by the median of the sample, matches the data (light blue) and the kernel density estimate (blue) of the distribution of particle distances well, even with a simplified model for the electrostatics.

To fit this model to the full distribution of gap distances, we use a No-U-Turn sampler (NUTS) as implemented by the Python package `pymc`²²⁴. This package is designed for fast exploration of posterior probability densities through automatic differentiation and Hamiltonian dynamics. We define the priors on each parameter as

$$\begin{aligned}
 a_s &\sim \text{Truncated Normal}(\mu = 0.070, \sigma = 0.05, \text{lower} = 0, \text{upper} = 0.1) \\
 a_l &\sim \text{Truncated Normal}(0.695, 0.1, \text{lower} = x_{\min}/2, \text{upper} = 0.8) \\
 \rho &\sim \text{Gamma}(\mu = 400, \sigma = 100) \\
 C &\sim \text{Gamma}(100, 100) \\
 D &\sim \text{Normal}(0, 0.01),
 \end{aligned} \tag{5.12}$$

where the mean and spread of the prior on the particle sizes are given by manufacturer’s specifications or size estimates. We initialize the sampler with the “jitter + adaptive diagonal” tuning method, which uses information from gradients to tune the step size and the number of steps per sample. To calculate the normalization factor Z in Equation 5.6, we implement a numerical integrator.

We find that the best-fit $U(r)$ predicts a distribution that matches the distribution of the data

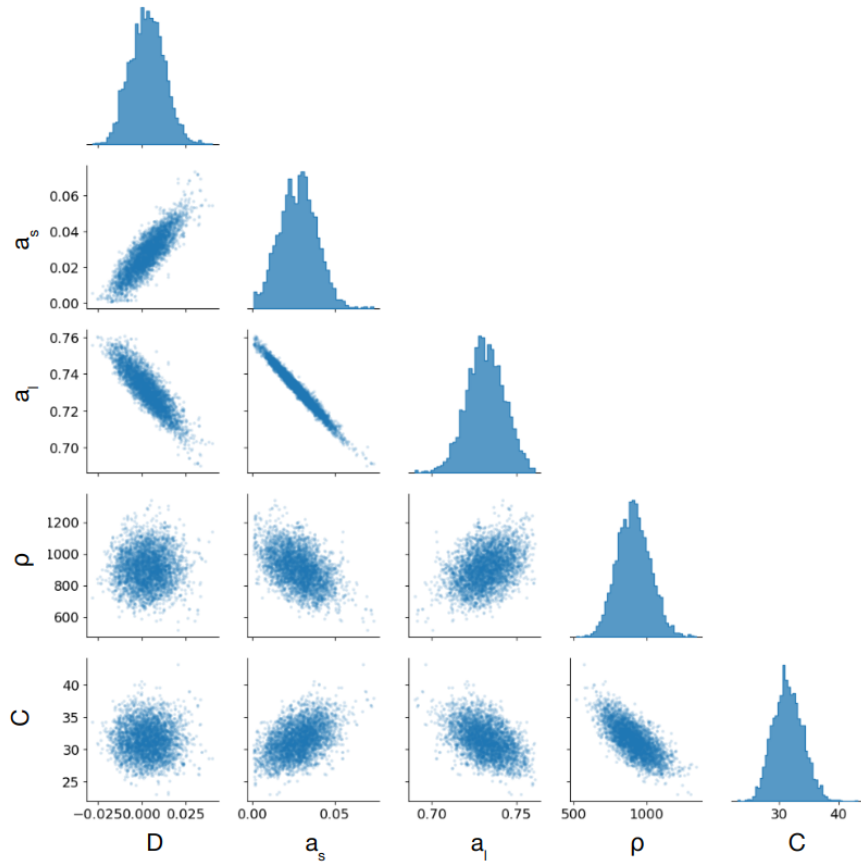


Figure 5.5: Posterior of AO model with generic repulsive term obtained by fitting a Boltzmann distribution to the distribution of gap distances. The marginalized best-fit parameters for each parameter are shown on the diagonal.

well (Fig. 5.4). However, the inferred parameters (shown in Fig. 5.5) present some complications.

First, there are strong covariances between the inferred sizes of the colloidal particles and the depletant polymer, as shown by the skew of the 2D marginalized posterior of those parameters. This covariance makes it difficult to independently infer the sizes of each particle. The sampler finds a MAP value for the polymer size of $a_s = 28 \text{ nm}$ (compared to the expected $r_g \approx 60 \text{ nm}$) and a MAP value for the spheres size of $a_l = 0.73 \mu\text{m}$ (compared to the expected $r = 0.66 \mu\text{m}$).

Despite these limitations, the AO model with a generic repulsive term captures the position and curvature of the peak of distance distribution (Fig. 5.4). This curvature can be described by the

spring constant of the system, which estimates the stiffness of the bond from the second derivative about the potential minimum. While the functional form of the model makes it challenging to solve for the spring constant analytically, numerically solving for the curvature about the minimum gives a spring constant of $k = 5450 k_b T / \mu\text{m}^2$.

5.2.3 MORSE POTENTIAL

If we are only interested in the shape and curvature of the particle pair potential, we can use a general model that is more easily fit, specifically a Morse potential,

$$\frac{U(r)}{k_b T} = D_e \left[e^{-2\alpha(r-r_e)} - 2e^{-\alpha(r-r_e)} \right], \quad (5.13)$$

where D_e is the well depth, r_e is the location of the minimum, and α is the range parameter. The Morse potential is a reasonable approximation to the full AO-DLVO potential, but is far easier to fit to data.

To fit this model to the data, we use the NUTS sampler as implemented by `pymc` with the following priors:

$$\begin{aligned} r_e &\sim \text{Truncated Normal}(\mu = 1.5, \sigma = 0.3, \text{lower} = x_l, \text{upper} = 1.8) \\ \alpha &\sim \text{Truncated Normal}(30, 10, \text{lower} = 10, \text{upper} = 60) \\ D &\sim \text{Gamma}(\mu = 5.5, \sigma = 3). \end{aligned} \quad (5.14)$$

Pair plots of the posterior are shown in Figure 5.6a. Although the well depth and range parameters differ slightly from the best fit to the inverted histogram (shown in Fig. 5.1b), the curvature of a Boltzmann distribution with the best-fit Morse parameters matches the curvature of the peak of the distribution of the data.

We can quantify this curvature by solving for the spring constant in terms of the model param-

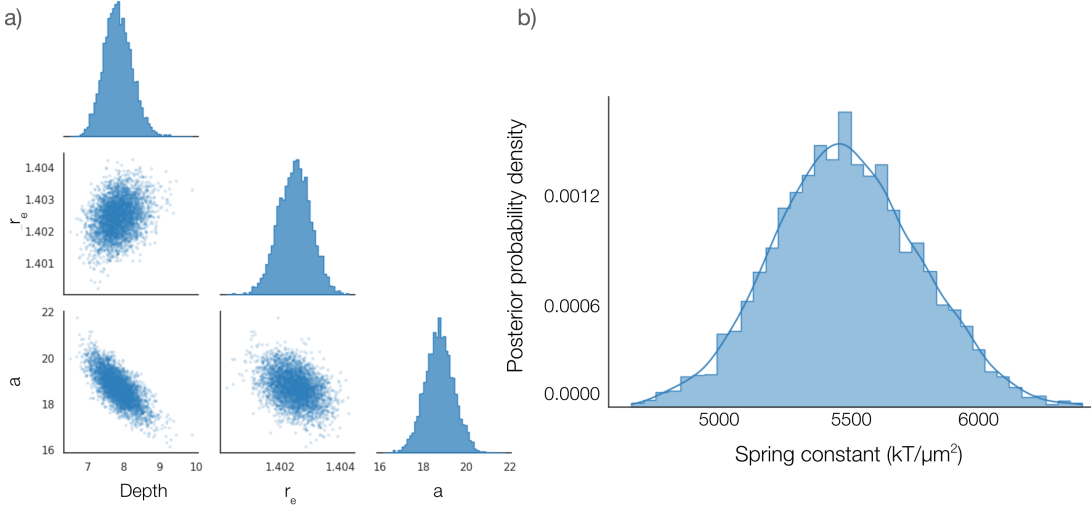


Figure 5.6: Posterior and spring constant from fitting a Boltzmann distribution with a Morse potential to the full distribution of gap distances. (a) Posterior and marginalized parameters for the Morse potential. (b) Marginalized posterior of the spring constant k , found by analytically solving for k in terms of the model parameters and plotted using the samples for these parameters.

eters. For a Morse potential, Taylor expanding the expression, truncating at the second derivative, and solving about the minimum position r_e yields

$$k = 2D_e a^2. \quad (5.15)$$

We use the Monte Carlo samples for a and D_e and marginalize over the other parameters to arrive at a posterior for the spring constant that accounts for all the uncertainties of our system, shown in Figure 5.6b. Approximating the curve as Gaussian, we arrive at an estimation of the spring constant as $k = 5480 \pm 270 \text{ } k_b T/\mu\text{m}^2$ for spheres $1.3 \text{ }\mu\text{m}$ in diameter, freely diffusing in 3D in a polymer solution at a concentration of 0.075 mg mL^{-1} . This result agrees with the results found from parameterizing the potential in terms of the AO model with a repulsive term, but with a much smaller computational time and a model that has less covariance between the parameters.

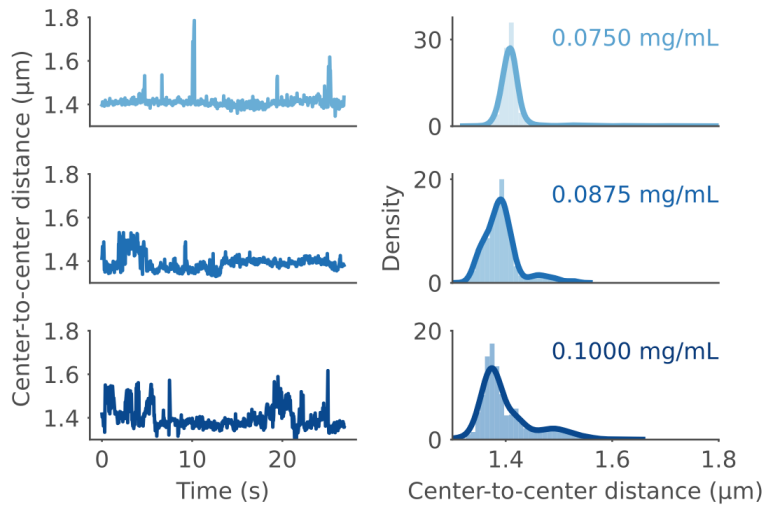


Figure 5.7: Trajectories (left) and histogram distributions (right) of particle gap distances with kernel density estimates for varying densities of depletant polymers. As the concentration of the depletant approaches the overlap concentration, the distribution of gap distances is no longer a single, well-defined peak. Instead, the distributions broaden and a secondary peak emerges at high depletant concentrations.

5.3 INCREASING DEPLETANT CONCENTRATION

Now that we have developed a set of tools for analyzing the distributions of gap distances obtained through holographic microscopy, what remains is to apply those tools to understand a range of systems. First, we compare the system we analyzed in the previous sections, a suspension with 0.075 mg mL^{-1} of 700,000 molecular weight NaCMC, to systems with a higher concentration of depletant polymers. We increase the polymer concentration until it is just below the expected overlap concentration of 0.11 mg mL^{-1} .

As the depletant concentration increases, we find that the particles no longer fluctuate about a single minimum position (Fig. 5.7). Instead, the distribution of the particle distances broadens and an additional peak appears approximately 120 nm from the primary peak. A secondary peak has been found in previous studies of the depletant interaction at high concentrations¹⁹⁸, where it

arises from the depletant particles forming layers about the larger particles. Although dense polyelectrolytes near the overlap concentration may not act as monodisperse spheres, we expect similar structuring effects to arise in this system.

While the distributions of the particle distances allow us to qualitatively describe the interactions at high depletant concentrations, it is evident that the distributions are no longer well described by the models for the particle pair potential detailed above. Therefore, any fits to a Morse potential to describe the spring constant of the system would not be reliable.

5.4 MEASUREMENTS OF PARTICLE INTERACTIONS ON GLASS SURFACE

The presence of a glass surface can introduce electrostatic interactions which affect the potential. Thus, for quasi-2D experiments in which particles are confined to a glass surface, it is important to characterize the interparticle potential on that surface. Although one of the main benefits of using holographic microscopy to track colloidal spheres is the three-dimensional information we can extract, it can also be used to track particles moving in two dimensions while accounting for any out-of-plane fluctuations they may experience.

For these experiments, the particles are $0.71\text{ }\mu\text{m}$ polystyrene spheres with 2 mM NaCl to screen interactions with the glass surface. We then add NaCMC with a molecular weight of $250,000$ and a radius of gyration of about 40 nm . We suspend samples at a range of concentration from 0.17 mg mL^{-1} to 0.40 mg mL^{-1} , well below the overlap concentration.

At the lowest depletant concentrations, the particles quickly fall apart, leading to an over-representation of large gap distances beyond the range of particle interactions (Fig. 5.8). We discuss how to more rigorously account for these effects in the following section, but in order to apply the straightforward Boltzmann inversion, we first restrict the histograms to small distances where the primary peak is clearly visible (Fig. 5.9). We see that increasing the depletant concentration increases

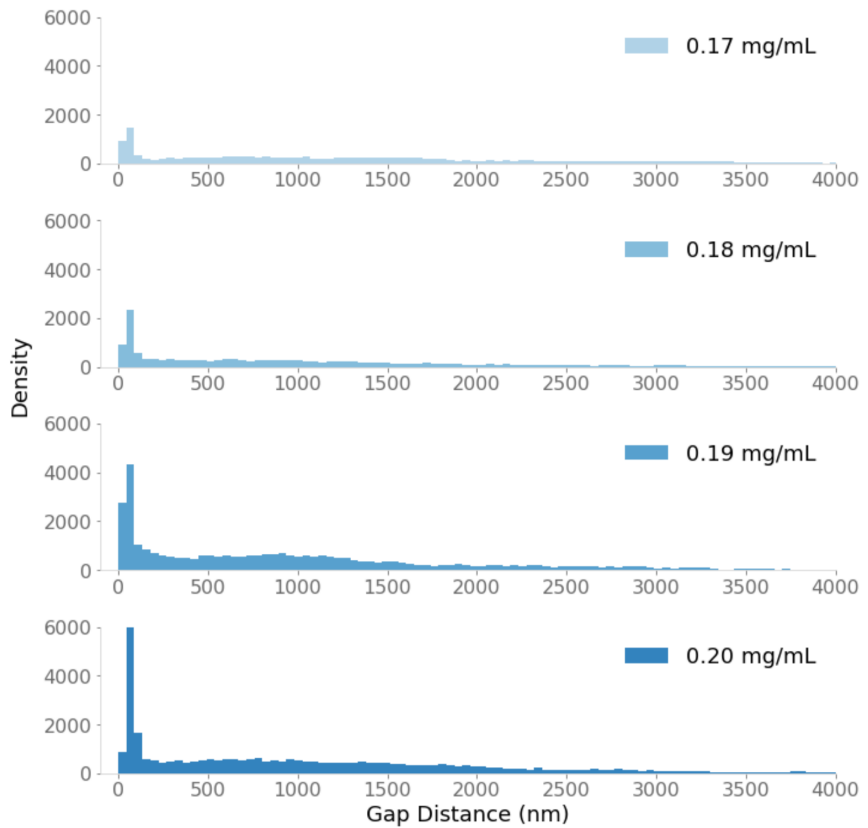


Figure 5.8: Full histograms of particle gap distance at varying depletant concentrations, from 0.17 mg mL^{-1} to 0.20 mg mL^{-1} . At the lowest concentrations, the particles quickly become unbound, oversampling large particle distances. At higher depletant concentrations, the particles remain bound longer, but still oversample large distances.

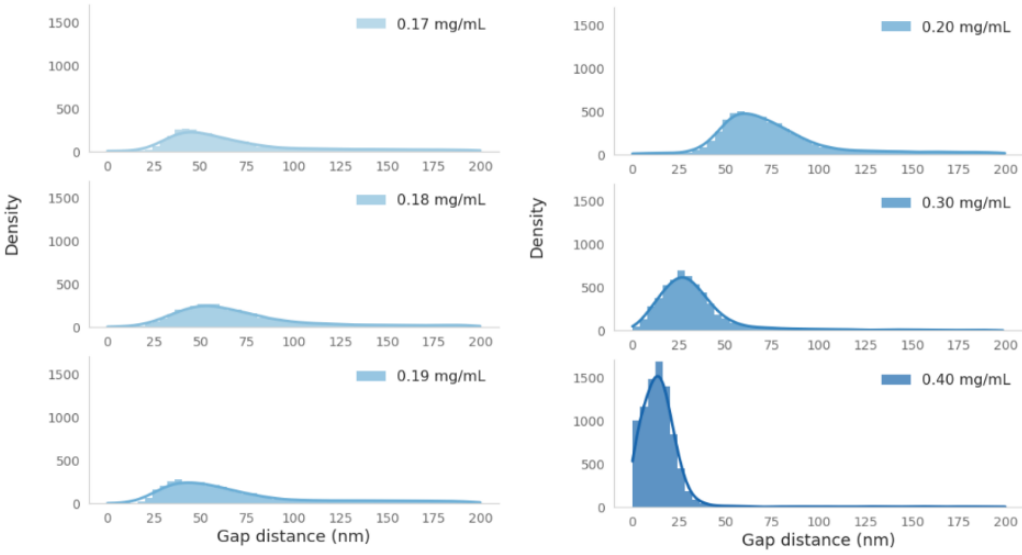


Figure 5.9: Histograms of particle gap distances less than 200 nm at varying depletant concentrations, from 0.17 mg mL^{-1} to 0.40 mg mL^{-1} . By focusing on the close particle distances, we resolve a single peak that increases as we increase the depletant concentration. At high depletant concentrations, the peak also shifts to smaller gap distances, potentially owing to electrostatic effects from the charged depletant polymers.

and narrows the peak of the histogram. It also shifts the peaks to smaller gap distances, possibly because the polymer screens the electrostatic repulsion.

Using the Boltzmann inversion method discussed in Section 5.1, we estimate the interparticle pair potential as a function of depletant concentration (Fig. 5.10). We fit the inverted histograms to a Morse potential and find that increasing the concentration of depletant polymers makes the potential well deeper and more narrow. Though the effects are subtle at the lower, more closely spaced depletant concentrations, the well depth increases significantly between the lowest and highest depletant concentrations, in accordance with our observations of different bond times.

5.4.1 ENTROPIC TERM IN BOLTZMANN DISTRIBUTION

Finally, we fit the full distribution of gap distances to a Boltzmann distribution with a Morse potential. First, to account for the increased configurational space available to the unbound particles, we

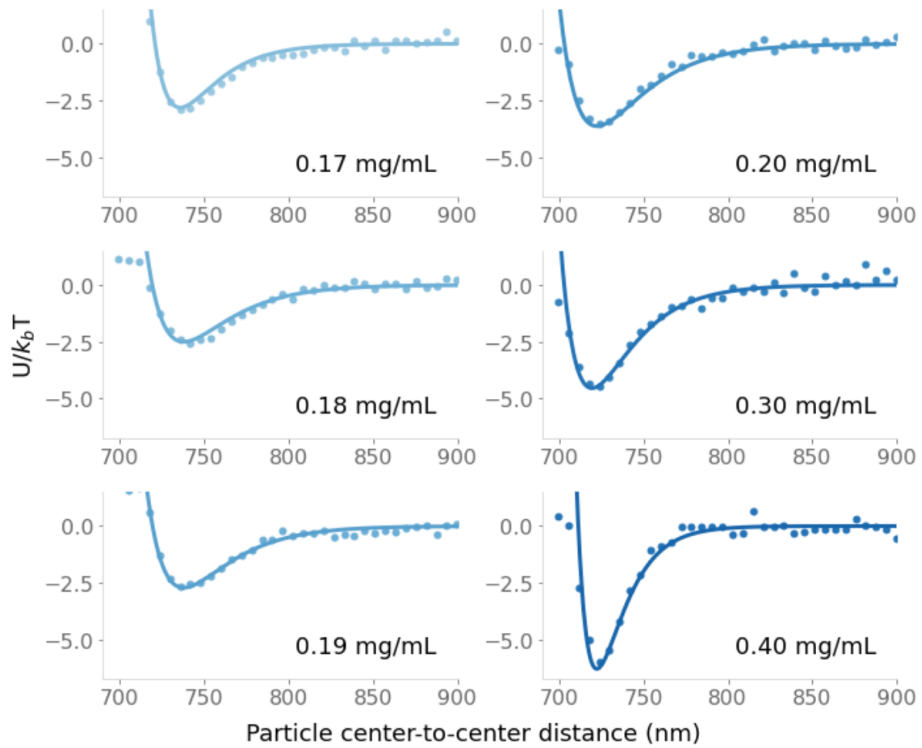


Figure 5.10: Boltzmann inversion (dots) and fits to a Morse potential (solid lines) for small particle gap distances at varying depletant concentrations, from 0.17 mg mL^{-1} to 0.40 mg mL^{-1} . Increasing the depletant concentration leads to a stronger interaction, as well as a narrower well.

include a term in the Boltzmann distribution that accounts for degeneracy, so that the distribution is now

$$p(r)dr = \frac{\Omega(r)dr \exp[-\beta U(r)]}{Z}, \quad (5.16)$$

where $\Omega(r)dr$ is the degeneracy of state r . For experiments confined in 1D, this degeneracy is one: there is only one configuration for every gap distance. In 2D, any given gap distance r could be observed on the circumference of a circle with radius r . In 3D, this configurational degeneracy goes as r^2 , as the particles can be positioned anywhere on the surface area of a sphere with radius r and still have the same gap distance. Therefore

$$p(r)dr = \frac{4\pi r^2 dr \exp[-\beta U(r)]}{Z}, \quad (5.17)$$

where

$$Z = \int_a^b 4\pi r^2 \exp[-\beta U(r)] dr, \quad (5.18)$$

and a and b are the boundaries of the support of $p(r)$. Simplifying, we find

$$p(r)dr = \frac{r^2 \exp[-\beta U(r)]}{\int_a^b 4r^2 \exp[-\beta U(r)] dr}. \quad (5.19)$$

Again, if the recorded data $\{r\}$ are IID, the likelihood function factorizes as

$$p(\{r\} | \theta) = \prod_{i=1}^N \frac{r_i^2}{Z} \exp[-\beta U(r_i | \theta)], \quad (5.20)$$

where θ is the vector of parameters for the potential and N is the number of data points. We can then write the log likelihood function as

$$\ln p(\{r\} | \theta) = -N \ln Z + \sum_{i=1}^N [2 \ln r_i - \beta U(r_i)]. \quad (5.21)$$

We evaluate the partition function as before with an integrator evaluated over the boundaries of the support for $p(r)$. With this formulation, we can optimize the log posterior function while accounting for the increased configurational space available to the particles.

5.4.2 SPRING CONSTANTS

We fit this model using the same NUTS sampler as before, with modified priors to account for the differences in the experimental system. The priors are given by

$$\begin{aligned} r_e &\sim \text{Truncated Normal}(\mu = 0.75, \sigma = 0.05, \text{lower} = x_l, \text{upper} = 0.9) \\ \alpha &\sim \text{Truncated Normal}(30, 10, \text{lower} = 10, \text{upper} = 60) \\ D &\sim \text{Gamma}(\mu = 4, \sigma = 4). \end{aligned} \tag{5.22}$$

To limit computational time, we limit the integrator to center-to-center distances between 0.65 μm and 4.0 μm , far beyond the expected range of interaction.

We marginalize the sampled posterior to arrive at a posterior probability density for the spring constants of each system (Fig. 5.11). While most of the marginalized posteriors are approximately Gaussian, the distributions of 0.17 mg mL^{-1} and 0.20 mg mL^{-1} have a noticeable skew, which arises because the distribution of the potential parameters is cut off by the limits on the priors.

We estimate the MAP value of the distribution and the uncertainty as the 1σ width of the distribution:

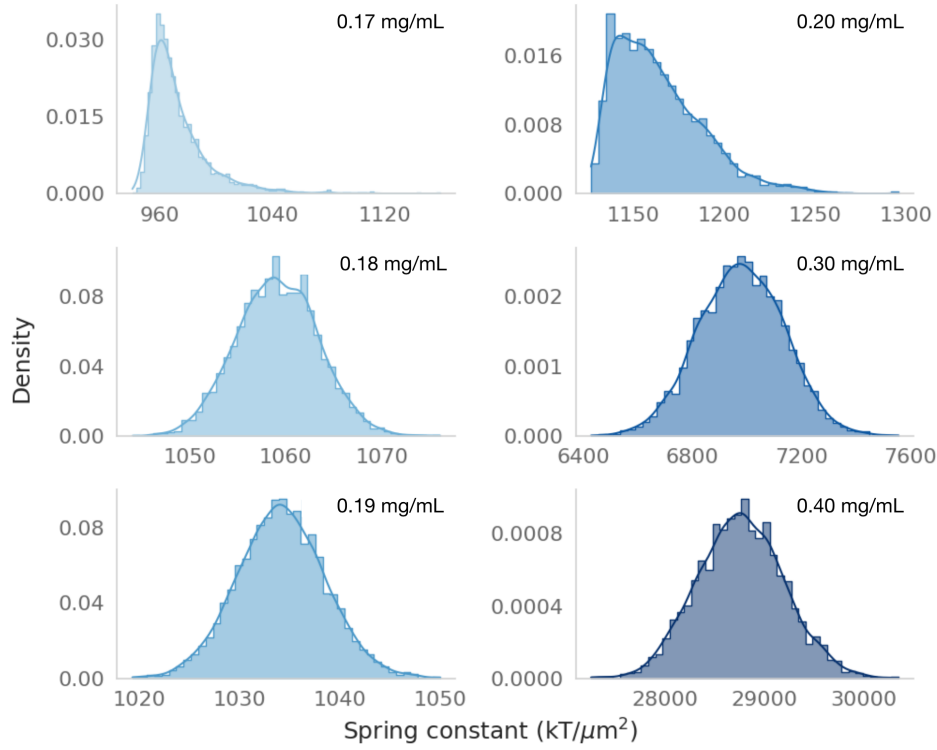


Figure 5.11: Marginalized posterior probability density of spring constants for various depletant concentrations. Increasing the depletant concentration increases the bond stiffness of the system by orders of magnitude. The skew in some of the distributions (0.17 mg mL^{-1} and 0.20 mg mL^{-1}) arises from skews in the inferred Morse parameters.

Concentration (mg mL ⁻¹)	Spring constant ($k_b T/\mu\text{m}^2$)
0.17	973 ± 24
0.18	1058 ± 4
0.19	1034 ± 4
0.20	1164 ± 25
0.30	6980 ± 160
0.40	28760 ± 440

As the depletant concentration increases, the bond stiffness increases significantly, though non-monotonically. Because the polymers are charged, increasing their concentration changes both the attractive depletant forces and the repulsive electrostatic terms; these electrostatic effects may be responsible for the complex response we see in the bond stiffness.

5.5 CONCLUSION

With the high-precision measurements of particle gap distances made with holographic microscopy, we can understand the underlying pair potential of two colloidal spheres. Through the different analyses outlined above, we can quantify the bond stiffness of the system, estimate the interaction range, and obtain quantitative information about the shape of the entire pair potential that arises from the balance of depletant-driven attraction, electrostatic repulsion, and van der Waals forces.

We have shown that this method can directly quantify interactions at the nanometer scale in both two and three dimensions, making it a powerful tool for characterizing interactions *in situ*. In principle, accurate measurements of particle interactions can be used to predict the phase behavior or assembled structure of colloidal particles. In the conclusion chapter, I discuss preliminary work to relate these inferred interactions to crystallization experiments in the same system.

The method could be extended to other systems. The simplest extension would be increasing the

number of particles from two to three, a regime still easily accessible with holographic microscopy and generative modeling. By measuring the pair and three-body potentials directly, we could test whether the interactions are additive²¹⁷. Other possible extensions include measurements of the depletant interaction for non-spherical particles²²⁵, as well as measurements of more complex interacting particles, such as living cells, especially those that are too delicate to be confined or manipulated with optical tweezers.

There are some limits to the interactions one can probe with these methods. For one, a generative modeling approach to holographic microscopy is best suited to the dilute limit, where there are a limited number of parameters to infer. It would be challenging, if not computationally impossible, to quantify *bulk* interactions between particles and to examine how they differ from sums of the pair potential. In the following chapter, I briefly discuss a collaborative effort to analyze the trajectories of many interacting particles in order to infer their underlying potential. Another limitation is the problem of sampling. The analysis we outlined above is best suited to particles that have a potential well and therefore remain close to one another throughout the experiment. Purely repulsive spheres or active particles would be more challenging to probe. Holographic microscopy can be used to track particles over a wide range of 3D spaces. In principle, any interaction that depends on relative particle positions could be measured with holographic microscopy.

*We know you can never do it properly - once and for all.
Passion is never enough; neither is skill. But try.*

Toni Morrison, *Nobel Lecture In Literature, 1993*

6

Conclusion

The contents of Section 6.2 are being prepared in the following manuscript:

“Inferring interaction potentials from stochastic particle trajectories.” Ella M. King, Megan C. Engel, Caroline Martin, Alp M. Sunol, Qian-Ze Zhu, Sam S. Schoenholz, Vinodhan N. Manoharan, and Michael P. Brenner.

The material in this chapter is based upon work supported by the National Science Foundation Graduate Research Fellowship under Grant No. DGE1745303, the Harvard Materials Research

Science and Engineering Center (DMR 20-11754), the Office of Naval Research (ONR N00014-17-1-3029), and the Department of Defense through the National Defense Science and Engineering Graduate Fellowship. The authors thanks Ryan Krueger and Chrisy Xiyu Du for helpful discussions.

IN THIS THESIS, I HAVE DETAILED how we can use a generative modeling approach to holographic microscopy to extract quantitative information about colloidal dynamics. I have shown that the generative model we chose can strongly affect the accuracy of our inferred parameters, and I have developed models that improve the accuracy of particle tracking and characterization by accounting for optical effects. I have used these improved models to characterize very small gap distances between two particles. Finally, I have analyzed distributions of those gap distances to understand particle interactions in the presence of a charged polymer depletant.

Here, I discuss ongoing work that expands upon the work detailed in Chapter 5, including using characterizations of particle pair potentials to compare experiment to simulation and developing alternative approaches to inferring pair potentials of many interacting particles.

6.1 INFORMING AND COMPARING TO SIMULATION

One of the appeals of accurately characterizing particle interactions is predictive power: if we understand how individual particles interact, we can predict their bulk behavior, such as crystallization, phase behavior, or structure formation. To investigate whether we can achieve this predictive power, I am collaborating with Dr. Jessica Sun and Dr. Alp Sunol to connect the particle pair potentials I infer to particle crystallization in both experiment and simulation.

To do so, we simulate many particles interacting in 2D via a Morse potential with the best-fit parameters found by the Boltzmann inversion method discussed in the prior chapter. We simulate par-

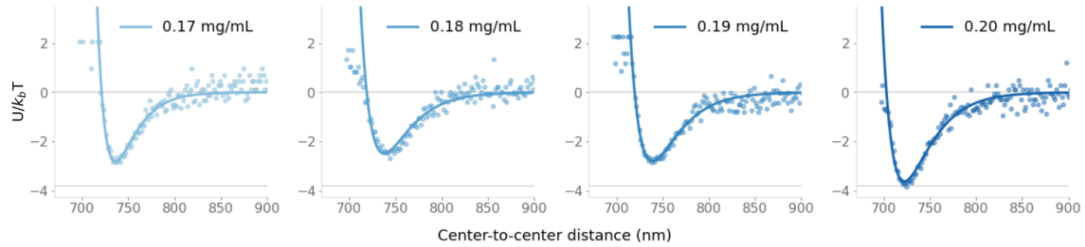


Figure 6.1: Measured particle interactions from Boltzmann inversion and best-fit Morse potential at varying depletant concentration. Subset of the fits shown in Figure 5.10.

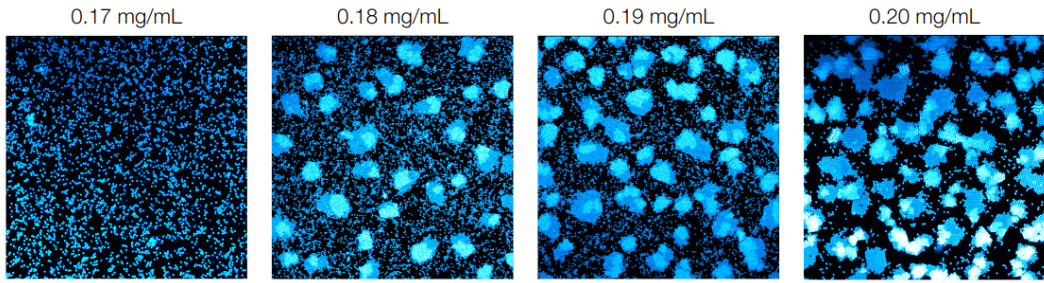


Figure 6.2: Confocal images of fluorescently labeled $0.7 \mu\text{m}$ spheres with increasing concentrations of NaCMC depletant polymers. Increasing depletant concentration triggers particle crystallization. Data taken by Jessica Sun.

ticles with a differentiable molecular dynamics code package called JAX-MD²²⁶. The pair potentials used for the simulations are shown in Figure 6.1. We compare the simulation results to experiments of particles assembling into crystals on glass surfaces, as observed by Jessica Sun. Confocal images of the particles show a strong dependence of the phase behavior on depletant concentration (Fig. 6.2).

We plan to compare the forward-simulations to the experimental behavior by characterizing the particle correlation function $g(r)$ for both the simulations and experiments. Although we do not find that the inferred particle potentials get monotonically deeper, we do find that as we increase the depletant concentration, the bond stiffness of the system increases overall. It will be interesting to observe the degree of sensitivity of the structure to the Morse potential, and to connect our direct measurements of particle interactions with observable phase behavior.

6.2 OTHER METHODS OF INFERRING PARTICLE PAIR POTENTIALS

Up until now, the methods I have outlined for inferring pair potentials rely on observing only a few particles at a time, a condition that could be very different from *in situ* environments of the systems of interest. Moreover, any method that assumes that the particle positions are Boltzmann distributed inherently assumes that the system is in equilibrium. There are several situations for which these assumptions would not hold, including active matter, many-body interactions, or velocity-dependent interactions.

An alternative approach to inferring particle interactions is to infer force fields directly using experimental trajectories of interacting particles. In collaboration Dr. Ella King, Prof. Megan Engel, Dr. Alp Sunol, Qian-Ze Zhu, Sam Schoenholz, and Prof. Michael Brenner, I have worked to develop a maximum-likelihood-based method for inferring particle interactions by explicitly solving the equations of motions to find a form of the potential that maximizes the probability of observing a known trajectory. The method we developed is valid for systems both in and out of equilibrium, is well-suited to large numbers of particles interacting in typical system conditions, and does not assume a functional form of the interaction potential. The approach can be applied equally to non-equilibrium data, opening up a new frontier of experimental settings – including active matter systems, defects in active nematics, cell-cell interactions, and tribocharged particles – for which interparticle interactions can be inferred.

The experimental trajectories we record are of colloidal particles experiencing depletion interactions and electrostatic repulsion. We suspend 1.3 μm charge-stabilized colloidal spheres and induce a depletant interaction with carboxymethyl cellulose salt polymers with a radius of gyration of 60 nm. We allow these spheres to deplete to the bottom surface of the chamber, confining the system to a quasi-2D geometry. The charge-stabilized particles are like-charged and repulsive, and the addition of the depletant polymers into the system induces an entropically-driven attractive force that mini-

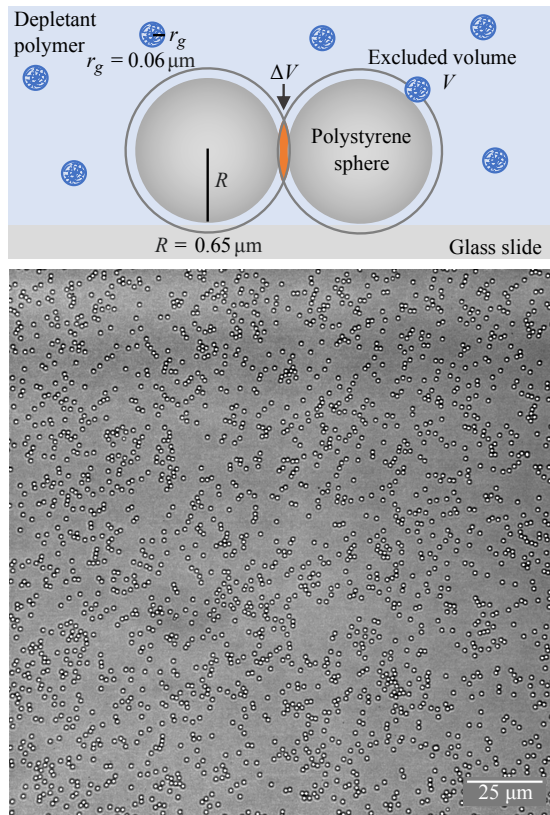


Figure 6.3: Diagram of experimental system. Charge-stabilized polystyrene spheres are suspended with depletant polymers with a radius of gyration of approximately $0.06 \mu\text{m}$. The depletants induce an entropically-driven attraction between the larger spheres, with a range set by the size of the polymers. The spheres are depleted to a glass slide and freely diffuse in the quasi-2D sample chamber.

mizes the volume excluded to the depletant particles (Fig. 6.3), leading to an overall attractive interaction. The range of the depletion interaction is set by the diameter of the depletant particles (0.12 μm), while the point of infinite energy is set by the center-to-center distance of the two spheres (1.3 μm). We record bright-field images of these diffusing and interacting particles, and recover particle trajectories using `trackpy`²²⁷.

To maximize the log likelihood function, we can either infer the best fit parameters for a particular functional form of the potential or we can fit the potential to a general functional form. Graph Neural Networks (GNNs) are an especially appealing choice, as they implicitly include physical priors of locality and distance dependence of interparticle potentials. Using a GNN, we reconstruct an experimental interaction potential from particle trajectories (Fig. 6.4a). We compare this potential to an inverted histogram of all interparticle separations, which gives the potential of mean force (PMF) according to

$$U(x) = -k_b T \log p(x) \quad (6.1)$$

where $p(x)$ is the probability of an interparticle distance falling into bin x ; the results are shown as black dots in Figure 6.4a. At low particle densities, the PMF can serve as a rough estimate of the pair potential, assuming that the system is at equilibrium and only exhibits pairwise interactions.

We find good agreement between the potential inferred by the GNN and the experimental potential near the well. Both methods return a measure of the colloidal radius and depletion interaction range that agree with previous characterizations. Additionally, the depth and curvature of the GNN potential matches the experimental results near the potential minimum.

We can further compare the results using the pair correlation function $g(r)$. We run forward simulations with Jax-MD with particles with the inferred potential and compare the resulting particle structure to the experimental data (Fig. 6.4b). The inferred potential reproduces several features of the experimental $g(r)$, including the height and location of the primary peak as well as a small

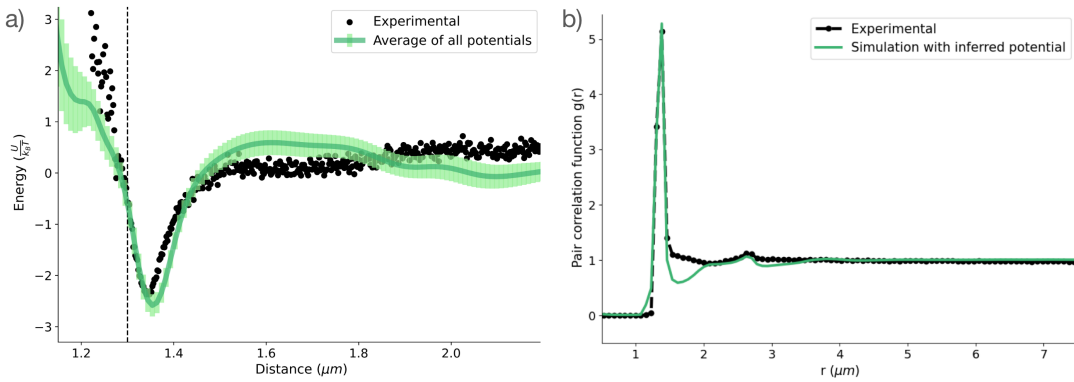


Figure 6.4: Plots of experimental data compared to inferred particle potential. (a) Inferred interaction potential is shown with a solid green line with shaded error bars set by variations over many trials. Experimental data is shown with black scatter points, given by inverting a histogram of particle positions. The two lines have reasonable agreement near the potential well. The vertical dashed line indicates the expected particle diameter. (b) The pair correlation function for the experimental data compared to the pair correlation function of forward-simulated particles with the inferred potential.

secondary peak, in addition to matching the long-ranged behavior.

There remain a few open questions to address, the biggest of which is how to account for entropic effects at a finite density. It is unknown whether this method could resolve two very different underlying potentials that give the same structure – say, a crystal that seems to be made up of attractive particles but in fact is made up of hard sphere particles driven to crystallize by entropy. It is possible that this could be resolved by sampling more particle trajectories, but it is also possible that some prior knowledge of the potential would be needed to differentiate them. One potential method to more rigorously account for entropic effects at a finite density is to vary the density and extrapolate to the dilute regime, a method outlined by Iacovella and coworkers²¹⁹.

6.3 OUTLOOK

Across length scales, life depends on the arrangement of subunits into larger, more complex structures: proteins fold into secondary structures, phospholipids assemble into bilayers, cells coordinate to form tissues. These microscopic structures of life emerge, in part, due to particle inter-

actions driving the emergence of a particular structure. Although the microscale dynamics and forces in these systems are rich for study, they are also hard to probe. Advances in microscopy have pushed resolution of single-molecule dynamics with methods such as interferometric scattering microscopy^{178,179} or *in vitro* images with methods such as two-photon microscopy²²⁸. But I argue that the future of microscopy lies not necessarily in the resolution of *images*, but in the resolution of *information*. To unravel the dynamics, forces, and interactions in these complex microscopic systems, we need quantitative, 3D information about how the components are moving.

However, it is often true that improvements in quantification must wait on improvements in computation. This is certainly true of holographic microscopy. Though generative models for light scattering had long been developed, fitting those models to holographic data had to wait for the advent of computers powerful enough to compute those scattering solutions^{173,174}. All the methods I used throughout my thesis were enabled by fairly recent developments in statistical inference and machine learning. In fact, the work I described in Chapters 4 and 5 to infer particle interactions is something that my group had been working on for over a decade. The additional progress I made is in part thanks to the larger progress of inference methods as a whole.

I anticipate that future progress in understanding colloidal physics using holographic microscopy will be enabled with even more powerful computational tools, such as advances in machine learning models or scattering solutions built with auto-differentiable code. Advances in colloidal sciences have long depended on technological advances, from Brown's microscope to the advent of digital video microscopy to improvements in particle tracking algorithms. I anticipate that in another decade, the computational tools I have spent my PhD developing will seem laughably slow. But though I know the methods outlined here will soon sink down into disuse, I hope they will become a foundation upon which more work will be built, reaching, perhaps, to something true.

References

- [1] W. Bentley, “Studies among the snow crystals during the winter of 1901-2, with additional data collected during previous winters,” *Monthly Weather Review*, vol. 30, no. 13, pp. 607–616, 1902.
- [2] K. G. Libbrecht, “Laboratory Snow Crystals,” in *Snow Crystals*, p. 185, Princeton University Press, 2021.
- [3] A. F. Demirörs, K. Manne, S. Magkiriadou, and F. Scheffold, “Tuning disorder in structurally colored bioinspired photonic glasses,” *Soft Matter*, vol. 20, no. 7, pp. 1620–1628, 2024.
- [4] M. He, J. P. Gales, E. Ducrot, Z. Gong, G.-R. Yi, S. Sacanna, and D. J. Pine, “Colloidal diamond,” *Nature*, vol. 585, pp. 524–529, Sept. 2020.
- [5] W. Poon, “Colloids as Big Atoms,” *Science*, vol. 304, pp. 830–831, May 2004.
- [6] G. Meng, N. Arkus, M. P. Brenner, and V. N. Manoharan, “The Free-Energy Landscape of Clusters of Attractive Hard Spheres,” *Science*, vol. 327, pp. 560–563, Jan. 2010.
- [7] M. Mondal, C. K. Mishra, R. Banerjee, S. Narasimhan, A. K. Sood, and R. Ganapathy, “Cooperative particle rearrangements facilitate the self-organized growth of colloidal crystal arrays on strain-relief patterns,” *Science Advances*, vol. 6, p. eaay8418, Mar. 2020.
- [8] J. R. Savage, D. W. Blair, A. J. Levine, R. A. Guyer, and A. D. Dinsmore, “Imaging the Sublimation Dynamics of Colloidal Crystallites,” *Science*, vol. 314, pp. 795–798, Nov. 2006.
- [9] P. N. Pusey and W. van Megen, “Phase behaviour of concentrated suspensions of nearly hard colloidal spheres,” *Nature*, vol. 320, pp. 340–342, Mar. 1986.
- [10] J. Perrin, “Mouvement brownien et realite moleculaire,” *Annales de chimie et de physique*, vol. 18, pp. 1–114, 1909.
- [11] D. M. Kaz, R. McGorty, M. Mani, M. P. Brenner, and V. N. Manoharan, “Physical ageing of the contact line on colloidal particles at liquid interfaces,” *Nature Materials*, vol. 11, pp. 138–142, Feb. 2012.

- [12] A. Wang, R. McGorty, D. M. Kaz, and V. N. Manoharan, “Contact-line pinning controls how quickly colloidal particles equilibrate with liquid interfaces,” *Soft Matter*, vol. 12, pp. 8958–8967, Nov. 2016.
- [13] A. Wang, J. W. Zwanikken, D. M. Kaz, R. McGorty, A. M. Goldfain, W. B. Rogers, and V. N. Manoharan, “Before the breach: Interactions between colloidal particles and liquid interfaces at nanoscale separations,” *Physical Review E*, vol. 100, p. 042605, Oct. 2019.
- [14] A. M. Rahmani, A. Wang, V. N. Manoharan, and C. E. Colosqui, “Colloidal particle adsorption at liquid interfaces: capillary driven dynamics and thermally activated kinetics,” *Soft Matter*, vol. 12, pp. 6365–6372, July 2016.
- [15] E. Barry, Z. Hensel, Z. Dogic, M. Shribak, and R. Oldenbourg, “Entropy-Driven Formation of a Chiral Liquid-Crystalline Phase of Helical Filaments,” *Physical Review Letters*, vol. 96, p. 018305, Jan. 2006.
- [16] S. Yardimci, T. Gibaud, W. Schwenger, M. R. Sartucci, P. D. Olmsted, J. S. Urbach, and Z. Dogic, “Bonded straight and helical flagellar filaments form ultra-low-density glasses,” *Proceedings of the National Academy of Sciences*, vol. 120, p. e2215766120, Apr. 2023.
- [17] E. Andablo-Reyes, P. Díaz-Leyva, and J. L. Arauz-Lara, “Microrheology from rotational diffusion of colloidal particles,” *Physical Review Letters*, vol. 94, p. 106001, Mar. 2005.
- [18] G. Foffano, J. S. Lintuvuori, K. Stratford, M. E. Cates, and D. Marenduzzo, “Colloids in Active Fluids: Anomalous Microrheology and Negative Drag,” *Physical Review Letters*, vol. 109, p. 028103, July 2012.
- [19] T. G. Mason, K. Ganesan, J. H. van Zanten, D. Wirtz, and S. C. Kuo, “Particle Tracking Microrheology of Complex Fluids,” *Physical Review Letters*, vol. 79, pp. 3282–3285, Oct. 1997.
- [20] J. Apgar, Y. Tseng, E. Fedorov, M. B. Herwig, S. C. Almo, and D. Wirtz, “Multiple-Particle Tracking Measurements of Heterogeneities in Solutions of Actin Filaments and Actin Bundles,” *Biophysical Journal*, vol. 79, pp. 1095–1106, Aug. 2000.
- [21] P. Schall, D. A. Weitz, and F. Spaepen, “Structural Rearrangements That Govern Flow in Colloidal Glasses,” *Science*, vol. 318, pp. 1895–1899, Dec. 2007.
- [22] P. Schall, I. Cohen, D. A. Weitz, and F. Spaepen, “Dynamics of Dislocations in Thin Colloidal Crystals,” in *Nanomechanics of Materials and Structures* (T. J. Chuang, P. M. Anderson, M. K. Wu, and S. Hsieh, eds.), (Dordrecht), pp. 255–261, Springer Netherlands, 2006.
- [23] A. Pertsinidis and X. S. Ling, “Diffusion of point defects in two-dimensional colloidal crystals,” *Nature*, vol. 413, pp. 147–150, Sept. 2001.

- [24] E. R. Dufresne, T. M. Squires, M. P. Brenner, and D. G. Grier, “Hydrodynamic Coupling of Two Brownian Spheres to a Planar Surface,” *Physical Review Letters*, vol. 85, pp. 3317–3320, Oct. 2000.
- [25] W. B. Rogers and J. C. Crocker, “Direct measurements of DNA-mediated colloidal interactions and their quantitative modeling,” *Proceedings of the National Academy of Sciences*, vol. 108, pp. 15687–15692, Sept. 2011.
- [26] A. E. Larsen and D. G. Grier, “Like-charge attractions in metastable colloidal crystallites,” *Nature*, vol. 385, no. 6613, pp. 230–233, 1997.
- [27] T. M. Squires and M. P. Brenner, “Like-charge attraction and hydrodynamic interaction,” *Physical Review Letters*, vol. 85, no. 23, p. 4976, 2000.
- [28] M. G. Nikolaides, A. R. Bausch, M. F. Hsu, A. D. Dinsmore, M. P. Brenner, C. Gay, and D. A. Weitz, “Electric-field-induced capillary attraction between like-charged particles at liquid interfaces,” *Nature*, vol. 420, pp. 299–301, Nov. 2002.
- [29] A. Kubincová, P. H. Hünenberger, and M. Krishnan, “Interfacial solvation can explain attraction between like-charged objects in aqueous solution,” *The Journal of Chemical Physics*, vol. 152, p. 104713, Mar. 2020.
- [30] R. Brown, “XXVII. A brief account of microscopical observations made in the months of June, July and August 1827, on the particles contained in the pollen of plants; and on the general existence of active molecules in organic and inorganic bodies,” *The Philosophical Magazine*, vol. 4, pp. 161–173, Sept. 1828.
- [31] J. Nozawa, S. Uda, H. Niinomi, J. Okada, and K. Fujiwara, “Heteroepitaxial Growth of Colloidal Crystals: Dependence of the Growth Mode on the Interparticle Interactions and Lattice Spacing,” *The Journal of Physical Chemistry Letters*, vol. 13, pp. 6995–7000, Aug. 2022.
- [32] T. J. Bechtel, T. Reyes-Robles, O. O. Fadeyi, and R. C. Oslund, “Strategies for monitoring cell-cell interactions,” *Nature Chemical Biology*, vol. 17, pp. 641–652, June 2021.
- [33] N. B. Schade, M. C. Holmes-Cerfon, E. R. Chen, D. Aronzon, J. W. Collins, J. A. Fan, F. Capasso, and V. N. Manoharan, “Tetrahedral Colloidal Clusters from Random Parking of Bidisperse Spheres,” *Physical Review Letters*, vol. 110, p. 148303, Apr. 2013.
- [34] W. B. Rogers, W. M. Shih, and V. N. Manoharan, “Using DNA to program the self-assembly of colloidal nanoparticles and microparticles,” *Nature Reviews Materials*, vol. 1, pp. 1–14, Mar. 2016.
- [35] S. Sacanna, W. T. M. Irvine, P. M. Chaikin, and D. J. Pine, “Lock and key colloids,” *Nature*, vol. 464, pp. 575–578, Mar. 2010.

- [36] X. Mao, Q. Chen, and S. Granick, “Entropy favours open colloidal lattices,” *Nature Materials*, vol. 12, pp. 217–222, Mar. 2013.
- [37] M. E. Cates, “Entropy stabilizes open crystals,” *Nature Materials*, vol. 12, pp. 179–180, Mar. 2013.
- [38] S. Hormoz and M. P. Brenner, “Design principles for self-assembly with short-range interactions,” *Proceedings of the National Academy of Sciences*, vol. 108, pp. 5193–5198, Mar. 2011.
- [39] M. Minkov, I. A. D. Williamson, L. C. Andreani, D. Gerace, B. Lou, A. Y. Song, T. W. Hughes, and S. Fan, “Inverse Design of Photonic Crystals through Automatic Differentiation,” *ACS Photonics*, vol. 7, pp. 1729–1741, July 2020.
- [40] M. C. Rechtsman, F. H. Stillinger, and S. Torquato, “Optimized Interactions for Targeted Self-Assembly: Application to a Honeycomb Lattice,” *Physical Review Letters*, vol. 95, p. 228301, Nov. 2005.
- [41] Z. M. Sherman, M. P. Howard, B. A. Lindquist, R. B. Jadrich, and T. M. Truskett, “Inverse methods for design of soft materials,” *The Journal of Chemical Physics*, vol. 152, p. 140902, Apr. 2020.
- [42] C. P. Goodrich, E. M. King, S. S. Schoenholz, E. D. Cubuk, and M. P. Brenner, “Designing self-assembling kinetics with differentiable statistical physics models,” *Proceedings of the National Academy of Sciences*, vol. 118, p. e2024083118, Mar. 2021.
- [43] E. M. King, Z. Wang, D. A. Weitz, F. Spaepen, and M. P. Brenner, “Correlation Tracking: Using simulations to interpolate highly correlated particle tracks,” *Physical Review E*, vol. 105, no. 4, p. 044608, 2022.
- [44] C. Martin, L. E. Altman, S. Rawat, A. Wang, D. G. Grier, and V. N. Manoharan, “In-line holographic microscopy with model-based analysis,” *Nature Reviews Methods Primers*, vol. 2, pp. 1–17, Oct. 2022.
- [45] J. Sheng, E. Malkiel, and J. Katz, “Digital holographic microscope for measuring three-dimensional particle distributions and motions,” *Applied Optics*, vol. 45, pp. 3893–3901, June 2006.
- [46] A. Wang, R. F. Garman, and V. N. Manoharan, “Tracking E coli runs and tumbles with scattering solutions and digital holographic microscopy,” *Optics Express*, vol. 24, pp. 23719–23725, Oct. 2016.
- [47] D. Gabor, “A New Microscopic Principle,” *Nature*, vol. 161, pp. 777–778, May 1948.
- [48] D. Gabor and W. L. Bragg, “Microscopy by reconstructed wave-fronts,” *Proceedings of the Royal Society of London. Series A. Mathematical and Physical Sciences*, vol. 197, pp. 454–487, July 1949.

- [49] W. Xu, M. H. Jericho, I. A. Meinertzhangen, and H. J. Kreuzer, “Digital in-line holography for biological applications,” *Proceedings of the National Academy of Sciences*, vol. 98, pp. 11301–11305, Sept. 2001.
- [50] W. Xu, M. H. Jericho, H. J. Kreuzer, and I. A. Meinertzhangen, “Tracking particles in four dimensions with in-line holographic microscopy,” *Optics Letters*, vol. 28, pp. 164–166, Feb. 2003.
- [51] M. J. Berg, “Tutorial: Aerosol characterization with digital in-line holography,” *Journal of Aerosol Science*, vol. 165, p. 106023, Sept. 2022.
- [52] M. K. Kim, “Principles and techniques of digital holographic microscopy,” *SPIE Reviews*, vol. 1, p. 018005, Apr. 2010.
- [53] S. K. Jericho, J. Garcia-Sucerquia, W. Xu, M. H. Jericho, and H. J. Kreuzer, “Submersible digital in-line holographic microscope,” *Review of Scientific Instruments*, vol. 77, p. 043706, Apr. 2006.
- [54] J. Garcia-Sucerquia, W. Xu, S. K. Jericho, P. Klages, M. H. Jericho, and H. J. Kreuzer, “Digital in-line holographic microscopy,” *Applied Optics*, vol. 45, pp. 836–850, Feb. 2006.
- [55] W. Bishara, H. Zhu, and A. Ozcan, “Holographic opto-fluidic microscopy,” *Optics Express*, vol. 18, pp. 27499–27510, Dec. 2010.
- [56] P. Marquet, B. Rappaz, P. J. Magistretti, E. Cuche, Y. Emery, T. Colomb, and C. Depeursinge, “Digital holographic microscopy: a noninvasive contrast imaging technique allowing quantitative visualization of living cells with subwavelength axial accuracy,” *Optics Letters*, vol. 30, pp. 468–470, Mar. 2005.
- [57] A. Mölder, M. Sebesta, M. Gustafsson, L. Gisselson, A. G. Wingren, and K. Alm, “Non-invasive, label-free cell counting and quantitative analysis of adherent cells using digital holography,” *Journal of Microscopy*, vol. 232, pp. 240–247, Nov. 2008.
- [58] B. Kemper and G. von Bally, “Digital holographic microscopy for live cell applications and technical inspection,” *Applied Optics*, vol. 47, pp. A52–A61, Feb. 2008.
- [59] Y. Park, C. Depeursinge, and G. Popescu, “Quantitative phase imaging in biomedicine,” *Nature Photonics*, vol. 12, pp. 578–589, Oct. 2018.
- [60] A. Barty, K. A. Nugent, A. Roberts, and D. Paganin, “Quantitative phase tomography,” *Optics Communications*, vol. 175, pp. 329–336, Mar. 2000.
- [61] G. Popescu, *Quantitative Phase Imaging of Cells and Tissues*. McGraw-Hill Education, 2011.

- [62] G. Popescu, Y. Park, W. Choi, R. R. Dasari, M. S. Feld, and K. Badizadegan, “Imaging red blood cell dynamics by quantitative phase microscopy,” *Blood Cells, Molecules, and Diseases*, vol. 41, pp. 10–16, July 2008.
- [63] P. Marquet, C. Depeursinge, and P. J. Magistretti, “Review of quantitative phase-digital holographic microscopy: promising novel imaging technique to resolve neuronal network activity and identify cellular biomarkers of psychiatric disorders,” *Neurophotonics*, vol. 1, p. 020901, Sept. 2014.
- [64] G. Mie, “Beiträge zur Optik trüber Medien, speziell kolloidaler Metallösungen,” *Annalen der Physik*, vol. 330, no. 3, pp. 377–445, 1908.
- [65] B. Ovryn and S. H. Izen, “Imaging of transparent spheres through a planar interface using a high-numerical-aperture optical microscope,” *Journal of the Optical Society of America A*, vol. 17, pp. 1202–1213, July 2000.
- [66] S.-H. Lee, Y. Roichman, G.-R. Yi, S.-H. Kim, S.-M. Yang, A. van Blaaderen, P. van Oostrum, and D. G. Grier, “Characterizing and tracking single colloidal particles with video holographic microscopy,” *Optics Express*, vol. 15, pp. 18275–18282, Dec. 2007.
- [67] A. Wang, W. B. Rogers, and V. N. Manoharan, “Effects of Contact-Line Pinning on the Adsorption of Nonspherical Colloids at Liquid Interfaces,” *Physical Review Letters*, vol. 119, p. 108004, Sept. 2017.
- [68] A. Wang, T. G. Dimiduk, J. Fung, S. Razavi, I. Kretzschmar, K. Chaudhary, and V. N. Manoharan, “Using the discrete dipole approximation and holographic microscopy to measure rotational dynamics of non-spherical colloidal particles,” *Journal of Quantitative Spectroscopy and Radiative Transfer*, vol. 146, pp. 499–509, Oct. 2014.
- [69] J. Fung, K. E. Martin, R. W. Perry, D. M. Kaz, R. McGorty, and V. N. Manoharan, “Measuring translational, rotational, and vibrational dynamics in colloids with digital holographic microscopy,” *Optics Express*, vol. 19, pp. 8051–8065, Apr. 2011.
- [70] M. A. Yurkin and A. G. Hoekstra, “The discrete dipole approximation: An overview and recent developments,” *Journal of Quantitative Spectroscopy and Radiative Transfer*, vol. 106, pp. 558–589, July 2007.
- [71] M. A. Yurkin and A. G. Hoekstra, “The discrete-dipole-approximation code ADDA: Capabilities and known limitations,” *Journal of Quantitative Spectroscopy and Radiative Transfer*, vol. 112, pp. 2234–2247, Sept. 2011.
- [72] Y. Pu and H. Meng, “Intrinsic aberrations due to Mie scattering in particle holography,” *Journal of the Optical Society of America A*, vol. 20, pp. 1920–1932, Oct. 2003.

- [73] D. Dulin, S. Barland, X. Hachair, and F. Pedaci, “Efficient Illumination for Microsecond Tracking Microscopy,” *PLoS ONE*, vol. 9, p. e107335, Sept. 2014.
- [74] C. B. Giuliano, R. Zhang, and L. G. Wilson, “Digital Inline Holographic Microscopy (DIHM) of Weakly-scattering Subjects,” *JoVE (Journal of Visualized Experiments)*, p. e50488, Feb. 2014.
- [75] M. Kanka, R. Riesenbergs, P. Petruks, and C. Graulig, “High resolution (NA=0.8) in lensless in-line holographic microscopy with glass sample carriers,” *Optics Letters*, vol. 36, pp. 3651–3653, Sept. 2011.
- [76] J. Garcia-Sucerquia, “Noise reduction in digital lensless holographic microscopy by engineering the light from a light-emitting diode,” *Applied Optics*, vol. 52, pp. A232–A239, Jan. 2013.
- [77] S. Hell, G. Reiner, C. Cremer, and E. H. K. Stelzer, “Aberrations in confocal fluorescence microscopy induced by mismatches in refractive index,” *Journal of Microscopy*, vol. 169, no. 3, pp. 391–405, 1993.
- [78] Y. Wu and A. Ozcan, “Lensless digital holographic microscopy and its applications in biomedicine and environmental monitoring,” *Methods*, vol. 136, pp. 4–16, Mar. 2018.
- [79] N.-N. Deng, Z.-J. Meng, R. Xie, X.-J. Ju, C.-L. Mou, W. Wang, and L.-Y. Chu, “Simple and cheap microfluidic devices for the preparation of monodisperse emulsions,” *Lab on a Chip*, vol. 11, no. 23, pp. 3963–3969, 2011.
- [80] H. W. Moyses, B. J. Krishnatreya, and D. G. Grier, “Robustness of Lorenz-Mie microscopy against defects in illumination,” *Optics Express*, vol. 21, p. 5968, Mar. 2013.
- [81] C. Martin, B. Leahy, and V. N. Manoharan, “Improving holographic particle characterization by modeling spherical aberration,” *Optics Express*, vol. 29, p. 18212, June 2021.
- [82] J. Fung, R. W. Perry, T. G. Dimiduk, and V. N. Manoharan, “Imaging multiple colloidal particles by fitting electromagnetic scattering solutions to digital holograms,” *Journal of Quantitative Spectroscopy and Radiative Transfer*, vol. 113, pp. 2482–2489, Dec. 2012.
- [83] F. C. Cheong, B. S. Rémi Dreyfus, J. Amato-Grill, K. Xiao, L. Dixon, and D. G. Grier, “Flow visualization and flow cytometry with holographic video microscopy,” *Optics Express*, vol. 17, p. 13071, July 2009.
- [84] L. Dixon, F. C. Cheong, and D. G. Grier, “Holographic deconvolution microscopy for high-resolution particle tracking,” *Optics Express*, vol. 19, p. 16410, Aug. 2011.
- [85] A. D. Edelstein, M. A. Tsuchida, N. Amodaj, H. Pinkard, R. D. Vale, and N. Stuurman, “Advanced methods of microscope control using µManager software,” *Journal of Biological Methods*, vol. 1, no. 2, p. e10, 2014.

- [86] D. Vercruyse, A. Dusa, R. Stahl, G. Vanmeerbeeck, K. de Wijs, C. Liu, D. Prodanov, P. Peumans, and L. Lagae, “Three-part differential of unlabeled leukocytes with a compact lens-free imaging flow cytometer,” *Lab on a Chip*, vol. 15, pp. 1123–1132, Feb. 2015.
- [87] T. G. Dimiduk, E. A. Kosheleva, D. Kaz, R. McGorty, E. J. Gardel, and V. N. Manoharan, “A Simple, Inexpensive Holographic Microscope,” p. JMA38, Optical Society of America, Apr. 2010. In Digital Holography and Three-Dimensional Imaging (OSA Topical Meeting).
- [88] J. Fung, *Measuring the 3D Dynamics of Multiple Colloidal Particles with Digital Holographic Microscopy*. PhD thesis, Harvard University, Graduate School of Arts & Sciences, 2013.
- [89] D. Moreno, F. M. Santoyo, J. A. Guerrero, and M. Funes-Gallanzi, “Particle positioning from charge-coupled device images by the generalized Lorenz–Mie theory and comparison with experiment,” *Applied Optics*, vol. 39, pp. 5117–5124, Oct. 2000.
- [90] L. Denis, C. Fournier, T. Fournel, C. Ducottet, and D. Jeulin, “Direct extraction of the mean particle size from a digital hologram,” *Applied Optics*, vol. 45, pp. 944–952, Feb. 2006.
- [91] J. A. Guerrero-Viramontes, D. Moreno-Hernández, F. Mendoza-Santoyo, and M. Funes-Gallanzi, “3D particle positioning from CCD images using the generalized Lorenz–Mie and Huygens–Fresnel theories,” *Measurement Science and Technology*, vol. 17, pp. 2328–2334, July 2006.
- [92] A. Yevick, M. Hannel, and D. G. Grier, “Machine-learning approach to holographic particle characterization,” *Optics Express*, vol. 22, p. 26884, Nov. 2014.
- [93] M. D. Hannel, A. Abdulali, M. O’Brien, and D. G. Grier, “Machine-learning techniques for fast and accurate feature localization in holograms of colloidal particles,” *Optics Express*, vol. 26, p. 15221, June 2018.
- [94] L. E. Altman and D. G. Grier, “CATCH: Characterizing and Tracking Colloids Holographically Using Deep Neural Networks,” *The Journal of Physical Chemistry B*, vol. 124, p. 1602–1610, Feb. 2020.
- [95] M. Hannel, C. Middleton, and D. G. Grier, “Holographic characterization of imperfect colloidal spheres,” *Applied Physics Letters*, vol. 107, p. 141905, Oct. 2015.
- [96] R. O. Duda and P. E. Hart, “Use of the Hough transformation to detect lines and curves in pictures,” *Communications of the ACM*, vol. 15, pp. 11–15, 1972.
- [97] D. H. Ballard, “Generalizing the Hough transform to detect arbitrary shapes,” *Pattern Recognition*, vol. 13, pp. 111–122, 1981.
- [98] T. G. Dimiduk, R. W. Perry, J. Fung, and V. N. Manoharan, “Random-subset fitting of digital holograms for fast three-dimensional particle tracking [Invited],” *Applied Optics*, vol. 53, pp. G177–G183, Sept. 2014.

- [99] T. G. Dimiduk and V. N. Manoharan, “Bayesian approach to analyzing holograms of colloidal particles,” *Optics Express*, vol. 24, p. 24045, Oct. 2016.
- [100] J. J. Moré, “The Levenberg-Marquardt algorithm: Implementation and theory,” in *Numerical Analysis* (G. A. Watson, ed.), Lecture Notes in Mathematics, (Berlin, Heidelberg), pp. 105–116, Springer, 1978.
- [101] F. C. Cheong, B. J. Krishnatreya, and D. G. Grier, “Strategies for three-dimensional particle tracking with holographic video microscopy,” *Optics Express*, vol. 18, p. 13563, June 2010.
- [102] B. J. Krishnatreya, A. Colen-Landy, P. Hasebe, B. A. Bell, J. R. Jones, A. Sunda-Meya, and D. G. Grier, “Measuring Boltzmann’s constant through holographic video microscopy of a single colloidal sphere,” *American Journal of Physics*, vol. 82, pp. 23–31, Jan. 2014.
- [103] Y. Roichman, B. Sun, A. Stolarski, and D. G. Grier, “Influence of nonconservative optical forces on the dynamics of optically trapped colloidal spheres: the fountain of probability,” *Physical Review Letters*, vol. 101, no. 12, p. 128301, 2008.
- [104] B. Sun, J. Lin, E. Darby, A. Y. Grosberg, and D. G. Grier, “Brownian vortexes,” *Physical Review E*, vol. 80, no. 1, p. 010401, 2009.
- [105] M. J. O’Brien and D. G. Grier, “Above and beyond: holographic tracking of axial displacements in holographic optical tweezers,” *Optics Express*, vol. 27, p. 25375, Sept. 2019.
- [106] K. Xiao and D. G. Grier, “Sorting colloidal particles into multiple channels with optical forces: prismatic optical fractionation,” *Physical Review E*, vol. 82, p. 051407, Nov. 2010.
- [107] K. Xiao and D. G. Grier, “Multidimensional Optical Fractionation of Colloidal Particles with Holographic Verification,” *Physical Review Letters*, vol. 104, p. 028302, Jan. 2010.
- [108] A. Winters, F. C. Cheong, M. A. Odete, J. Lumer, D. B. Ruffner, K. I. Mishra, D. G. Grier, and L. A. Philips, “Quantitative Differentiation of Protein Aggregates From Other Sub-visible Particles in Viscous Mixtures Through Holographic Characterization,” *Journal of Pharmaceutical Sciences*, vol. 109, pp. 2405–2412, Aug. 2020.
- [109] C. Wang, H. Shpaisman, A. D. Hollingsworth, and D. G. Grier, “Celebrating Soft Matter’s 10th Anniversary: Monitoring colloidal growth with holographic microscopy,” *Soft Matter*, vol. 11, no. 6, pp. 1062–1066, 2015.
- [110] H. Shpaisman, B. Jyoti Krishnatreya, and D. G. Grier, “Holographic microrefractometer,” *Applied Physics Letters*, vol. 101, p. 091102, Aug. 2012.
- [111] F. C. Cheong, S. Duarte, S.-H. Lee, and D. G. Grier, “Holographic microrheology of polysaccharides from *Streptococcus mutans* biofilms,” *Rheologica Acta*, vol. 48, pp. 109–115, Jan. 2009.

- [112] C. Wang, X. Zhong, D. B. Ruffner, A. Stutt, L. A. Philips, M. D. Ward, and D. G. Grier, “Holographic Characterization of Protein Aggregates,” *Journal of Pharmaceutical Sciences*, vol. 105, pp. 1074–1085, Mar. 2016.
- [113] J. Fung and S. Hoang, “Computational assessment of an effective-sphere model for characterizing colloidal fractal aggregates with holographic microscopy,” *Journal of Quantitative Spectroscopy and Radiative Transfer*, vol. 236, p. 106591, Oct. 2019.
- [114] L. E. Altman, R. Quddus, F. C. Cheong, and D. G. Grier, “Holographic characterization and tracking of colloidal dimers in the effective-sphere approximation,” *Soft Matter*, vol. 17, no. 10, pp. 2695–2703, 2021.
- [115] L. A. Philips, D. B. Ruffner, F. C. Cheong, J. M. Blusewicz, P. Kasimbeg, B. Waisi, J. R. Mc-Cutcheon, and D. G. Grier, “Holographic characterization of contaminants in water: Differentiation of suspended particles in heterogeneous dispersions,” *Water Research*, vol. 122, pp. 431–439, Oct. 2017.
- [116] F. C. Cheong, P. Kasimbeg, D. B. Ruffner, E. H. Hlaing, J. M. Blusewicz, L. A. Philips, and D. G. Grier, “Holographic characterization of colloidal particles in turbid media,” *Applied Physics Letters*, vol. 111, p. 153702, Oct. 2017.
- [117] D. W. Mackowski and M. I. Mishchenko, “Calculation of the T matrix and the scattering matrix for ensembles of spheres,” *Journal of the Optical Society of America A*, vol. 13, pp. 2266–2278, Nov. 1996.
- [118] B. Leahy, B. Leahy, R. Alexander, R. Alexander, C. Martin, S. Barkley, V. N. Manoharan, and V. N. Manoharan, “Large depth-of-field tracking of colloidal spheres in holographic microscopy by modeling the objective lens,” *Optics Express*, vol. 28, pp. 1061–1075, Jan. 2020.
- [119] R. Alexander, B. Leahy, and V. N. Manoharan, “Precise measurements in digital holographic microscopy by modeling the optical train,” *Journal of Applied Physics*, vol. 128, p. 060902, Aug. 2020.
- [120] C. J. Geyer, “Introduction to Markov Chain Monte Carlo,” in *Handbook of Markov Chain Monte Carlo* (S. Brooks, A. Gelman, G. L. Jones, and X.-L. Meng, eds.), Chapman & Hall/CRC Handbooks of Modern Statistical Methods, pp. 3–48, Chapman & Hall/CRC, 2011.
- [121] N. Hansen and A. Ostermeier, “Adapting arbitrary normal mutation distributions in evolution strategies: The covariance matrix adaptation,” in *Proceedings of IEEE international conference on evolutionary computation*, pp. 312–317, IEEE, 1996.

- [122] R. M. Neal, “MCMC Using Hamiltonian dynamics,” in *Handbook of Markov Chain Monte Carlo* (S. Brooks, A. Gelman, G. L. Jones, and X. L. Meng, eds.), pp. 113–162, Chapman & Hall/CRC Handbooks of Modern Statistical Methods, 2011.
- [123] D. J. Earl and M. W. Deem, “Parallel tempering: Theory, applications, and new perspectives,” *Physical Chemistry Chemical Physics*, vol. 7, pp. 3910–3916, Nov. 2005.
- [124] S. Barkley, T. G. Dimiduk, J. Fung, D. M. Kaz, V. N. Manoharan, R. McGorty, R. W. Perry, and A. Wang, “Holographic Microscopy With Python and HoloPy,” *Computing in Science Engineering*, vol. 22, pp. 72–82, Sept. 2020.
- [125] J. Crocker and D. Grier, “Methods of digital video microscopy for colloidal studies,” *Journal of Colloid and Interface Science*, vol. 179, no. 1, pp. 298–310, 1996.
- [126] B. J. Krishnatreya and D. G. Grier, “Fast feature identification for holographic tracking: the orientation alignment transform,” *Optics Express*, vol. 22, p. 12773, June 2014.
- [127] R. Parthasarathy, “Rapid, accurate particle tracking by calculation of radial symmetry centers,” *Nature Methods*, vol. 9, pp. 724–726, 2012.
- [128] G. M. Rotskoff and E. Vanden-Eijnden, “Trainability and Accuracy of Neural Networks: An Interacting Particle System Approach,” *arXiv e-prints*, p. arXiv:1805.00915, May 2018.
- [129] J. M. Newby, A. M. Schaefer, P. T. Lee, M. G. Forest, and S. K. Lai, “Convolutional neural networks automate detection for tracking of submicron-scale particles in 2D and 3D,” *Proceedings of the National Academy of Sciences of the United States of America*, vol. 115, pp. 9026–9031, Sept. 2018.
- [130] B. Schneider, J. Dambre, and P. Bienstman, “Fast particle characterization using digital holography and neural networks,” *Applied Optics*, vol. 55, p. 133, Jan. 2016.
- [131] E. Klein, *Structure and Dynamics of Colloidal Clusters*. PhD thesis, Harvard University, Graduate School of Arts & Sciences, 2019.
- [132] D. P. Kingma and J. Ba, “Adam: A Method for Stochastic Optimization,” Dec. 2014. arXiv e-prints, arXiv:1412.6980.
- [133] L. Bottou, “Large-Scale Machine Learning with Stochastic Gradient Descent,” in *Proceedings of COMPSTAT 2010* (Y. Lechevallier and G. Saporta, eds.), (Heidelberg), pp. 177–186, Physica-Verlag HD, 2010.
- [134] X. Glorot, A. Bordes, and Y. Bengio, “Deep Sparse Rectifier Neural Networks,” in *Proceedings of the Fourteenth International Conference on Artificial Intelligence and Statistics* (G. Gordon, D. Dunson, and M. Dudík, eds.), vol. 15 of *Proceedings of Machine Learning Research*, pp. 315–323, Apr. 2011.

- [135] J. Redmon and A. Farhadi, “YOLOv3: An Incremental Improvement,” *arXiv e-prints*, 2018. arXiv:1804.02767.
- [136] C. Szegedy, V. Vanhoucke, S. Ioffe, J. Shlens, and Z. Wojna, “Rethinking the Inception Architecture for Computer Vision,” Proceedings of the IEEE Conference on Computer Vision and Pattern Recognition (CVPR), pp. 2818–2826, 2016.
- [137] R. W. Perry, G. Meng, T. G. Dimiduk, J. Fung, and V. N. Manoharan, “Real-space studies of the structure and dynamics of self-assembled colloidal clusters,” *Faraday Discussions*, vol. 159, pp. 211–234, Mar. 2013.
- [138] S. U. Pickering, “Emulsions,” *Journal of the Chemical Society, Transactions*, vol. 91, pp. 2001–2021, Jan. 1907.
- [139] J. Xiao, Y. Li, and Q. Huang, “Recent advances on food-grade particles stabilized Pickering emulsions: Fabrication, characterization and research trends,” *Trends in Food Science & Technology*, vol. 55, pp. 48–60, Sept. 2016.
- [140] K. Y. Yoon, H. A. Son, S. K. Choi, J. W. Kim, W. M. Sung, and H. T. Kim, “Core Flooding of Complex Nanoscale Colloidal Dispersions for Enhanced Oil Recovery by in Situ Formation of Stable Oil-in-Water Pickering Emulsions,” *Energy & Fuels*, vol. 30, pp. 2628–2635, Apr. 2016.
- [141] A. Bhargava, A. V. Francis, and A. K. Biswas, “Interfacial studies related to the recovery of mineral slimes in a water-hydrocarbon liquid-collector system,” *Journal of Colloid and Interface Science*, vol. 64, pp. 214–227, Apr. 1978.
- [142] R. Aveyard, B. P. Binks, and J. H. Clint, “Emulsions stabilised solely by colloidal particles,” *Advances in Colloid and Interface Science*, vol. 100–102, pp. 503–546, Feb. 2003.
- [143] A. D. Dinsmore, M. F. Hsu, M. G. Nikolaides, M. Marquez, A. R. Bausch, and D. A. Weitz, “Colloidosomes: selectively permeable capsules composed of colloidal particles,” *Science*, vol. 298, pp. 1006–1009, Nov. 2002.
- [144] J. Fung and V. N. Manoharan, “Holographic measurements of anisotropic three-dimensional diffusion of colloidal clusters,” *Physical Review E*, vol. 88, p. 020302, Aug. 2013.
- [145] R. N. Zia, “Active and Passive Microrheology: Theory and Simulation,” *Annual Review of Fluid Mechanics*, vol. 50, pp. 371–405, Jan. 2018.
- [146] R. W. Style, R. Boltynskiy, G. K. German, C. Hyland, C. W. MacMinn, A. F. Mertz, L. A. Wilen, Y. Xu, and E. R. Dufresne, “Traction force microscopy in physics and biology,” *Soft Matter*, vol. 10, pp. 4047–4055, May 2014.

- [147] F. C. Cheong and D. G. Grier, “Rotational and translational diffusion of copper oxide nanorods measured with holographic video microscopy,” *Optics Express*, vol. 18, p. 6555, Mar. 2010.
- [148] S. Makarchuk, N. Beyer, C. Gaiddon, W. Grange, and P. Hébraud, “Holographic Traction Force Microscopy,” *Scientific Reports*, vol. 8, p. 3038, Feb. 2018.
- [149] W. E. Moerner and D. P. Fromm, “Methods of single-molecule fluorescence spectroscopy and microscopy,” *Review of Scientific Instruments*, vol. 74, pp. 3597–3619, Aug. 2003.
- [150] Z. A. Steelman, W. J. Eldridge, J. B. Weintraub, and A. Wax, “Is the nuclear refractive index lower than cytoplasm? Validation of phase measurements and implications for light scattering technologies,” *Journal of Biophotonics*, vol. 10, pp. 1714–1722, Dec. 2017.
- [151] P. Y. Liu, L. K. Chin, S. W, T. C. Ayi, P. H. Yap, T. Bourouina, and Y. Leprince-Wang, “Real-time measurement of single bacterium’s refractive index using optofluidic immersion refractometry,” *Procedia Engineering*, vol. 87, pp. 356–359, 2014.
- [152] M. Molaei and J. Sheng, “Imaging bacterial 3D motion using digital in-line holographic microscopy and correlation-based de-noising algorithm,” *Optics Express*, vol. 22, p. 32119, Dec. 2014.
- [153] G. Bozzuto and A. Molinari, “Liposomes as nanomedical devices,” *International Journal of Nanomedicine*, vol. 10, pp. 975–999, Feb. 2015.
- [154] D. Deamer, “The Role of Lipid Membranes in Life’s Origin,” *Life*, vol. 7, p. 5, Jan. 2017.
- [155] P. Schwille and S. Diez, “Synthetic biology of minimal systems,” *Critical Reviews in Biochemistry and Molecular Biology*, vol. 44, pp. 223–242, Aug. 2009.
- [156] K. Spustova, E. S. Köksal, A. Ainla, and I. Gözen, “Subcompartmentalization and Pseudo-Division of Model Protocells,” *Small*, vol. 17, no. 2, p. 2005320, 2021.
- [157] A. Wang, C. Chan Miller, and J. W. Szostak, “Core-Shell Modeling of Light Scattering by Vesicles: Effect of Size, Contents, and Lamellarity,” *Biophysical Journal*, vol. 116, pp. 659–669, Feb. 2019.
- [158] L. H. A. Tran, M. Turner, J. Luong, O. A. A. Khamis, Y. Deckel, L. A. Lowe, and A. Wang, “Measuring vesicle loading with holographic microscopy,” *arXiv e-print*, Apr. 2022. arXiv:2204.13068.
- [159] L. E. Altman and D. G. Grier, “Interpreting holographic molecular binding assays with effective medium theory,” *Biomedical Optics Express*, vol. 11, p. 5225, Sept. 2020.

- [160] M. K. Quinn, N. Gnan, S. James, A. Ninarello, F. Sciortino, E. Zaccarelli, and J. J. McManus, “How fluorescent labelling alters the solution behaviour of proteins,” *Physical Chemistry Chemical Physics*, vol. 17, pp. 31177–31187, Nov. 2015.
- [161] L. D. Hughes, R. J. Rawle, and S. G. Boxer, “Choose Your Label Wisely: Water-Soluble Fluorophores Often Interact with Lipid Bilayers,” *PLOS ONE*, vol. 9, p. e87649, Feb. 2014.
- [162] V. Markel, “Introduction to the Maxwell Garnett approximation: tutorial,” *Journal of the Optical Society of America A*, vol. 33, pp. 1244–1256, 2016.
- [163] Y. Zagzag, M. F. Soddu, A. D. Hollingsworth, and D. G. Grier, “Holographic molecular binding assays,” *Scientific Reports*, vol. 10, p. 1932, Dec. 2020.
- [164] K. Snyder, R. Quddus, A. D. Hollingsworth, K. Kirshenbaum, and D. G. Grier, “Holographic immunoassays: direct detection of antibodies binding to colloidal spheres,” *Soft Matter*, vol. 16, no. 44, pp. 10180–10186, 2020.
- [165] B. T. Draine, “The discrete-dipole approximation and its application to interstellar graphite grains,” *Astrophysical Journal*, vol. 333, pp. 848–872, 1988.
- [166] D. B. Ruffner, F. C. Cheong, J. M. Blusewicz, and L. A. Philips, “Lifting degeneracy in holographic characterization of colloidal particles using multi-color imaging,” *Optics Express*, vol. 26, pp. 13239–13251, May 2018.
- [167] S. Rawat, J. Wendoloski, and A. Wang, “cGAN-assisted imaging through stationary scattering media,” *Optics Express*, vol. 30, pp. 18145–18155, May 2022.
- [168] M. Abadi, A. Agarwal, P. Barham, E. Brevdo, Z. Chen, C. Citro, G. S. Corrado, A. Davis, J. Dean, M. Devin, S. Ghemawat, I. Goodfellow, A. Harp, G. Irving, M. Isard, Y. Jia, R. Jozefowicz, L. Kaiser, M. Kudlur, J. Levenberg, D. Mane, R. Monga, S. Moore, D. Murray, C. Olah, M. Schuster, J. Shlens, B. Steiner, I. Sutskever, K. Talwar, P. Tucker, V. Vanhoucke, V. Vasudevan, F. Viegas, O. Vinyals, P. Warden, M. Wattenberg, M. Wicke, Y. Yu, and X. Zheng, “TensorFlow: Large-Scale Machine Learning on Heterogeneous Distributed Systems,” *arXiv e-print*, Mar. 2016. arXiv:1603.04467.
- [169] A. Kucukelbir, D. Tran, R. Ranganath, A. Gelman, and D. M. Blei, “Automatic Differentiation Variational Inference,” *Journal of Machine Learning Research*, vol. 18, pp. 1–45, 2017.
- [170] N. P. Jouppi, C. Young, N. Patil, D. Patterson, G. Agrawal, R. Bajwa, S. Bates, S. Bhatia, N. Boden, A. Borchers, R. Boyle, P.-l. Cantin, C. Chao, C. Clark, J. Coriell, M. Daley, M. Dau, J. Dean, B. Gelb, T. V. Ghaemmaghami, R. Gottipati, W. Gulland, R. Hagmann, C. R. Ho, D. Hogberg, J. Hu, R. Hundt, D. Hurt, J. Ibarz, A. Jaffey, A. Jaworski, A. Kaplan, H. Khaitan, D. Killebrew, A. Koch, N. Kumar, S. Lacy, J. Laudon, J. Law, D. Le, C. Leary, Z. Liu, K. Lucke, A. Lundin, G. MacKean, A. Maggiore, M. Mahony, K. Miller, R. Nagarajan, R. Narayanaswami, R. Ni, K. Nix, T. Norrie, M. Omernick, N. Penukonda, A. Phelps,

J. Ross, M. Ross, A. Salek, E. Samadiani, C. Severn, G. Sizikov, M. Snelham, J. Souter, D. Steinberg, A. Swing, M. Tan, G. Thorson, B. Tian, H. Toma, E. Tuttle, V. Vasudevan, R. Walter, W. Wang, E. Wilcox, and D. H. Yoon, “In-Datacenter Performance Analysis of a Tensor Processing Unit,” in *Proceedings of the 44th Annual International Symposium on Computer Architecture*, ISCA, pp. 1–12, Association for Computing Machinery, June 2017.

- [171] E. N. Leith, J. Upatnieks, and K. A. Haines, “Microscopy by Wavefront Reconstruction,” *Journal of the Optical Society of America*, vol. 55, pp. 981–986, Aug. 1965.
- [172] U. Schnars and W. Jüptner, “Direct recording of holograms by a CCD target and numerical reconstruction,” *Applied Optics*, vol. 33, pp. 179–181, Jan. 1994.
- [173] R. Hickling, “Holography of Liquid Droplets,” *Journal of the Optical Society of America*, vol. 59, pp. 1334–1339, Oct. 1969.
- [174] F. Slimani, G. Grehan, G. Gouesbet, and D. Allano, “Near-field Lorenz-Mie theory and its application to microholography,” *Applied Optics*, vol. 23, pp. 4140–4148, Nov. 1984.
- [175] C. Trujillo, R. Castañeda, P. Piedrahita-Quintero, and J. García-Sucerquia, “Automatic full compensation of quantitative phase imaging in off-axis digital holographic microscopy,” *Applied Optics*, vol. 55, pp. 10299–10306, Dec. 2016.
- [176] G. Popescu, L. P. Deflores, J. C. Vaughan, K. Badizadegan, H. Iwai, R. R. Dasari, and M. S. Feld, “Fourier phase microscopy for investigation of biological structures and dynamics,” *Optics Letters*, vol. 29, pp. 2503–2505, Nov. 2004.
- [177] C. Joo, T. Akkin, B. Cense, B. H. Park, and J. F. de Boer, “Spectral-domain optical coherence phase microscopy for quantitative phase-contrast imaging,” *Optics Letters*, vol. 30, pp. 2131–2133, Aug. 2005.
- [178] M. Piliarik and V. Sandoghdar, “Direct optical sensing of single unlabelled proteins and super-resolution imaging of their binding sites,” *Nature Communications*, vol. 5, p. 4495, July 2014.
- [179] G. Young, N. Hundt, D. Cole, A. Fineberg, J. Andrecka, A. Tyler, A. Olerinyova, A. Ansari, E. G. Marklund, M. P. Collier, S. A. Chandler, O. Tkachenko, J. Allen, M. Crispin, N. Billington, Y. Takagi, J. R. Sellers, C. Eichmann, P. Selenko, L. Frey, R. Riek, M. R. Galpin, W. B. Struwe, J. L. P. Benesch, and P. Kukura, “Quantitative mass imaging of single biological macromolecules,” *Science*, vol. 360, pp. 423–427, Apr. 2018.
- [180] R. G. Mahmoodabadi, R. W. Taylor, M. Kaller, S. Spindler, M. Mazaheri, K. Kasaian, and V. Sandoghdar, “Point spread function in interferometric scattering microscopy (iSCAT). Part I: Aberrations in defocusing and axial localization,” *Optics Express*, vol. 28, pp. 25969–25988, Aug. 2020.

- [181] U. Schnars and W. Jüptner, “Digital recording and numerical reconstruction of holograms,” *Measurement Science and Technology*, vol. 13, pp. R85–R101, Aug. 2002.
- [182] A. Stadelmaier and J. H. Massig, “Compensation of lens aberrations in digital holography,” *Optics Letters*, vol. 25, pp. 1630–1632, Nov. 2000.
- [183] S. Grilli, P. Ferraro, S. D. Nicola, A. Finizio, G. Pierattini, and R. Meucci, “Whole optical wavefields reconstruction by Digital Holography,” *Optics Express*, vol. 9, pp. 294–302, Sept. 2001.
- [184] P. Ferraro, S. D. Nicola, A. Finizio, G. Coppola, S. Grilli, C. Magro, and G. Pierattini, “Compensation of the inherent wave front curvature in digital holographic coherent microscopy for quantitative phase-contrast imaging,” *Applied Optics*, vol. 42, pp. 1938–1946, Apr. 2003.
- [185] T. Colomb, E. Cuche, F. Charrière, J. Kühn, N. Aspert, F. Montfort, P. Marquet, and C. Depeursinge, “Automatic procedure for aberration compensation in digital holographic microscopy and applications to specimen shape compensation,” *Applied Optics*, vol. 45, pp. 851–863, Feb. 2006.
- [186] S. D. Nicola, A. Finizio, G. Pierattini, D. Alfieri, S. Grilli, L. Sansone, and P. Ferraro, “Recovering correct phase information in multiwavelength digital holographic microscopy by compensation for chromatic aberrations,” *Optics Letters*, vol. 30, pp. 2706–2708, Oct. 2005.
- [187] T. Nguyen, V. Bui, V. Lam, C. B. Raub, L.-C. Chang, and G. Nehmetallah, “Automatic phase aberration compensation for digital holographic microscopy based on deep learning background detection,” *Optics Express*, vol. 25, pp. 15043–15057, June 2017.
- [188] N. Verrier, C. Fournier, L. Méès, and T. Fournel, “In-line particle holography with an astigmatic beam: setup self-calibration using an inverse problems approach,” *Applied Optics*, vol. 53, pp. G147–G156, Sept. 2014.
- [189] L. Denis, C. Fournier, T. Fournel, and C. Ducottet, “Twin-image noise reduction by phase retrieval in in-line digital holography,” in *Wavelets XI*, vol. 5914, p. 59140J, International Society for Optics and Photonics, Sept. 2005.
- [190] C. J. R. Sheppard and C. J. Cogswell, “Effects of aberrating layers and tube length on confocal imaging properties,” *Optik*, vol. 87, no. 1, pp. 34–38, 1991.
- [191] M. Born and E. Wolf, *Principles of Optics*. Cambridge University, 3rd ed., 1983.
- [192] X. Ma, J. Q. Lu, R. S. Brock, K. M. Jacobs, P. Yang, and X.-H. Hu, “Determination of complex refractive index of polystyrene microspheres from 370 to 1610 nm,” *Physics in Medicine and Biology*, vol. 48, pp. 4165–4172, Dec. 2003.

- [193] R. Alexander, S. Barkley, T. G. Dimiduk, J. Fung, A. M. Goldfain, D. M. Kaz, B. Leahy, V. N. Manoharan, R. McGorty, R. W. Perry, and A. Wang, “HoloPy: Holography and Light Scattering in Python,” 2021. Github, <http://github.com/manoharan-lab/holopy>.
- [194] D. Foreman-Mackey, D. W. Hogg, D. Lang, and J. Goodman, “emcee: The MCMC Hammer,” *Publications of the Astronomical Society of the Pacific*, vol. 125, p. 306, Feb. 2013.
- [195] N. Hansen, Y. Akimoto, and P. Baudis, “CMA-ES/pycma: r3.0.3,” Apr. 2020. Zenodo, DOI:[10.5281/zenodo.2559634](https://doi.org/10.5281/zenodo.2559634).
- [196] M. Newville, T. Stensitzki, D. B. Allen, and A. Ingargiola, “LMFIT: Non-Linear Least-Square Minimization and Curve-Fitting for Python,” Sept. 2014. Zenodo, <https://dx.doi.org/10.5281/zenodo.11813>.
- [197] C. Martin, B. Leahy, and V. N. Manoharan, “Data for ‘Effect of spherical aberration on hologram formation and characterization of colloidal spheres’,” 2021. Harvard Dataverse, <https://doi.org/10.7910/DVN/K2AoWW.V1>.
- [198] J. C. Crocker, J. A. Matteo, A. D. Dinsmore, and A. G. Yodh, “Entropic Attraction and Repulsion in Binary Colloids Probed with a Line Optical Tweezer,” *Physical Review Letters*, vol. 82, pp. 4352–4355, May 1999.
- [199] M. A. Bevan and D. C. Prieve, “Direct Measurement of Retarded van der Waals Attraction,” *Langmuir*, vol. 15, pp. 7925–7936, Nov. 1999.
- [200] Z. Zhang and C.-H. Menq, “Three-dimensional particle tracking with subnanometer resolution using off-focus images,” *Applied Optics*, vol. 47, pp. 2361–2370, May 2008.
- [201] M. S. Elliot and W. C. K. Poon, “Conventional optical microscopy of colloidal suspensions,” *Advances in Colloid and Interface Science*, vol. 92, pp. 133–194, Sept. 2001.
- [202] M. Bierbaum, B. D. Leahy, A. A. Alemi, I. Cohen, and J. P. Sethna, “Light Microscopy at Maximal Precision,” *Physical Review X*, vol. 7, p. 041007, Oct. 2017.
- [203] D. Prieve and N. Frej, “Total internal reflection microscopy: a quantitative tool for the measurement of colloidal forces,” *Langmuir*, vol. 6, no. 2, pp. 396–403, 1990.
- [204] C. G. Lopez, R. H. Colby, and J. T. Cabral, “Electrostatic and Hydrophobic Interactions in NaCMC Aqueous Solutions: Effect of Degree of Substitution,” *Macromolecules*, vol. 51, pp. 3165–3175, Apr. 2018.
- [205] C. W. Hoogendam, A. de Keizer, M. A. Cohen Stuart, B. H. Bijsterbosch, J. A. M. Smit, J. A. P. P. van Dijk, P. M. van der Horst, and J. G. Batelaan, “Persistence Length of Carboxymethyl Cellulose As Evaluated from Size Exclusion Chromatography and Potentiometric Titrations,” *Macromolecules*, vol. 31, pp. 6297–6309, Sept. 1998.

- [206] D. W. Hogg, J. Bovy, and D. Lang, “Data analysis recipes: Fitting a model to data,” Aug. 2010. arXiv:1008.4686.
- [207] N. Metropolis, A. W. Rosenbluth, M. N. Rosenbluth, A. H. Teller, and E. Teller, “Equation of State Calculations by Fast Computing Machines,” *Journal of Chemical Physics*, vol. 21, pp. 1087–1092, June 1953.
- [208] M. N. Rosenbluth and A. W. Rosenbluth, “Further results on Monte Carlo equations of state,” *Journal of Chemical Physics*, vol. 22.5, pp. 881–884, 1954.
- [209] W. K. Hastings, “Monte Carlo Sampling Methods Using Markov Chains and Their Applications,” *Biometrika*, vol. 57, no. 1, pp. 97–109, 1970.
- [210] P. Gregory, *Bayesian Logical Data Analysis for the Physical Sciences: A Comparative Approach with Mathematica® Support*. Cambridge University Press, Apr. 2005.
- [211] W. B. Russel, D. A. Saville, and W. R. Schowalter, *Colloidal Dispersions*. Cambridge Monographs on Mechanics, Cambridge: Cambridge University Press, 1989.
- [212] E. B. Sirota, H. D. Ou-Yang, S. K. Sinha, P. M. Chaikin, J. D. Axe, and Y. Fujii, “Complete phase diagram of a charged colloidal system: A synchrotron x-ray scattering study,” *Physical Review Letters*, vol. 62, pp. 1524–1527, Mar. 1989.
- [213] B. Tränkle, D. Ruh, and A. Rohrbach, “Interaction dynamics of two diffusing particles: contact times and influence of nearby surfaces,” *Soft Matter*, vol. 12, pp. 2729–2736, Mar. 2016.
- [214] M. Piech, P. Weronski, X. Wu, and J. Y. Walz, “Prediction and Measurement of the Inter-particle Depletion Interaction Next to a Flat Wall,” *Journal of Colloid and Interface Science*, vol. 247, pp. 327–341, Mar. 2002.
- [215] W. A. Ducker, T. J. Senden, and R. M. Pashley, “Direct measurement of colloidal forces using an atomic force microscope,” *Nature*, vol. 353, pp. 239–241, Sept. 1991.
- [216] K. Lee, M. Kinnunen, M. D. Khokhlova, E. V. Lyubin, A. V. Priezzhev, I. Meglinski, and A. A. Fedyanin, “Optical tweezers study of red blood cell aggregation and disaggregation in plasma and protein solutions,” *Journal of Biomedical Optics*, vol. 21, p. 035001, Mar. 2016.
- [217] J. Dobnikar, M. Brunner, H.-H. von Grünberg, and C. Bechinger, “Three-body interactions in colloidal systems,” *Physical Review E*, vol. 69, p. 031402, Mar. 2004.
- [218] C. Zhang, J. Muñetón Díaz, A. Muster, D. R. Abujetas, L. S. Froufe-Pérez, and F. Scheffold, “Determining intrinsic potentials and validating optical binding forces between colloidal particles using optical tweezers,” *Nature Communications*, vol. 15, p. 1020, Feb. 2024.

- [219] C. R. Iacovella, R. E. Rogers, S. C. Glotzer, and M. J. Solomon, “Pair interaction potentials of colloids by extrapolation of confocal microscopy measurements of collective suspension structure,” *The Journal of Chemical Physics*, vol. 133, p. 164903, Oct. 2010.
- [220] C. P. Royall, A. A. Louis, and H. Tanaka, “Measuring colloidal interactions with confocal microscopy,” *The Journal of Chemical Physics*, vol. 127, p. 044507, July 2007.
- [221] S. Asakura and F. Oosawa, “Interaction between particles suspended in solutions of macromolecules,” *Journal of Polymer Science*, vol. 33, no. 126, pp. 183–192, 1958.
- [222] R. Verma, J. C. Crocker, T. C. Lubensky, and A. G. Yodh, “Entropic Colloidal Interactions in Concentrated DNA Solutions,” *Physical Review Letters*, vol. 81, pp. 4004–4007, Nov. 1998.
- [223] H. C. Trivedi and R. D. Patel, “Studies on Carboxymethylcellulose: Osmotic Pressure Measurements. I,” *Journal of Macromolecular Science: Part A - Chemistry*, vol. 17, pp. 893–903, Apr. 1982.
- [224] J. Salvatier, T. V. Wiecki, and C. Fonnesbeck, “Probabilistic programming in Python using PyMC3,” *PeerJ Computer Science*, vol. 2, p. e55, Apr. 2016.
- [225] S. Zhou, “Three-body potential amongst similarly or differently charged cylinder colloids immersed in a simple electrolyte solution,” *Journal of Statistical Mechanics: Theory and Experiment*, vol. 2015, p. P11030, Nov. 2015.
- [226] S. S. Schoenholz and E. D. Cubuk, “Jax M.D.: A framework for differentiable physics,” in *Advances in Neural Information Processing Systems*, vol. 33, Curran Associates, Inc., 2020.
- [227] D. B. Allan, T. Caswell, N. C. Keim, C. M. van der Wel, and R. W. Verweij, “soft-matter/trackpy: v0.6.1,” Feb. 2023. Zenodo. DOI: 10.5281/zenodo.7670439.
- [228] F. Helmchen and W. Denk, “Deep tissue two-photon microscopy,” *Nature Methods*, vol. 2, pp. 932–940, Dec. 2005.